Fall 2017

Development of active microwave thermography for structural health monitoring

Ali Foudazi

Department: Electrical and Computer Engineering

DEVELOPMENT OF ACTIVE MICROWAVE THERMOGRAPHY FOR STRUCTURAL HEALTH MONITORING

by

ALI FOUDAZI

A DISSERTATION

Presented to the Faculty of the Graduate School of the

MISSOURI UNIVERSITY OF SCIENCE AND TECHNOLOGY

In Partial Fulfillment of the Requirements for the Degree

DOCTOR OF PHILOSOPHY

in

ELECTRICAL ENGINEERING

2017

Approved
Dr. Kristen M. Donnell, Advisor
Dr. Reza Zoughi
Dr. David Pommerenke
Dr. Jun Fan
Dr. K. Chandrashekhara

PUBLICATION DISSERTATION OPTION

This dissertation consists of the following 5 papers, formatted in the style used by the Missouri University of Science and Technology, listed as follows:

Paper I (pages 14-38), A. Foudazi, C. Edwards, M. Ghasr, and K. Donnell, "Active microwave thermography for defect detection of CFRP-strengthened cement-based materials", has been published in IEEE Transactions on Instrumentation and Measurement, vol. 65, no. 11, pp. 2612-2620, 2016.

Paper II (pages 39-59), A. Foudazi, C. Edwards, L. Sneed, M. Ghasr, and K. Donnell, "Active microwave thermography for nondestructive evaluation of FRP-rehabilitated cement-based structures," under review for publication in Research in Nondestructive Evaluation, submitted on June 2017.

Paper III (pages 60-91), A. Foudazi, I. Mehdipour, K. Donnell, and K. Khayat, "Evaluation of steel fiber distribution in cement-based mortars using active microwave", has been published in Materials and Structure, vol. 49, pp. 5051-5065, 2016.

Paper IV (pages 92-101), A. Foudazi, M. Ghasr, and K. Donnell, "Characterization of corroded reinforced steel bars by active microwave thermography", has been published in IEEE Transactions on Instrumentation and Measurement, vol. 64, no. 9, pp. 2583-2585, 2015.

Paper V (pages 102-125), A. Foudazi, A. Mirala, M. Ghasr, and K. Donnell, "Active microwave thermography for nondestructive evaluation of surface crack in metal structures", to be submitted in August 2017 to IEEE Transactions on Instrumentation and Measurement,.

ABSTRACT

Active Microwave Thermography (AMT) is an integrated nondestructive testing and evaluation (NDT&E) method that incorporates aspects of microwave NDT and thermography techniques. AMT uses a microwave excitation to generate heat and the surface thermal profile of the material or structure under test is subsequently measured using a thermal camera (or IR camera). Utilizing a microwave heat excitation provides advantages over traditional thermal excitations (heat lamps, etc.) including the potential for non-contact, selective and focused heating. During an AMT inspection, two heating mechanisms are possible, referred to as dielectric and induction heating. Dielectric heating occurs as a result of the interaction of microwave energy with lossy dielectric materials which results in dissipated microwave energy and a subsequent increase in temperature. Induction heating is a result of induced surface current on conductive materials with finite conductivity under microwave illumination and subsequently ohmic loss. Due to the unique properties of microwave signals including frequency of operation, power level, and polarization, as well as their interaction with different materials, AMT has strong potential for application in various industries including infrastructure, transportation, aerospace, etc. As such, this Dissertation explores the application of AMT to NDT&E needs in these important industries, including detection and evaluation of defects in single- or multi-layered fiber-reinforced polymer-strengthened cement-based materials, evaluation of steel fiber percentage and distributions in steel fiber reinforced structures, characterization of corrosion ratio on corroded reinforcing steel bars (rebar), and evaluation of covered surface cracks orientation and size in metal structures.

ACKNOWLEDGMENTS

First and foremost, I would like to thank my beloved wife and my best friend, Atieh Talebzadeh for her dedication, enthusiasm, and love. I believe I never could have embarked on my Ph.D. journey and finished it without an overwhelming support from her.

I would like to express my utmost gratitude to my advisor, Dr. Kristen M. Donnell, for her earnest support, inspirations, and the many hours she has devoted to me. Although this dissertation is an individual work, I could have never accomplished this without her help.

I am also grateful to thank Dr. Reza Zoughi, Dr. Jun Fan, Dr. David Pommerenke, and Dr. K. Chandrashekhara for serving on my committee and their valuable guidance.

I would also like to thank all my dear teachers, colleagues, and friends, in particular Dr. Mohammad Tayeb Ghasr for his guidance and mentorship during my research work, Prof. Jim Drewniak, Dr. Iman Mehdipour, Mr. Ali Mirala, Mr. Cody Edwards, Mr. Matthew Dvorsky, and Dr. Mojtaba Fallahpour for their collaborative work during my PhD program

I would like to acknowledge the American Society for Nondestructive Testing (ASNT) for financial support of this research under the 2015 Graduate Research Fellowship, the IEEE Instrumentation and Measurement Society (IEEE IMS) for the 2015 Graduate Research Fellowship, Center for Infrastructure Engineering Studies (CIES) at Missouri University of Science and Technology for their support, and National Science Foundation (NSF) for financial support of this research under award No. 1609470.

Last but not least, I am grateful with all of my being to my parents, Mohammad and Tahereh, for everything they gave me during my life. I would also like to thank my brother, Reza, for his guidance during my education. Special thanks to my sisters Maryam and Farideh for their support. I believe I never could have embarked on my Ph.D. journey and finished it without an overwhelming support from my lovely mother and father.

TABLE OF CONTENTS

Page

PUBLICATION DISSERTATION OPTION iii

ABSTRACT iv

ACKNOWLEDGEMENTS v

LIST OF ILLUSTRATIONS ix

LIST OF TABLES xiii

NOMENCLATURE xiv

SECTION

1. INTRODUCTION 1

1.1. ACTIVE MICROWAVE THERMOGRAPHY 3

1.2. ACTIVE MICROWAVE THERMOGRAPHY SIGNAL PROCESSING 5

1.3. RESEARCH OBJECTIVE 7

1.4. ORGANIZATION OF THE DISSERTATION 9

BIBLIOGRAPHY 12

PAPER

I. ACTIVE MICROWAVE THERMOGRAPHY FOR DEFECT DETECTION OF CFRP-STRENGTHENED CEMENT-BASED MATERIALS 14

ABSTRACT 14

1. INTRODUCTION 15

2. ACTIVE MICROWAVE THERMOGRAPHY 17

2.1. BASIC PRINCIPAL 17

2.2. AMT SIGNAL PROCESSING 20

3. ELECTROMAGNETIC-THERMAL SIMULATION 21

4. MEASUREMENTS 24

4.1. SAMPLE PREPARATION 24

4.2. AMT MEASUREMENTS AND DISCUSSION 26

5. CONCLUSION 35

REFERENCES 36

II. ACTIVE MICROWAVE THERMOGRAPHY FOR NONDESTRUCTIVE EVALUATION OF FRP-REHABILITATED CEMENT-BASED STRUCTURES 39

ABSTRACT 39

1. INTRODUCTION 40

2. ACTIVE MICROWAVE THERMOGRAPHY 41

3. ELECTROMAGNETIC-THERMAL MODELING 44

4. AMT MEASUREMENTS – A CASE STUDY 53

5. CONCLUSION 57

REFERENCES 58

III. EVALUATION OF STEEL FIBER DISTRIBUTION IN CEMENT-BASED MORTARS USING ACTIVE MICROWAVE THERMOGRAPHY 60

ABSTRACT 60

1. INTRODUCTION 61

2. ACTIVE MICROWAVE THERMOGRAPHY 63

3. RESEARCH METHODOLOGY 65

3.1. MATERIALS, MIXTURE PROPORTIONING, AND SAMPLE PREPARATION 66

3.2. TEST METHODS 67

3.2.1. Fresh And Hardened Properties Of FRCMS 67

3.2.2. AMT Measurements 69

4. NUMERICAL SIMULATION OF AMT 72

4.1. EFFECT OF EMBEDDED SINGLE FIBER ON SURFACE TEMPERATURE 73

4.2. EFFECT OF FIBER DISTRIBUTION ON SURFACE TEMPERATURE 76

5. TEST RESULTS 78

5.1. FRESH AND MECHANICAL PROPERTIES OF FRCMS 78

5.2. AMT RESULTS 80

6. CONCLUSIONS 88

REFERENCES 89

IV. CHARACTERIZATION OF CORRODED REINFORCED STEEL BARS BY ACTIVE MICROWAVE THERMOGRAPHY 92

ABSTRACT 92

1. INTRODUCTION 93

2. SIMULATIONS 94

3. MEASUREMENT RESULTS 98

4. CONCLUSION 100

REFERENCES 101

V. ACTIVE MICROWAVE THERMOGRAPHY FOR NONDESTRUCTIVE EVALUATION OF SURFACE CRACKS IN METAL STRUCTURES 102

ABSTRACT 102

1. INTRODUCTION 103

2. ACTIVE MICROWAVE THERMOGRAPHY 104

3. AMT SIMULATIONS 107

4. AMT MEASUREMENTS 115

5. CONCLUSION 121

REFERENCES 122

SECTION

2. CONCLUSIONS AND FUTURE WORK 125

VITA 129

LIST OF ILLUSTRATIONS

Page

PAPER I

Figure 1 - Illustration of an RCM with unbond, delamination, and crack defects 15

Figure 2 - Simulated TC for an unbond defect for parallel (Pr) and perpendicular (Pn) polarization 23

Figure 3 - Simulated TC for an unbond defect for perpendicular (Pn) polarization for various defect dimensions 23

Figure 4 - RCM samples with (a) an unbond, (b) delaminations, and (c) cracks 25

Figure 5 - The AMT (a) system configuration, (b) measurement setup 25

Figure 6 - Thermal profile of RCM sample with unbond defect for perpendicular polarization (a) surface temperature after 60 and 180 sec, (b) linear temperature profile after 60 sec 27

Figure 7 - Raw (n = 1) and median filtered (n = 3 and 5) surface thermal profile of the RCM with unbond after 180 sec of microwave illumination with parallel polarization 28

Figure 8 - (a) TC and (b) SNR, of RCM sample with unbond defect for perpendicular and parallel polarizations 29

Figure 9 - Surface thermal profile of RCM sample with delaminated defects for perpendicular polarization 31

Figure 10 - (a) TC and (b) SNR, of RCM sample with delaminated defects for perpendicular polarization 32

Figure 11 - Surface thermal profile of RCM sample with crack defects for perpendicular polarization 33

Figure 12 - (a) TC and (b) SNR, of RCM sample with crack defects for perpendicular polarization 34

PAPER II

Figure 1 - Illustration of plane wave excitation for microwave-induced heating 42

Figure 2 - Simulation model including boundary conditions for (a) electromagnetic and (b) thermal simulations 46

Figure 3 - Fiber direction parallel (a) and perpendicular (b) to the electric field polarization 47

Figure 4 - Simulated TC for an unbond for parallel and perpendicular (to the fiber direction) polarizations 48

Figure 5 - Simulated thermal profile for (a) case I, and (b) case IV. 50

Figure 6 - TC (K) as a function of frequency for case I (a), and case IV (b) 51

Figure 7 - The AMT system and measurement configuration 53

Figure 8 - Results after 5, 10, 20, 60, and 180 sec heating: (a) ΔT profile (defined in Eq, 11) for Pn-Pol, (b) SNR profile for Pn-Pol, (c) ΔT profile for Pr-Pol, and (d) SNR profile for Pr-Pol 56

Figure 9 - Temporal noise for both polarizations 57

PAPER III

Figure 1 - Experimental procedure for evaluating fiber inhomogeneity along cast prism in fresh state 69

Figure 2 - AMT measurement test setup 70

Figure 3 - Illustration of image acquisition 71

Figure 4 - Simulated surface temperature and induced surface current on fiber for sample with a single fiber a variation in fiber depth and b variation in sample loss factor 75

Figure 5 - Numerical modeling results of E-field and temperature variation for random (top row) and clumped (bottom row) fiber distributions 77

Figure 6 - Effect of fiber addition on flow and PFT covering fibers 78

Figure 7 - Load-deflection curves of investigated FRCMs 79

Figure 8 - Surface temperature variation of samples made with different fiber contents 80

Figure 9 - Histograms of surface temperature for samples made with different fiber contents 81

Figure 10 - Transient surface temperature of samples made with different fiber contents at operating frequency of 2.4 GHz 82

Figure 11 - Variation in mean value of surface temperature at different operating frequencies after 30 s heating 82

Figure 12 - Variation in mean value of surface temperature for 40 zones across each sample after 30 s heating 85

Figure 13 - Correlation between fiber density and mean of surface temperature for both simulations and measurements 87

Figure 14 - Correlation between surface temperature and normalized toughness of hardened samples with fiber homogeneity determined from freshly cast prism 87

PAPER IV

Figure 1 - Rebar cross-section (a) un-corroded, and (b) corroded 94

Figure 2 - Transient behavior of the corroded area of rebar at 2.5 GHz 96

Figure 3 - Effect of (a) corrosion thickness, and (b) frequncy, on normalized temperature of corrosion at t = 10 sec (left), and maximum SAR (right) 97

Figure 4 - AMT measurement set-up for corroded rebar (side and top view) 98

Figure 5 - Temperature profile of corroded rebar after 10 sec heating (C1, left, and C4, right) 99

Figure 6 - Measured results of (a) C2 and C4 at 2 GHz, and (b) C4 at frequenciey of 2, 2.5 and 3 GHz 100

PAPER V

Figure 1 - Top view of a simulated steel structure with a filled and covered crack 108

Figure 2 - Simulated normalized E-field as a function of position along the crack length with l = 40 mm for below (0.4 GHz) and above cut-off (1.2 GHz). 109

Figure 3 - Simulated TC as a function of frequency 110

Figure 4 - Simulated temperature rise after 60 sec microwave heating 112

Figure 5 - Simulated TC as a function of time for various crack orientation angles ... 113

Figure 6 - Simulated *TC* as a function of crack orientation angle 113

Figure 7 - Simulated TC for various crack width at $\phi = 0°$ 114

Figure 8 - (a) Top view of metal sample with surface crack, and (b) illustration of the AMT measurement set up. 117

Figure 9 - Measured (a) TC and (b) SNR for various crack orientation angles with 15 cm lift-off 118

Figure 10 - Measured (a) TC and (b) SNR 119

Figure 11 - Measured (a) TC and (b) SNR for two different lift-off 120

LIST OF TABLES

Page

PAPER I

Table 1 - Electromagnetic and thermal properties of materials 19

Table 2 - Thermal response of RCM with perpendicular and parallel polarization illumination 30

PAPER II

Table 1 – Electromagnetic-thermal properties of materials 45

Table 2 - TC (K) for an unbond in a rehabilitated CM with two layers of CFRP, the CM is assumed to be flush with the 2nd layer indicated below 49

Table 3 - TC (K) as a function of source power 52

PAPER III

Table 1 - ANOVA results at 2.4 GHz 84

PAPER IV

Table 1 - Thermal Properties of Materials 95

PAPER V

Table 1 - Microwave and Thermal Properties 108

NOMENCLATURE

Symbol	Description
α	attenuation constant
β	phase constant
f	frequency
ε	dielectric properties
ε_r	relative (to free-space) dielectric constant
ε_0	free-space dielectric constant
ε'_r	permittivity
ε''_r	loss factor
μ_r	relative (to free-space) permeability
μ_0	free-space permeability
σ	conductivity
k	thermal conductivity
C	specific heat
ρ	material density
T	temperature
t	time
Q	dissipated (microwave) energy
E	electric-field
H	magnetic field
J	induced surface current
S	poynting vector
ΔT	temperature rise
T_a	ambient temperature
T_D	defect area temperature
T_S	sound area temperature
TC	thermal contrast
SNR	signal-to-noise ratio
σ_N	standard deviation of sound area

SECTION

1. INTRODUCTION

Nondestructive testing and evaluation (NDT&E) and structural health monitoring of composite infrastructure and aerospace structures is a challenging issue to fully address with traditional NDT&E techniques. It can often be quite difficult to use a single modality for a complete inspection of structures or materials due to the complexity and variation in material type (such as metals, dielectrics, etc.). Among various NDT&E methods, microwave NDT has been successfully applied for inspection of dielectric materials (including composite and cement-based material), crack detections in metal or corrosion under the paint, but cannot inspect for subsurface defects in or beneath conductive materials [1]. In addition, microwave inspections often require raster scanning for large areas of interest which may result in significant inspection times [2]. Another well-established technique is the mechanical wave method (e.g., ultrasonic inspection). The main limitation of the ultrasonic method is that an expert operator is often required. In addition, contact between the mechanical transducer and material under inspection is also often required [3]. X-ray and computed tomography are also promising NDT tools, but include significant safety concerns [4]. Thus, these techniques are more challenging to apply in the field. Shearography has shown promise in terms of defect detection, but the high equipment cost limits its use [5]. Thermography, or the thermal wave method, is another inspection method that has shown promise for many applications in NDT [6]-[12]. Thermography can be utilized in an active or passive mode. Since passive thermography utilizes a solar energy excitation, it is limited in application (i.e., solar energy must be available). However, active thermography (that utilizes an external heat source) [6]-[7] has been successfully applied for a number of structural health monitoring applications including defect detection in composite materials. Active thermography conventionally requires high power heat sources (usually a flash heat lamp) in order to generate enough thermal contrast to facilitate detection of surface or subsurface defects. However, the main limitation is that the energy cannot be targeted to an area of interest, but rather is applied over a large area.

To this end, other modalities have been considered to provide the thermal excitation including ultrasonic [8], induction current or eddy current [9], and most recently, a microwave excitation [10]-[12]. In ultrasonic thermography, ultrasonic energy is transformed into heat through friction where defects are present. Therefore, defects act as internal heat sources, while undamaged areas show almost no temperature increase. However, ultrasonic thermography is a contact-based method, as the ultrasound transducer needs to be in contact with the material to be inspected in order to couple the ultrasonic energy into the material.

In the last decade, researchers have shown an increased interest in using a microwave heat excitation for thermographic inspections. The combination of a microwave excitation and subsequent thermal measurement is herein referred to as Active Microwave Thermography (AMT), and has shown strong potential for inspection of:

carbon-fiber reinforced polymer laminate in rehabilitated cement-based materials,

steel fiber distribution in steel fiber reinforced cement-based materials,

corrosion on metal structures, and

covered surface cracks in metal structures, amongst others.

Utilizing a microwave excitation offers unique advantages including the application of controlled and localized microwave energy, remote (non-contact) inspection, and the ability to tailor the evaluation to the inspection need through choice of frequency and polarization of the microwave signal. A significant advantage of the integration of these two techniques lies in the ability to capitalize on the properties of microwave signals. More specifically, microwaves readily penetrate dielectric materials (i.e., composites), and are also sensitive to surface damage in conductive materials (e.g., carbon-fiber composites). Further, AMT takes advantage of the well-developed area of thermography, utilizing commercially-available thermal cameras to capture easy-to-interpret surface thermal images of a structure or material under test.

1.1. ACTIVE MICROWAVE THERMOGRAPHY

There are two types of heating mechanisms in AMT, referred to as dielectric heating and induction heating. As it relates to dielectric heating, dielectric materials are defined by their complex relative (to free-space) dielectric properties, defined as:

$$\varepsilon_r = \varepsilon_r' - j\varepsilon_r'' \tag{1}$$

The real (permittivity) and imaginary (loss factor) parts represent the ability of a material to store and absorb microwave energy, respectively. As dielectric heating is caused by the absorption of microwave energy, in order to quantitatively determine the amount of heat generated, the electric field inside the dielectric material must be known. To this end, a uniform plane wave is assumed to propagate in an unbounded lossy medium in the *z*-direction ($\hat{z}$) with an electric-field (*E-field*) component polarized in the *x*-direction ($\hat{x}$) and a magnetic field (*H-field*) component polarized in y-direction ($\hat{y}$). To consider the effect of thermal diffusion and convection from this material to air, an infinite half-space of this material is assumed with the air-dielectric interface at $z = 0$. Also, the plane wave is assumed to originate in air (i.e., $z < 0$) and propagates toward the dielectric. Thus, the *E-field* ($\vec{E}$) and *H-field* ($\vec{H}$) can be expressed as [13]:

$$\vec{E} = \hat{x}E_0 e^{-\gamma z} \tag{2}$$

$$\vec{H} = \hat{y}\frac{E_0}{\sqrt{\mu_0\mu_r / \varepsilon_0\varepsilon_r}}e^{-\gamma z} \tag{3}$$

where E_0 is the amplitude of the *E-field* at the material interface ($z = 0$) and is related to the incident microwave power. Also, μ_0 is the permeability of the fee-space, μ_r is the relative permeability of the material, ε_0 is the free-space dielectric constant, and γ is the propagation constant that is defined as:

$$\gamma = \sqrt{j\omega\mu_0\mu_r\, j\omega\varepsilon_0\varepsilon_r} = \omega\sqrt{\varepsilon_0\mu_0}\sqrt{-\varepsilon_r' + j\varepsilon_r''} = \alpha + j\beta \tag{4}$$

where α (Np/m) is the attenuation constant, β (rad/m) is the phase propagation, and ω is the radian frequency of the electromagnetic wave. To determine the complex power associated with a propagating plane wave, the Poynting vector, $\vec{S}$, is defined as:

$$\vec{S} = \vec{E} \times \vec{H}^* = \frac{\sqrt{\varepsilon_0}}{\sqrt{\mu_0}} (\sqrt{\varepsilon_r})^* \left|E_0\right|^2 e^{-2\alpha z} \tag{5}$$

And subsequently, the dissipated (absorbed) power, *Q*, can be determined as:

$$Q = -\mathrm{Re}(\nabla . \vec{S}) = \omega \varepsilon_0 \varepsilon_r'' \left|E_0\right|^2 e^{-2\alpha z} \tag{6}$$

As seen from Eq. 6, the amplitude of the *E-field* decrease as it propagates inside the dielectric material and subsequently the available power attenuates as the energy travels through the material as well.

From the above discussions, when a lossy dielectric is irradiated with microwave energy, dielectric heating as a result of absorbed power occurs. For dielectric materials, the volumetric heating as a result of dissipated power can be expressed as:

$$\rho C \frac{\partial T(x,y,z)}{\partial t} = \nabla . (k \nabla T(x,y,z)) + Q(x,y,z) \tag{7}$$

where k (W/m.K) is the thermal conductivity, C (J/g.K) is the specific heat, ρ (Kg/m^3) is the material density, t (sec) is the time, and T (K) is the temperature at each point (x,y,z) inside the dielectric. Finally, from Equation (7), the temperature at heating time, t, resulting from the absorbed microwave power under constant plane wave illumination can be simplified as follow:

$$T = \frac{Qt}{\rho C} = \frac{\omega \varepsilon_0 \varepsilon_r'' \left|E\right|^2 t}{\rho C} \tag{8}$$

Induction heating occurs when an electromagnetic wave impinges upon a conductive material with (finite) conductivity of σ (S/m). In this case, microwave energy cannot penetrate through the conductor. Rather, surface current, $\vec{J}_{ind}$, is induced on the surface of the conductor and is given as follows:

$$\vec{J}_{ind} = \hat{n} \times \vec{H}_{inc} \tag{9}$$

where $\hat{n}$ is the normal (to the plane of the conductor) unit vector, and $\vec{H}_{inc}$ is the incident *H-field*. Due to the finite σ, ohmic loss (per unit volume) occurs which can be expressed based on the Lorentz force equation and Newton's equation of motion, as follows [14]:

$$\frac{\partial P_{loss}}{\partial V} = \vec{J}_{ind} . \vec{E}_{inc} \tag{10}$$

where $\vec{E}_{inc}$ is the incident *E-field*. In addition, this induced surface current serves as a source of radiated (or scattered) microwave energy which in turn may be absorbed by nearby dielectric materials (e.g., corrosion on steel etc.).

1.2. ACTIVE MICROWAVE THERMOGRAPHY SIGNAL PROCESSING

During an AMT inspection, prior to microwave illumination, the surface thermal profile of the structure or material under test as measured by the thermal camera is a result of ambient conditions (due to the environment). Subsequently, once under microwave illumination, the temperature increase is defined as:

$$\Delta T(t) = T(t) - T_a \tag{11}$$

where $\Delta T(t)$ is the temperature difference at time t, $T(t)$ is the (absolute) temperature observed at time t, and T_a is the (absolute) temperature prior to microwave illumination

(i.e., ambient conditions). To quantitatively assess the thermal images, the thermal contrast (*TC*) between a defective and a sound (i.e., defect-free) area is considered and is defined as:

$$TC = \Delta T_D(t) - \Delta T_S(t) \tag{12}$$

where $\Delta T_D(t)$ and $\Delta T_S(t)$ are:

$$\Delta T_D(t) = T_D(t) - T_{aD} \tag{13}$$

$$\Delta T_S(t) = T_S(t) - T_{aS} \tag{14}$$

where $T_D(t)$ and $T_S(t)$ are the temperatures of the defective and sound areas at time, *t*, respectively, and T_{aD} and T_{aS} are the ambient temperatures of the defective and sound areas prior to microwave illumination, respectively. Practically speaking, in order to be able to detect the presence of a defect after a heating time of *t*, the *TC* must be greater than the sensitivity of the thermal camera used to capture the thermal images.

In practice, it is expected that AMT inspection results will be affected by temporal noise (e.g., environmental, system, thermal camera, etc.). As such, the signal-to-noise ratio (*SNR*) can be used to describe the contrast between a defective and sound area. To this end, in order to calculate the *SNR*, the signal is defined as the *TC* and the temporal noise is defined based on the standard deviation of temperature in a sound area (thereby representing noise in the thermal image). Therefore, the *SNR* of the measured thermal data is expressed as:

$$SNR = 20\log_{10}\frac{TC}{\sigma_S} \tag{15}$$

where σ_S is the standard deviation of temperature of the sound area. Generally speaking, in order to be able to detect a defect, the difference between the *SNR* at the defective area

and that of an adjacent sound area should be greater than 0 dB [15]. However, the actual value required for successful detection in practice will depend on the application, system, environment, etc.

1.3. RESEARCH OBJECTIVE

As mentioned earlier, developing a new NDT&E tool that can overcome limitations of other techniques for different applications is always of interest. To this end, the development of AMT is the objective of this dissertation for various industries including transportation/infrastructure and aerospace. Thus, the focus of this dissertation is to study the potential for AMT to detect defects in structures rehabilitated with carbon fiber reinforced polymers (CFRP), evaluate the steel fiber distribution in structures reinforced with the same, and detect corrosion on steel bars (rebar) and surface cracks under coatings.

Composite materials, including carbon fiber reinforced polymers (CFRP), are widely applied (in laminate sheets) to beams and slabs or wrapped around columns (and bonded using adhesives such as epoxy resins) to enhance the mechanical performance of cement-based structural elements. Thus, the bond quality between the CFRP sheets and cement-based materials is of high importance to the short- and long-term structural integrity and durability of these rehabilitated structures. Three common types of defects, referred to as unbond, delamination, and crack, are of concern to such rehabilitated structures. Typically, CFRPs used for rehabilitation are uni-directional. When CFRPs are made into laminate sheets, their interaction with microwave energy is strongly influenced by the relative orientation of the fibers with respect to the polarization of the incident microwave signal. Consequently, for uni-directional CFRP, microwave signals can penetrate through the sheet when the fiber direction is orthogonal to the polarization of the microwave signal and thus, the material behaves as a lossy dielectric. However, when the CFRP fiber direction is parallel to the polarization of the incident microwave signal, the incident signal is reflected from the laminate, resulting in very little signal penetration.

As mentioned before, inspection of CFRP laminate in rehabilitated structures for defect detection is important. For some applications, multiple layers of uni-directional CFRP laminate will be attached to the structure for improved mechanical strength. In addition, in order to improve the mechanical strength in two orthogonal directions, two separate layers of uni-directional CFRP (orthogonally placed) can be used. As such, since defects can occur between these CFRP layers, it is also important to be able to assess these multilayered structures. As such, AMT is considered as a viable inspection tool for this application, and the efficacy of the method is quantified through the *TC* and *SNR*.

Cement-based materials are typically characterized as brittle materials, with relatively low tensile strength and strain capacity [16]. Fibers can be incorporated to reduce cracking tendency and improve post-cracking response and energy absorption capacity. In fiber-reinforced cement-based materials, parameters including fiber content, geometry, and type have an effect on workability and rheological properties, as well as mechanical characteristics of cement-based materials. In addition, the effectiveness of incorporating fibers to enhance mechanical properties of cement-based materials is significantly affected by the fiber distribution. Non-uniform fiber distribution can lead to mechanical anisotropy in some regions of a structural element, resulting in an undesirable variability in mechanical performance of fiber-reinforced cement-based materials. Given the interaction between fibers, the incorporation of fibers can result in a reduction in the workability of steel fiber reinforced cement-based materials. In the case of relatively low steel fiber volume, the workability of steel fiber reinforced cement-based materials may not be significantly affected, given the lower level of potential interaction and larger distance between individual steel fibers. As steel fiber volume increases, the interaction between fibers increases, thus reducing workability. Beyond a certain fiber content, the interaction among fibers can substantially increase, potentially leading to the formation of fiber clumping (or fiber balling). Fiber clumping can form a non-uniform fiber distribution throughout the mixture, which can result in significant reduction in workability and mechanical properties. As such, AMT is considered as a viable inspection tool for this application, and the efficacy of the method for evaluation of fiber percentage and distribution as well as fiber clumping detection is quantified through the *TC* and correlation between mechanical testing with AMT results.

Corrosion is defined as the deterioration of a metal surface as a result of chemical reactions between metal and the surrounding environment. Both the type of metal and the environmental conditions determine the form and rate of deterioration. Corrosion is a complicated science that requires in-depth knowledge of chemistry, metallurgy, coatings, and environmental condition. Corrosion can happen on a large (e.g., entire surface) or localized (e.g., pitting) scale. Determine the presence of corrosion and also characterizing the corrosion ratio on the metal surface is of high importance to the transportation and aerospace industries since it can lead to structural failure due to degradation in mechanical performance. Therefore, AMT is considered as a feasible inspection tool for this inspection need, and parameters including the effect of frequency, and corrosion ratio are studied via their effect on the *TC*.

Surface cracks in metal structures result from large stresses, cyclical loading, and environmentally accelerated phenomena (i.e., corrosion) can occur in an aircraft fuselage, turbine blades, railroad and steel-bridge infrastructure, and oil and gas pipelines. Cracks can be visible or hidden under coatings (intentional such as paint or unintentional such as corrosion). Surface cracks on metal under coatings and/or filled with dielectric materials such as paint, rust, or dirt are not always reliably detected using conventional nondestructive testing and evaluation (NDT&E) methods. Therefore, AMT is considered as a viable inspection tool for this inspection need, and the effectiveness of the technique is quantified through consideration of the effect of parameters including crack dimensions and orientation on the *TC* and *SNR*.

.

1.4. ORGANIZATION OF THE DISSERTATION

As mentioned, the research objective of this work is to study the potential for AMT to detect defects in structures rehabilitated with carbon fiber reinforced polymers (CFRP), evaluate the steel fiber distribution in structures reinforced with the same, and detect corrosion on rebar and surface cracks under coatings. As such, for each of these potential applications, simulations were developed and utilized to study the various scenarios mentioned above. Then, representative measurements were conducted for each

application to further support the results and conclusions. The most relevant and critical outcomes are outlined in this dissertation, and are reported in the following papers:

In Paper I, the application of AMT for detection of various types of defects in CFRP-strengthened structures is presented. It is shown that microwave energy cannot penetrate through CFRPs when the *E-field* polarization is parallel to the fiber orientation. However, due to induction heating, the presence of a defect can still be determined. Also, the minimum required heating time for which an *SNR* of greater than 0 dB is achieved is studied. It is concluded that at least ~5 sec is required for successful detection of defects in such structures. In addition, it is observed that the *SNR* saturates as microwave illumination continues. From this, the maximum effective heating time can also be determined and for this type of inspection is ~60 sec.

In Paper II, the application of AMT for detection of defects at different interfaces within a multilayered CFRP laminate (placed on a structure/substrate) is investigated. For a two-layer CFRP laminate, there are 8 possible cases for the location of the defect. These cases are a result of the orientation of CFRP layers with respect to the *E-field* polarization of the incident wave and also the defect location (between CFRP layers or at the structure-CFRP interface). It is shown that the *TC* differs for each case, meaning an indication of defect location is possible from an AMT inspection.

In Paper III, the application of AMT for steel fiber evaluation in fiber-reinforced cement-based materials is presented. In this type of structure, both heating mechanisms occur. It is observed that fiber depth and dielectric properties of mortar have a significant influence on the *TC*. In addition, it is also observed that due to the increase in induction heating with increasing fiber percentage, the *TC* increases. However, it is shown that the samples containing 1% and 2% steel fibers (by volume) have a higher *TC* as compared to a sample made with 3% fiber content. This is attributed to the non-uniform fiber distribution and potential fiber clumping that results when the fiber content increases past an optimal level (i.e., 3%). Lastly, mechanical tests were also conducted on these samples, and a good correlation between the *TC* and mechanical test results was achieved.

In Paper IV, the application of AMT for characterization of corrosion in steel bridges or reinforcing rebar in concrete is investigated. First, in order to ensure optimal

interaction with the illuminating microwave signal and corrosion, the rebar has to be parallel to the *E-field* polarization in order to cause the maximum induced current and subsequent scattering from the rebar. To this end, a rebar with several corroded areas is considered in order to investigate the percentage of corrosion present. It is shown that a higher percentage of corrosion leads to increased absorption of microwave energy as well as a greater *TC*. Moreover, increasing frequency leads to a greater temperature difference as well. Overall, AMT is shown to have potential to serve as a detection and characterization tool for corrosion detection and characterization.

In Paper V, AMT is investigated for detection and evaluation of covered cracks in metal structures (in particular, cracks in 1008 steel covered by and filled with corrosion). In general, since corrosion is a lossy dielectric and the underlying material is conductive, both dielectric and induction heating will take place when such a structure is under microwave illumination. However, the contribution to the heat generated from induction heating is limited, making the primary heating mechanism dielectric heating. In addition, it is shown that maximum heat generation occurs when the crack is perpendicular to the *E-field* polarization. More specifically, at the presence of the crack (depending on the frequency of the incident signal, crack dimensions, dielectric properties of filling materials, and also boundary conditions), a propagating mode TE_{10} may be set up at the crack meaning the crack will act like a very short in length waveguide with the broad dimension corresponding the length of the crack. In addition, the relationship between the *TC* and dissipated microwave energy (and subsequent heat generation) is proportional to $\cos^2(\phi)$, where ϕ is the angle between the *E-field* polarization and direction perpendicular to crack length (meaning maximum heat generation occurs when $\phi = 0$). Thus, according to the minimum sensitivity of the current AMT system thermal camera, a crack with an orientation angle of $\phi = 65°$ can be detected.

BIBLIOGRAPHY

[1] R. Zoughi, "Microwave non-destructive testing and evaluation principles" vol. 4, Springer Science & Business Media, 2000.

[2] A. Foudazi, T. E. Roth, M. T. Ghasr, and R. Zoughi, "Aperture-coupled microstrip patch antenna fed by orthogonal SIW line for millimetre-wave imaging applications," IET Microwaves, Antennas & Propagation vol. 11, no. 6, pp. 811-817, 2016.

[3] M. Ricci, L. Senni, and P. Burrascano, "Exploiting pseudorandom sequences to enhance noise immunity for air-coupled ultrasonic nondestructive testing," IEEE Transactions on Instrumentation and Measurement, vol. 61, no. 11, pp. 2905-2915, 2012.

[4] S. C. de Wolski, J. E. Bolander, and E. N. Landis, "An in-situ X-ray microtomography study of split cylinder fracture in cement-based materials," Experimental Mechanics, vol. 54, no. 7, pp. 1227-1235, 2014.

[5] Y. Y. Hung, Y. S. Chen, S. P. Ng, L. Liu, Y. H. Huang, B. L. Luk, R. W. L. Ip, C. M. L. Wu, and P. S. Chung, "Review and comparison of shearography and active thermography for nondestructive evaluation," Materials Science and Engineering: R: Reports, vol. 64, no. 5, pp. 73-112, 2009.

[6] C. Ibarra-Castanedo, and X. Maldague, "Infrared thermography," Chapter 10, In Handbook of Technical Diagnostics, pp. 175-220. Springer Berlin Heidelberg, 2013.

[7] R. Yang, and Y He, "Optically and Non-optically Excited Thermography for Composites: A Review," Infrared Physics & Technology, vol. 75, pp. 26-50, 2016.

[8] J. G. Thompson, and C. T. Uyehara, "Ultrasonic thermography inspection method and apparatus," U.S. Patent 7,075,084, 2006.

[9] D. Vasic, V. Bilas, and D. Ambrus, "Pulsed eddy-current nondestructive testing of ferromagnetic tubes," IEEE Transactions on Instrumentation and Measurement, vol. 53, no. 4, pp. 1289-1294, 2004.

[10] D. Balageas, and P. Levesque, "Mines detection using the EMIR® method," In QIRT, pp. 71-78, 2002.

[11] C. A. DiMarzio, C. M. Rappaport, W. Li, M. E. Kilmer, and G. O. Sauermann, "Microwave-enhanced infrared thermography," In International Society for Optics and Photonics, Photonics East (ISAM, VVDC, IEMB), pp. 337-342, 1999.

[12] S. Keo, D. Defer, F. Breaban, and F. Brachelet, “Comparison between microwave infrared thermography and CO2 Laser infrared thermography in defect detection in applications with CFRP,” Materials Sciences and Applications, vol. 4, pp. 600-605, 2013.

[13] C. A. Balanis, “Advanced engineering electromagnetic,” John Wiley & Sons, 1999.

[14] S. Orfanidis; Electromagneticwaves and antennas. New Brunswick, NJ: Rutgers University, 2002.

[15] K. Srinivas, A. O. Siddiqui, and J. Lahiri, “Thermographic inspection of composite materials,” In Proc. National Seminar on Non-Destructive Evaluation, vol. 12, pp. 7-9, 2006.

[16] L. Ferrara, Y. Park, and S. Shah, “A method for mix-design of fiber-reinforced self-compacting concrete,” Cement and Concrete Research, vol. 37, no. 6, pp. 957-971, 2007.

PAPER

I. ACTIVE MICROWAVE THERMOGRAPHY FOR DEFECT DETECTION OF CFRP-STRENGTHENED CEMENT-BASED MATERIALS

ABSTRACT

Nondestructive testing of rehabilitated cement-based materials with carbon fiber reinforced polymer (CFRP) composites is quite important in the transportation and infrastructure industries. Among various nondestructive testing methods, Active Microwave Thermography (AMT) has shown good potential. This method uses microwave energy to heat a structure of interest, and subsequently the surface thermal profile is measured using a thermal camera. In this paper, the application of AMT for defect detection (unbond, delamination and crack) in CFRP composites used in rehabilitated cement-based materials is presented. More specifically, the effect of defect size and depth and polarization on the resultant surface thermal profile with defects is first studied through simulation. The effect of polarization on detection of defects with regards to the orientation of CFRP fibers is also experimentally investigated. Finally, a quantitative analysis of the measured results based on the thermal contrast and signal-to-noise ratio (*SNR*) for all three aforementioned defect types is presented. The results show that the *SNR* is improved when utilizing perpendicular (as compared to parallel) polarization and that the maximum effective heating time is ~60 seconds, even for small defects.

Index Terms—nondestructive testing; active microwave thermography; defect detection; rehabilitated cement-based materials; carbon fiber reinforced polymer.

1. INTRODUCTION

Nondestructive testing (NDT) of infrastructure is quite important as it relates to inspection of cement-based materials and composite materials utilized in the transportation and infrastructure industries. Fiber reinforced polymer has become an important and widely accepted material for rehabilitation of deteriorating concrete structures due to its chemical stability, high mechanical strength and low density [1]. These polymers, including carbon fiber reinforced polymers (CFRP), are applied (in laminate sheets) to beams and slabs or wrapped around columns to enhance the mechanical performance of the structural element. The CFRP laminates are bonded to cement-based materials using an adhesive such as epoxy resins. Therefore, the bond quality between the CFRP sheets and cement-based materials is of high importance to the short- and long-term structural integrity and durability of these rehabilitated structures.

Three common types of defects referred to as unbond, delamination, and crack are of concern to such rehabilitated structures and are illustrated in Figure 1.

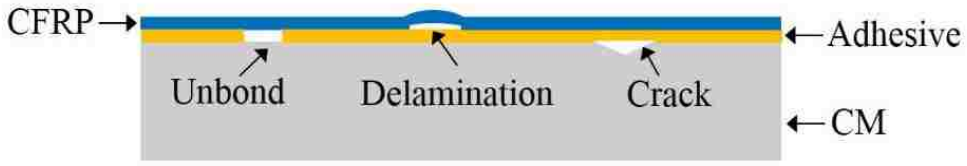

Figure 1 - Illustration of an RCM with unbond, delamination, and crack defects

An unbond defect occurs due to poor workmanship during the initial application of the CFRP strips to the CM surface which leads to entrapped air voids. A delamination is formed due to a chemical/physical degradation of the adhesive bonding layer (i.e. epoxy resin) when the composite is exposed to aggressive environments (including temperature variations, moisture, etc.). When this degradation occurs, the bond quality (strength) is reduced and thus a delamination may occur. Cracking may occur under the CFRP/adhesive layer if the RCM undergoes an impact, or due to other environmental causes such as chloride ingress, creation of alkali silica reaction gel, etc. Several visual inspection [2] and NDT methods including microwave [3]-[6], ultrasound [7], x-ray [8],

shearography [9], and thermography (active and passive) [10]-[17] have been applied to the infrastructure industry with varying levels of success. Among these NDT methods, microwave NDT has been successfully applied for inspection of dielectric materials (including composite and cement-based material), but cannot inspect for subsurface defects in or beneath conductive materials. Also, raster scanning of large areas of interest often requires significant inspection time. Sonic methods are well-established techniques. However, operator expertise and contact between the sonic transducer and material are often required. X-ray methods are quite promising, but include significant safety concerns, making this technique more challenging to apply in practice. Shearography has shown promise in terms of defect detection, but the high equipment cost limits its use. Thermography, both active and passive, is another inspection method that has shown promise for NDT of CMs. Since passive thermography utilizes a solar energy excitation, it is limited in application. However, active thermography has been successfully applied for a number of structural health monitoring applications including defect detection in composite materials [10]. Most of the conventional pulse-based active thermographic methods (pulsed and pulsed phase thermography) require high peak power heat sources in order to generate enough thermal contrast to facilitate detection of surface or subsurface defects. Conversely, modulated thermal imaging modalities (lock-in, frequency modulated, etc.) modulate the heat source over a specific time interval, thereby increasing the average power delivered to the material under test while improving detection capabilities [17]. However, the energy cannot be targeted to an area of interest, but rather is applied over a large area. To this end, other modalities have been considered for the thermal excitation including ultrasonic [18], induction current or eddy current [19]-[20], microwave for mines detection [21], [22], and most recently microwave excitation for transportation and aerospace industries [23]-[28]. In ultrasonic thermography [18], ultrasonic energy is transformed into heat through friction where defects are present. Defects therefore act as internal heat sources, while undamaged areas show almost no temperature increase. However, ultrasonic thermography is a contact-based method, as the ultrasound transducer needs to be in contact with the material to be inspected in order to couple the ultrasonic energy into the material. Eddy current thermography [19] utilizes an induction heating mechanism which restricts the method to

primarily conductive materials (or inspections in the vicinity of a conductive material [20]). The combination of microwave NDT and thermography, herein referred to as Active Microwave Thermography (AMT), has shown promise for steel fiber detection in reinforced concrete [24], [25], corrosion detection and characterization of steel [26], and delamination and unbond detection in carbon fiber reinforced composites [27],[28]. Utilizing a microwave excitation offers unique advantages including the application of controlled and localized microwave energy, remote (noncontact) inspection, and the ability to tailor the evaluation to the inspection need through choice of frequency and polarization of the microwave signal (amongst others). Further, AMT utilizes commercially-available thermal cameras to capture easy-to-interpret surface thermal images of a structure under test.

As such, this paper investigates a new application of AMT as an NDT tool for inspection of rehabilitated cement-based materials (RCMs). Numerical modeling of defect detection in rehabilitated cement-based structures by AMT is conducted by utilizing a coupled electromagnetic-thermal model using CST MultiPhysics Studio™ [29]. The effect of defect depth and size, as well as polarization of the incident microwave energy on the thermal response is studied using this model. Then, the potential for AMT as an inspection tool for RCMs is further investigated through representative measurements.

2. ACTIVE MICROWAVE THERMOGRAPHY

2.1. BASIC PRINCIPAL

As discussed above, AMT is based on the integration of microwave and thermographic techniques. For a microwave (heat) excitation, two different heating mechanisms based on dielectric heating or induced current may take place depending on the material properties of the material under test. Dielectric materials are defined by their complex relative (to free-space) dielectric properties, $\varepsilon_r = \varepsilon_r' - j\varepsilon_r''$. The real (permittivity) and imaginary (loss factor) parts represent the ability of a material to store and absorb microwave energy, respectively. Thus, when a lossy dielectric is irradiated with

microwave energy, the amount of dissipated heat Q (W/m^3) at each point inside the dielectric is related to the free space dielectric constant (ε_0), relative loss factor (ε_r''), frequency (f), and the RMS magnitude of the electric field (E) at that point as follows:

$$Q = 2\pi\varepsilon_0\varepsilon_r''\left|E_0\right|^2 \tag{1}$$

As such, transient heat diffusion occurs and is related to the thermal properties of material(s) and source of heat (i.e., Q), as follows:

$$\rho C_T \frac{\partial T}{\partial t} = K_T \nabla^2 T + Q \tag{2}$$

where K_T is the thermal conductivity (W/m.K), C_T is the specific heat (J/g.K), ρ is the density (Kg/m^3), t is the time (sec), and T is the temperature (K).

The second heating mechanism in AMT occurs when an electromagnetic wave impinges upon a conductive material. In this case, surface currents are induced on the surface of conductor. Such surface currents serve as a source of radiated (or scattered) electromagnetic energy which in turn may be absorbed by nearby dielectric materials (resulting in additional heat generation). Furthermore, due to the limited electric conductivity of the material, ohmic losses also occur. As such, for conductive materials, both the scattered electric field and ohmic losses contribute to the induced heat.

Microwave signals do not penetrate into carbon-based materials, as carbon is a decent conductor (σ = 10^4 S/m). As it relates to RCMs with CFRP, when carbon fibers are made into laminate sheets, their interaction with microwave energy is strongly influenced by the relative orientation of the fibers with respect to the polarization of the incident microwave signal. Consequently, for unidirectional CFRP, microwave signals can penetrate through the sheet when the fiber direction is orthogonal to the polarization (CFRP$\perp$) of the microwave signal and the material behaves as a lossy dielectric [5]. However, when the CFRP fiber direction is parallel (CFRP ||) to the polarization of the incident microwave signal, the incident signal is reflected from the laminate, resulting in

very little signal penetration. Thus, the effect of polarization on heat distribution and consequently its effect on defect detectability is of interest for this type of inspection.

Since AMT is based on a coupled electromagnetic-thermal relationship, the dielectric and thermal properties of material(s) under test determine the induced heat and subsequent heat diffusion. In Table 1, the dielectric and thermal properties, including the thermal conductivity (K_T), specific heat (C_T), and density (ρ) of materials relevant to this work are provided [5], [24]-[28]. As CFRP is the outer layer of a rehabilitated structure and is an electrically conductive material, when the fiber orientation is parallel to the signal polarization, the only heating mechanism (in this case) is a result of the induced surface current on the CFRP. However, when the fiber orientation is perpendicular to the signal polarization, the signal penetrates through to the underlying CM, resulting in dielectric heating. As seen in the Table 1, by comparing the thermal conductivity of air (0.026 W/m.K) and adhesive (1.0 W/m.K), air behaves as a thermal insulator between layers of CFRP and cement-based material, while adhesive is a better thermal conductor (in comparison with air). Hence, it is expected that the defects considered here (delamination, unbond, and crack) will experience a larger temperature difference from ambient than healthy areas when monitoring the surface of the sample and will therefore appear as hot spots in thermal images.

Table 1 - Electromagnetic and thermal properties of materials

Material	EM Properties	K_T(W/m.K)	C_T(J/g.K)	ρ (Kg/m^3)
Air	$\varepsilon_r = 1$	0.026	1.005	1.204
Foam	$\varepsilon_r \approx 1$	0.03	1.3	30
Adhesive	$\varepsilon_r \approx 6\text{-}j0.6$	1.0	3.7	1100
CM	$\varepsilon_r \approx 4.7\text{-}j0.7$	1.7	0.8	2400
CFRP$\parallel$	$\sigma = 10^4$	7	1.2	1600
CFRP$\perp$	$\varepsilon_r \approx 7\text{-}j2.5$	0.8	1.2	1600

2.2. AMT SIGNAL PROCESSING

During an AMT inspection, prior to microwave illumination, the surface thermal profile represents the ambient response (due to the environment) of the material. Subsequently, once under microwave illumination, the temperature increase is defined as:

$$\Delta T(t) = T(t) - T_a \tag{3}$$

where $\Delta T(t)$ is the temperature difference at time t, $T(t)$ is the (absolute) temperature observed at time t, and T_a is the (absolute) temperature prior to microwave illumination (i.e., ambient conditions). To quantitatively assess the thermal images, the thermal contrast between defective and sound (i.e., defect-free) areas, $TC(t)$, is considered and is defined as [13]:

$$TC(t) = [T_D(t) - T_{aD}] - [T_S(t) - T_{aS}] \tag{4}$$

where $T_D(t)$ and $T_S(t)$ are the temperatures of the defective and sound areas at time t, respectively, and T_{aD} and T_{aS} are the ambient temperatures of the defective and sound areas prior to microwave illumination, respectively. Practically speaking, in order to be able to detect the presence of a defect after a heating time of t, the TC must be greater than the sensitivity of the thermal camera used to capture the thermal images.

In practice, it is expected that AMT inspection results will be affected by noise (environmental, system, thermal camera, etc.). As such, the signal-to-noise ratio (SNR) can be used to describe the contrast between a defective area and its surrounding (sound) region to establish a dynamic range for measured data. To this end, in order to calculate the SNR, the signal is defined as the TC and the noise level is based on the variation of temperature difference in a sound area (representing noise in the thermal image). As defined in [14], the SNR of the measured thermal data is calculated as:

$$SNR(t) = 20\log_{10}\frac{|\mu_D(t) - \mu_S(t)|}{\sigma_S(t)} \tag{5}$$

where $\mu_D(t)$ is the mean of surface temperature difference profile for the defective area, and $\mu_S(t)$and $\sigma_S(t)$ are the mean and standard deviation of the sound area, respectively. In order to be able to detect any type of defect, an *SNR* of greater than 0 dB is ideally required for successful defect detections [15].

The mean, $\mu(z,t)$, and standard deviation, $\sigma(z,t)$, of the temperature difference at time *t* for the defect and sound areas can be calculated as follows:

$$\mu(t) = \frac{1}{N_P} \sum_{P=1}^{N_P} \Delta T_P(t) \tag{6}$$

$$\sigma(t) = \sqrt{\frac{1}{N_P} \sum_{P=1}^{N_P} [\Delta T_P(t) - \mu(t)]} \tag{7}$$

where $\Delta T_p(t)$ is the temperature difference at pixel *p* and time *t*, and N_p refers to total number of pixels for a given zone (defect or sound area). In the case of a noisy environment or a low (measured) *TC* in comparison with the sensitivity of the thermal camera, signal processing methods such as a median filter can be applied to the measured thermal image to reduce the effect of noise (and improve the *SNR*).

3. ELECTROMAGNETIC-THERMAL SIMULATION

In order to investigate the sensitvity of AMT to the presence of defects in RCMs, a coupled electromagnetic-thermal simulation was performed using CST MultiPhysics Studio™. The simulation was carried out in two parts. First, the electromagnetic response was determined. The solution is based on the finite difference time domain technique. For electromagnetic source, a 50 W plane wave excitation is considered. Subsequently for thermal simulation, the computed electric fields are utilized to determine the transient heat diffusion based on Eq. (2). In the simulation, open boundary conditions were utilized in order to model an infinite expansion of the material along the lateral direction (i.e., perpendicular to the propagation direction of the incident electromagnetic energy). Thus, heat diffusion is the only mechanism of heat transfer in the lateral direction as a result of

the open boundary condition. In addition, at the top and bottom of the sample under test, heat convection is considered with the following boundary condition:

$$K_T \frac{\partial T}{\partial n} = -h_C (T - T_a) \tag{8}$$

where h_C is the convective heat transfer coefficient (W/m^{2}K), and T_a is the ambient temperature. In this case for RCM, h_C = 10 W/m^{2}K is considered. Also, the emissivity of the CFRP is considered to be 0.9, which corresponds to the ability of CFRP to emit infrared energy.

For simplicity, only simulation of the unbond defect is considered, as the coupled electromagnetic-thermal response for all three defect types will be similar (since all three defect types result in the addition of air to the structure). As such, an RCM with a 1 mm layer of unidirectional CFRP attached to the CM with a 1 mm layer of adhesive is considered (similar to Figure 1). The defect is modeled with dimensions of $w \times w$ and thickness of d between the CFRP and CM (see Table 1 for the elctromagnetic and thermal properties of the materials used in simulation). The *TC* for an unbond defect with w = 60 mm for both parallel (*Pr*) and perpendicular (*Pn*) polarizations is shown in Figure For parallel polarization, the CFRP layer is modeled as a good electrical conductor, and for perpendicular polarization, it is modeled as a lossy dielectric (see Table 1). As seen, increasing the thickness (d) of the unbond area results in an increase in *TC* since this causes a thicker air gap between the CFRP layer and CM. In addition, the *TC* for parallel polarization is less than the *TC* for perpendicular polarization. This is a result of the fact that in the latter case, the majority contribution of heat generation is due to dielectric heating as CFRP$\perp$ acts as a lossy dielectric.

In Figure 3, the effect of defect width (for a fixed d of 1 mm) is presented for perpendicular polarization. In this case, a larger area experiences a higher temperature increase, but the difference in comparison to the changing in thickness is not substantial, showing ~0.15 K temperature difference for w = 40 to 80 mm (as compared to 0.7 K for d = 1 mm to 3 mm in Figure 2).

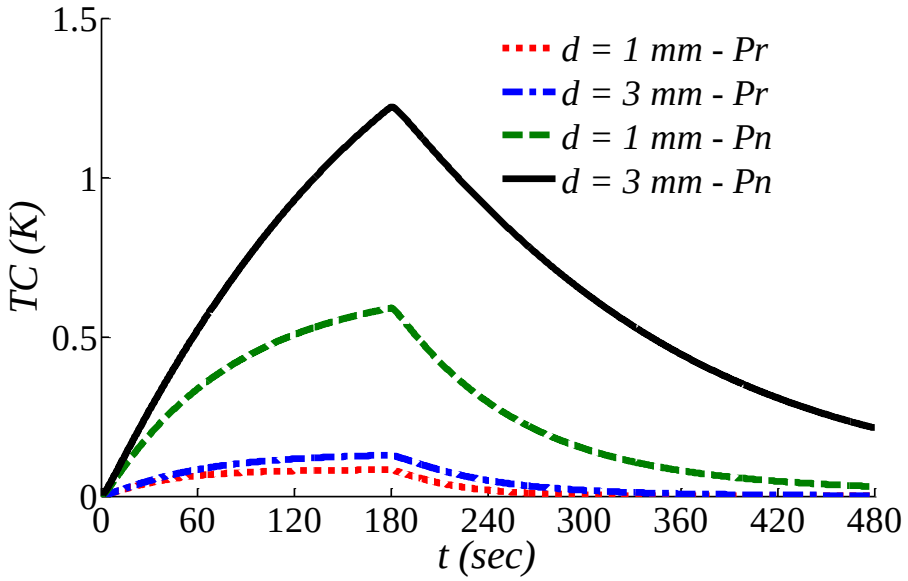

Figure 2 - Simulated *TC* for an unbond defect for parallel (*Pr*) and perpendicular (*Pn*) polarization

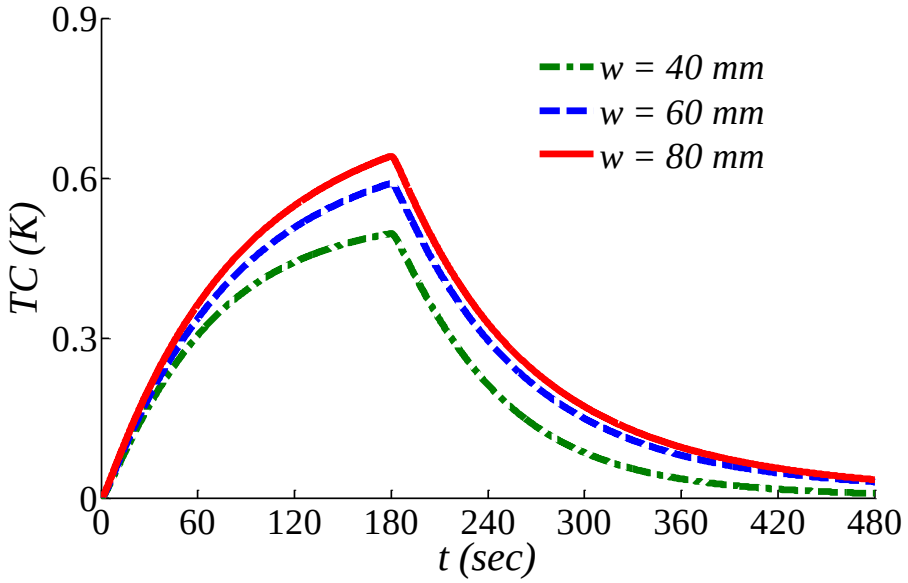

Figure 3 - Simulated *TC* for an unbond defect for perpendicular (*Pn*) polarization for various defect dimensions

4. MEASUREMENTS

4.1. SAMPLE PREPARATION

As presented in the simulated results, the presence of defects can be detected in the surface thermal profile, supporting the potential of AMT for defect detection in RCMs. To further support the results, AMT measurements were conducted on three different mortar samples, one with an unbond defect, one with multiple delaminations, and one with cracks, as shown in Figure 4. For each sample, the location of the defects (D) are indicated. The samples were made using a water-to-cement ratio (w/c) of 0.6 and sand-to-cement ratio (s/c) of 2.0, and were allowed to fully cure in ambient conditions for approximately 4 months. After curing, two layers (oriented in the same direction) of unidirectional CFRP laminate were bonded to each sample's surface by using adhesive. The unbond defect (Figure 4a, in a sample with dimensions of 52 × 38 × 9 cm^3), was made by placing a thin sheet (5 mm) of foam (with dimensions of 6 cm × 8 cm) between the CM and CFRP laminate at the center of the sample. The use of foam (emulating air) to create an unbond is reasonable since the thermal conductivity and specific heat properties of foam and air are very similar, as are the dielectric properties of foam and air (Table 1). Several delaminations (Figure 4b, in a sample with dimensions of 52 × 38 × 7.8 cm^3), were formed by injecting air between the CFRP laminate and the CM to create a thin air gap between the CFRP laminate and the adhesive during manufacture. The delaminations vary in size and geometry with a thickness ranging from 1-3 mm and an area ranging from ~10 to ~100 cm^2. At the top left corner of this sample, air was injected to create a delamination which was subsequently filled by injecting adhesive (marked as filled defect in Figure 4b). In this way, the potential for AMT to assess repaired defects is also studied. The sample with cracks (Figure 4c, dimensions of 52 × 38 × 9 cm^3) includes crack D1 (representative of the effect of an impact), and a thin cracked area (which may come from environmental causes as mentioned above), D2.

(a) (b) (c)

Figure 4 - RCM samples with (a) an unbond, (b) delaminations, and (c) cracks

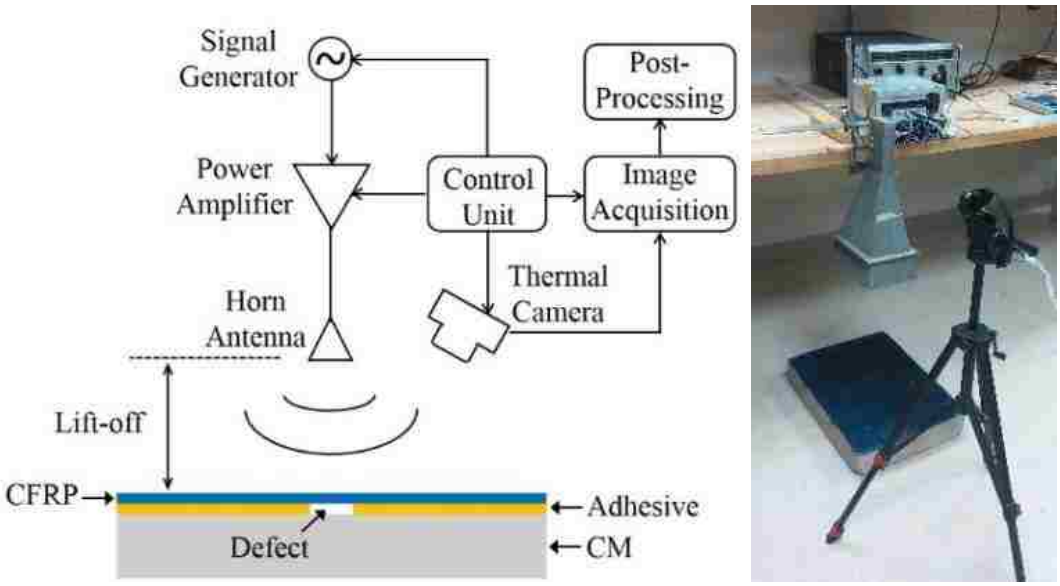

(a) (b)

Figure 5 - The AMT (a) system configuration, (b) measurement setup

4.2. AMT MEASUREMENTS AND DISCUSSION

A schematic and photograph of the AMT measurement setup is shown in Figure 5. In the system, electromagnetic energy is generated by a signal generator operating at a frequency of 2.4 GHz. Then, the power level of the signal is amplified using a 50 W power amplifier. The linearly polarized electromagnetic energy was radiated toward the RCM samples using a horn antenna, which is capable of handling high power signals as well as concentrating the energy toward the surface of the samples. The surface thermal profile is captured using a DRS Tamarisk 320 thermal camera [30]. Each measurement included 180 sec of microwave illumination (the heating period) followed by an additional 300 sec of measurement (the cooling period).

In Figure 6a, the surface thermal profile of the sample with the unbond defect is presented after 60 and 180 sec of microwave illumination with perpendicular polarization. In addition, the linear (one-dimensional) temperature profile (Figure 6b) across the central portion of the defect is also included. More specifically, the temperature increase based on Eq. (3) at distance *R* from the center point of the defect area is presented along the X- and Y-directions (as illustrated in Figure 6a). From Figure 6a, the mean temperature difference at the defect and sound area is 2.32 K, and 0.29 K, respectively. These values after 180 sec are 3.18 K and 0.87 K, respectively. This difference in temperature between defective and sound areas is due to the lower thermal conductivity of air (or foam) than adhesive (as mentioned above). From Figure 6b, the defect dimensions can be estimated to be ~8 cm along the X- and ~6 cm along the Y-direction. To quantitatively analyze the results determined from the surface thermal profile, the *TC* in Eq. (4) and *SNR* in Eq. (5) are required. As such, proper/correct determination of a sound area is necessary. From Figure 6b, it is observed that after 12 cm from the center point of the defect along both X- and Y-directions, the temperature response is essentially constant, with slight variation (due to environmental noise). Thus, an area with the distance of 12 cm from the center point of the defect area can be considered as a sound area, as is indicated in Figure 6a.

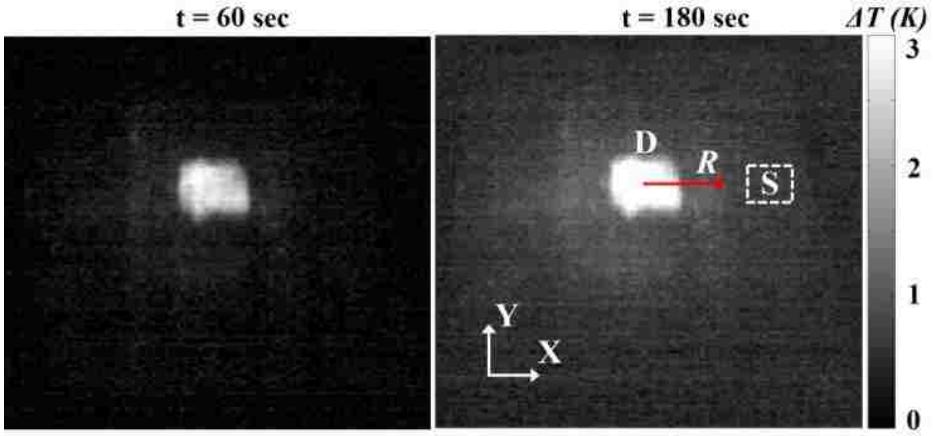

(a)

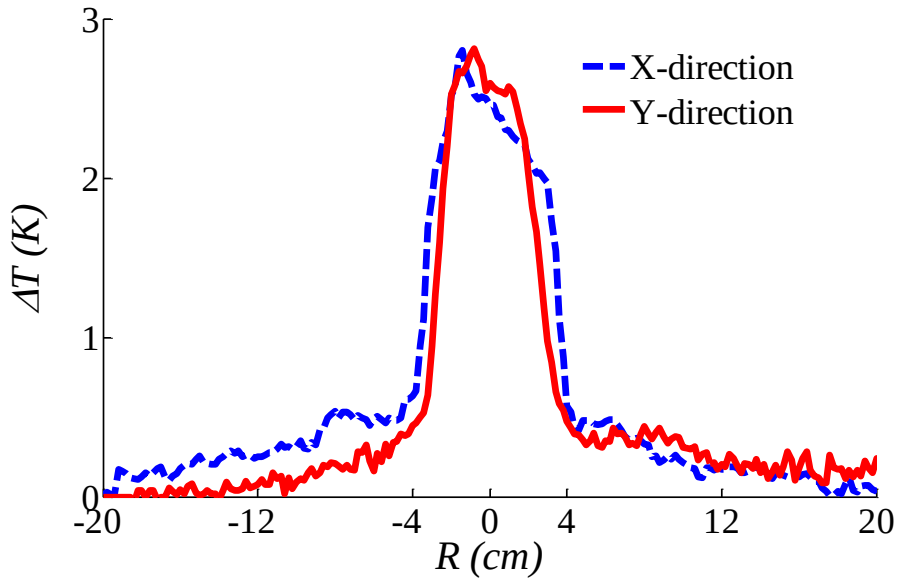

(b)

Figure 6 - Thermal profile of RCM sample with unbond defect for perpendicular polarization (a) surface temperature after 60 and 180 sec, (b) linear temperature profile after 60 sec

In Figure 7, the surface thermal profile of the measured data (unfiltered, or $n = 1$) and post-processed (by applying the median filter) data for parallel polarization after 180 sec of microwave illumination are presented. As discussed, CFRP acts as a good conductor when illuminated with parallel polarized energy. To this end, a reduction of the induced heat compared to perpendicular polarization illumination is apparent (comparing

Figure 6 and Figure 7). This indicates that the level of the signal is reduced, but the noise (independent of the orientation and related to the environment and system) remains the same. Thus, utilizing parallel polarization will cause a reduction in *SNR.*

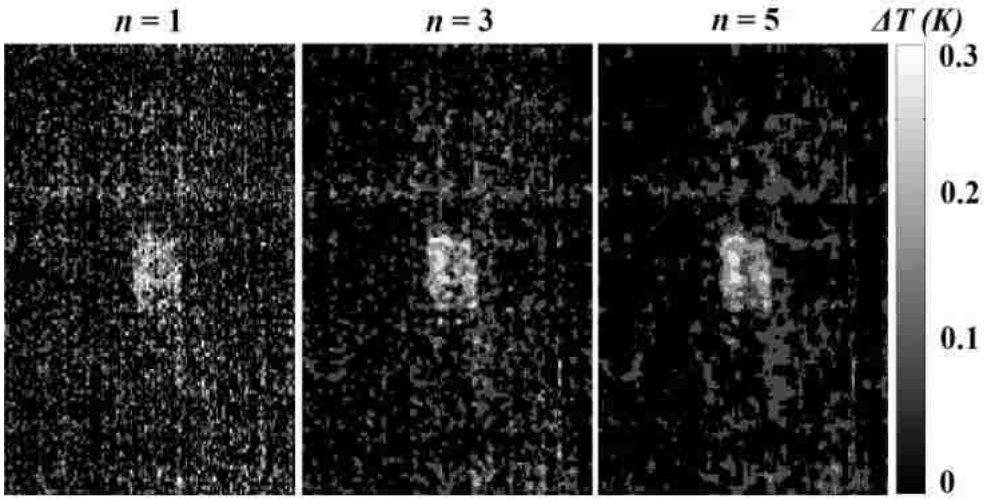

Figure 7 - Raw (n = 1) and median filtered (n = 3 and 5) surface thermal profile of the RCM with unbond after 180 sec of microwave illumination with parallel polarization

In Figure 8a and b, the (unprocessed) *TC* and *SNR* for both polarizations are presented. As shown in Figure 8a, the *TC* increases as the heating time increases (as is expected). Since CFRP is a good conductor under parallel polarization and acts as a lossy dielectric under perpendicular polarization, the defect under perpendicular illumination experiences greater *TC* than when under parallel illumination. With regards to the *SNR*, shown in Figure 8b, the change in *SNR* after ~60 sec of microwave illumination is not significant for both polarizations. This indicates that ~60 sec of illumination may be sufficient for unbond detection in RCMs. This time (~60 sec) can alter slightly by changing the material under the test.

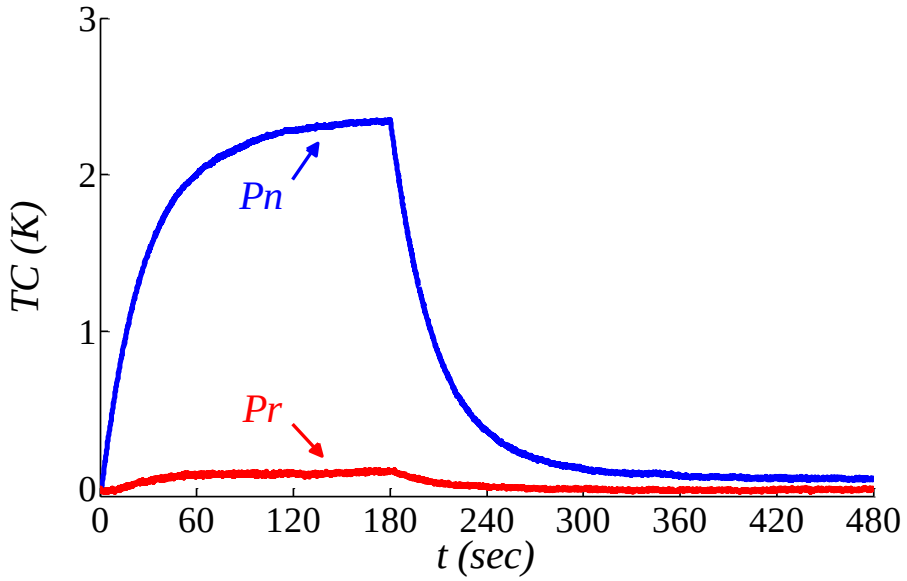

(a)

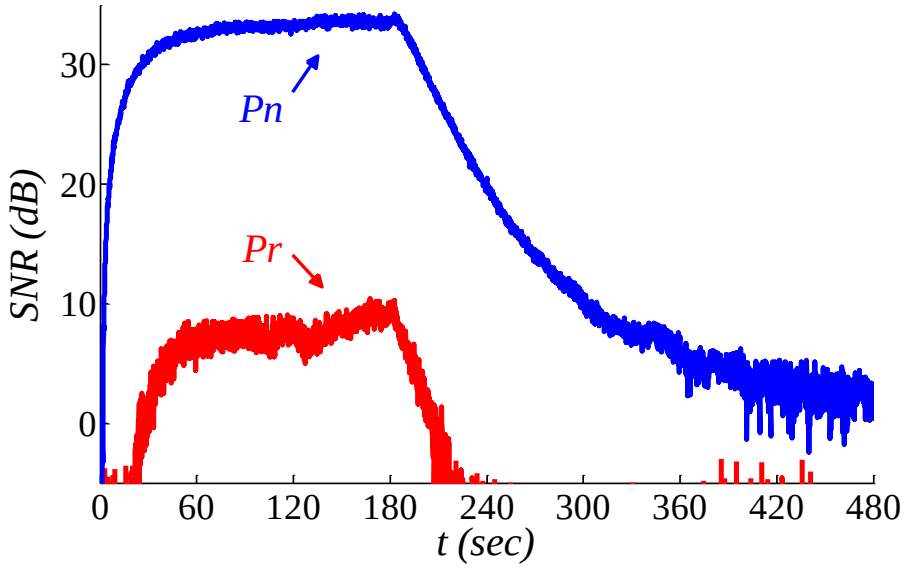

(b)

Figure 8 - (a) TC and (b) SNR, of RCM sample with unbond defect for perpendicular and parallel polarizations

In Table 2, the results of perpendicular and parallel polarization heating after 60, 120, and 180 sec are presented. The results include the mean (μ) and standard deviation (σ) for the defective and sound areas along with the *SNR* and *TC*. It is obvious that as the heating time increases, the mean value of temperature difference at the defected and sound area increases. Also, the standard deviation of sound area remains constant, indicating the presence of environmental noise.

Table 2 - Thermal response of RCM with perpendicular and parallel polarization illumination

Parameters		**Perpendicular polarization**			**Parallel polarization**		
		t = 60	t = 120	t = 180	t = 60	t = 120	t = 180
ΔT_D *(t)*	μ	2.31	2.83	3.17	0.105	0.110	0.120
ΔT_S *(t)*	μ	0.17	0.48	0.72	0.005	0.005	0.010
	σ	0.097	0.084	0.089	0.080	0.083	0.083
TC (°K)		2.14	2.35	2.45	0.100	0.105	0.110
SNR (dB)		26.9	28.8	28.8	1.94	2.04	2.45

Since parallel polarization has been shown to be inferior, only perpendicularly polarized illumination was used for the other samples. As seen in Figure 9, the surface thermal profile of the delamination sample is presented after 60 and 180 sec of (perpendicularly polarized) microwave illumination. This sample contains 6 delaminations (D) along with sound area (S). As is evident, the temperature difference at the delamination locations after 60 sec of microwave illumination varies from 0.8-2 K and the sound areas have a temperature difference of < 0.5 K. In addition, delaminations

D4 and D6 show the highest and lowest temperature increase, respectively (due to the defect size difference of ~10 and 100 cm^2 and thickness difference of ~1-3 mm, respectively). As it is obvious, the filled defect is not showing any temperature change, indicating repaired defect. The *TC* and SNR for this sample under perpendicular polarization are presented in Figure 10a and b. As expected, based on the delamination size and thickness, D4 and D6 experience the largest and smallest *TC*, shown in Figure 10a. Further, even for the smallest delamination, D6, an *SNR* of 14.1 dB is achieved, shown in Figure 10b. Moreover, the change in *SNR* after ~60 sec for all delaminations is not significant, similar to the unbond defect, indicating that ~60 sec of microwave illumination may be sufficient for delamination detection in RCMs. As mentioned previously, this value depends on the thermal properties of the CFRP and may change for different materials and structures.

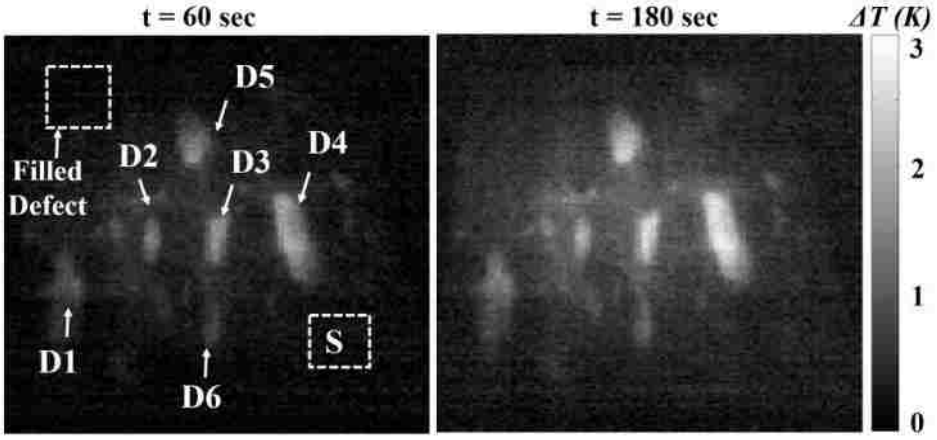

Figure 9 - Surface thermal profile of RCM sample with delaminated defects for perpendicular polarization

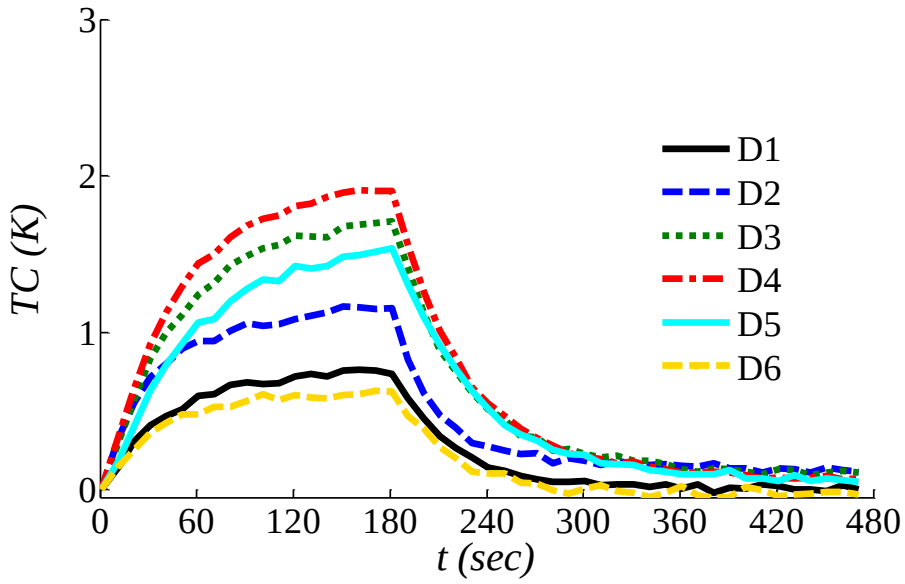

(a)

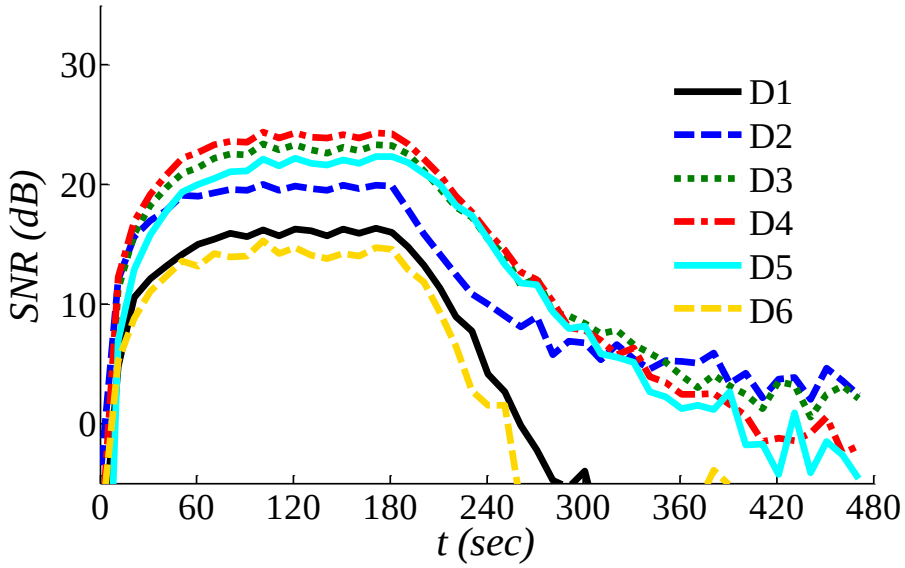

(b)

Figure 10 - (a) TC and (b) SNR, of RCM sample with delaminated defects for perpendicular polarization

In Figure 11, the surface thermal profile of the RCM with cracks D1 (i.e., recess or indentation on the surface) and D2 (i.e., notch on the surface) is presented after 60 and 180 sec of heating time. The temperature at D1 and D2 provide an indication of the difference between these two cracks. More specifically, since D1 contains more thermally insulating material (air), a greater temperature increase (2.5 K) as compared to the shallow and narrow crack D2 (1.5 K) after 60 sec of microwave illumination is detected. In addition, the sound areas experience temperature increase of < 0.5 K after 60 sec of heating. In Figure 12, the *TC* and *SNR* for this sample under perpendicular polarization are presented. From the results in Figure 12a, D1 experiences greater *TC* than D2 (as expected). In Figure 12b, for the even for the narrow and shallow crack, D2, an *SNR* of 22.2 dB is achieved after 60 sec of microwave illumination. Also, an *SNR* of 27.5 dB after 60 sec heating for D1 is attained.

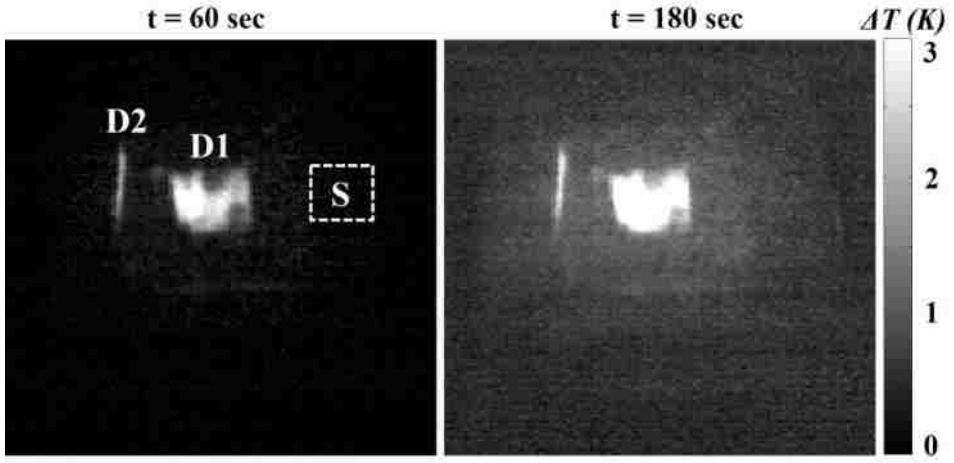

Figure 11 Surface thermal profile of RCM sample with crack defects for perpendicular polarization

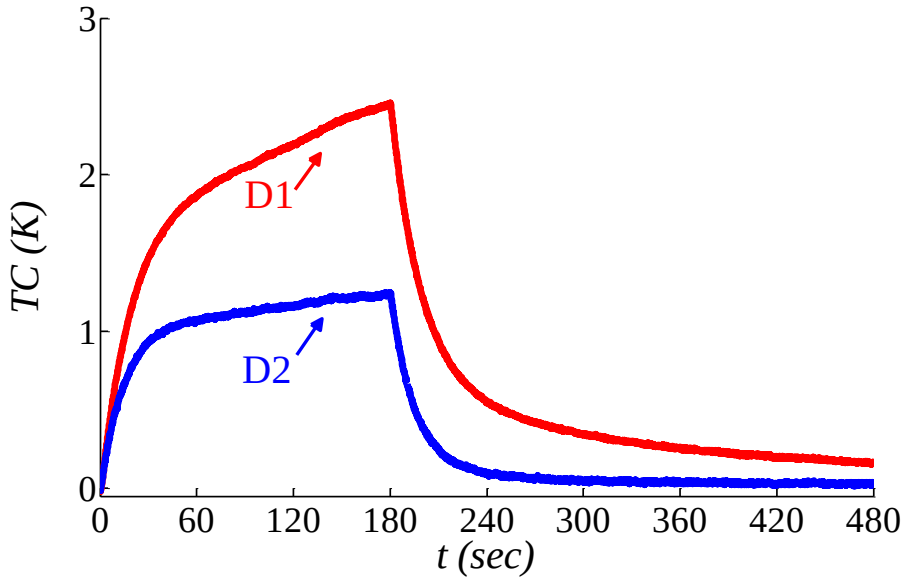

(a)

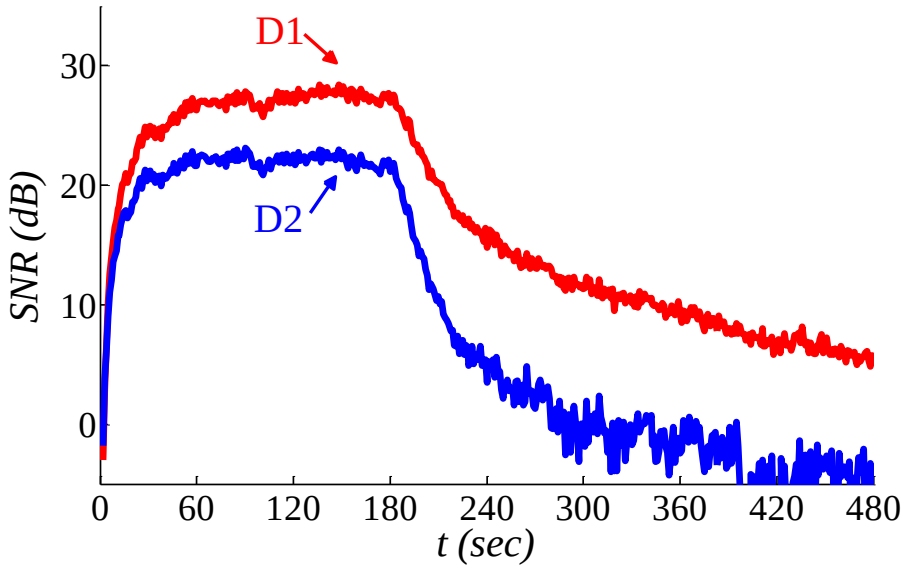

(b)

Figure 12 - (a) TC and (b) SNR, of RCM sample with crack defects for perpendicular polarization

5. CONCLUSION

Nondestructive testing of rehabilitated cement-based materials with carbon fiber reinforced polymer composites is quite important in the transportation industry. Among various nondestructive testing techniques, Active Microwave Thermography, based on the integration of microwave and thermographic NDT, has also been considered as a potential NDT tool for infrastructure. As such, to assess the potential of AMT for inspection of RCMs, simulations and measurements of RCM samples with various types of defects are performed. Simulations shown that since the CFRP is conductive when illuminated with microwave energy polarized parallel to the CFRP fiber direction but behaves as a lossy dielectric when illuminated by energy polarized perpendicular to the fiber direction, the temperature contrast (*TC*) between healthy and defective areas is much greater for the latter case. Additionally, increasing defect dimensions also led to a greater *TC*. Representative measurements on samples with three common types of defects (unbond, delamination, and crack) were conducted using AMT. Since the presence of noise is inevitable in practice, a quantitative analysis of the measured results based on the signal-to-noise ratio (*SNR*) for all three defect types is presented. From this analysis, it is shown that the *SNR* does not improve significantly after ~60 sec of microwave illumination, indicating a potentially maximum effective heat time for inspection of RCMs. This time may differ for other materials under test, as it is related to the thermal properties of the materials. Also, utilizing a microwave excitation polarized perpendicular to the fiber direction results in an *SNR* of 26.9 dB as compared to 1.94 dB for a parallel polarized excitation for unbond defect detection. Furthermore, it is shown that applying a median filter to the measured thermal results improves the *SNR* by ~3 dB. This is important for cases where a parallel polarized excitation cannot be avoided, such as bidirectional CFRP. Overall, the results presented here indicate that AMT has strong potential for inspection of RCMs. As AMT is still under development, authors are investigating a number of potential future improvements to AMT in general and for *SNR* specifically including the implementation of lock-in techniques and/or a modulated excitation approach.

REFERENCES

[1] M. Fakharifar, G. Chen, L. Sneed, and A. Dalvand, "Seismic performance of post-mainshock FRP/steel repaired RC bridge columns subjected to aftershocks" Composites Part B: Engineering, vol. 72, pp. 183-198, 2015.

[2] A. Ebrahimkhanlou, A. Farhidzadeh, and S. Salamone, "Multifractal analysis of crack patterns in reinforced concrete shear walls," Structural Health Monitoring, pp. 1475921715624502, 2016.

[3] R. Zoughi, "Microwave non-destructive testing and evaluation principles" vol. 4, Springer Science & Business Media, 2000.

[4] M. Fallahpour, and R. Zoughi, "Fast 3-D qualitative method for through-wall imaging and structural health monitoring," IEEE Geoscience and Remote Sensing Letters, vol. 12, no. 12, pp. 2463-2467, 2015.

[5] B. Akuthota, B., D. Hughes, R. Zoughi, J. Myers, and A. Nanni, "Near-field microwave detection of disbond in carbon fiber reinforced polymer composites used for strengthening cement-based structures and disbond repair verification," Journal of materials in civil engineering, vol. 16, no. 6, pp. 540-546, 2004.

[6] S. Kharkovsky, A. C. Ryley, V. Stephen, and R. Zoughi, "Dual-polarized near-field microwave reflectometer for noninvasive inspection of carbon fiber reinforced polymer-strengthened structures," IEEE Transactions on Instrumentation and Measurement, vol. 57, no. 1, pp. 168-175, 2008.

[7] M. Ricci, L. Senni, and P. Burrascano, "Exploiting pseudorandom sequences to enhance noise immunity for air-coupled ultrasonic nondestructive testing," IEEE Transactions on Instrumentation and Measurement, vol. 61, no. 11, pp. 2905-2915, 2012.

[8] S. C. de Wolski, J. E. Bolander, and E. N. Landis, "An in-situ X-ray microtomography study of split cylinder fracture in cement-based materials," Experimental Mechanics, vol. 54, no. 7, pp. 1227-1235, 2014.

[9] Y. Y. Hung, Y. S. Chen, S. P. Ng, L. Liu, Y. H. Huang, B. L. Luk, R. W. L. Ip, C. M. L. Wu, and P. S. Chung, "Review and comparison of shearography and active thermography for nondestructive evaluation," Materials Science and Engineering: R: Reports, vol. 64, no. 5, pp. 73-112, 2009.

[10] A. Poudel, K. R. Mitchell, T. P. Chu, S. Neidigk, and C. Jacques, "Non-destructive evaluation of composite repairs by using infrared thermography," Journal of Composite Materials, vol. 50, no. 3, pp. 351-363, 2016.

[11] R. Yang, and Y He, "Optically and Non-optically Excited Thermography for Composites: A Review," Infrared Physics & Technology, vol. 75, pp. 26-50, 2016.

[12] Z. Li, and Z. Meng, "A Review of the Radio Frequency Non-destructive Testing for Carbon-fibre Composites," Measurement Science Review, vol. 16, no. 2, pp. 68-76, 2016.

[13] C. Ibarra-Castanedo, and X. Maldague, "Infrared thermography," Chapter 10, In Handbook of Technical Diagnostics, pp. 175-220. Springer Berlin Heidelberg, 2013.

[14] C. Ibarra-Castanedo, J. Piau, S. Guilbert, N. P. Avdelidis, M. Genest, A. Bendada, and X. Maldague, "Comparative study of active thermography techniques for the nondestructive evaluation of honeycomb structures," Research in Nondestructive Evaluation, vol. 20, no. 1, pp. 1-31, 2009.

[15] K. Srinivas, A. O. Siddiqui, and J. Lahiri, "Thermographic inspection of composite materials," In Proc. National Seminar on Non-Destructive Evaluation, vol. 12, pp. 7-9, 2006.

[16] V. Arora, J. Siddiqui, R. Mulaveesala, and A. Muniyappa, "Pulse compression approach to nonstationary infrared thermal wave imaging for nondestructive testing of carbon fiber reinforced polymers," IEEE Sensors Journal, vol. 15, no. 2, pp. 663-664, 2015.

[17] R. Mulaveesala, V.S. Ghali, and V. Arora, "Applications of non-stationary thermal wave imaging methods for characterisation of fibre-reinforced plastic materials," Electronics Letters, vol. 49 no. 2, pp. 118-119, 2013.

[18] J. G. Thompson, and C. T. Uyehara, "Ultrasonic thermography inspection method and apparatus," U.S. Patent 7,075,084, 2006.

[19] D. Vasic, V. Bilas, and D. Ambrus, "Pulsed eddy-current nondestructive testing of ferromagnetic tubes," IEEE Transactions on Instrumentation and Measurement, vol. 53, no. 4, pp. 1289-1294, 2004.

[20] J. Saniie, M. Luukkala, A. Lehto, and R. Rajala, "Thermal wave imaging through radio frequency induction heating," Electronics Letters, vol. 18, no. 15, pp. 651-653, 1982.

[21] D. Balageas, and P. Levesque, "Mines detection using the EMIR® method," In QIRT, pp. 71-78, 2002.

[22] C. A. DiMarzio, C. M. Rappaport, W. Li, M. E. Kilmer, and G. O. Sauermann, "Microwave-enhanced infrared thermography," In International Society for Optics and Photonics, Photonics East (ISAM, VVDC, IEMB), pp. 337-342, 1999.

[23] S. Keo, D. Defer, F. Breaban, and F. Brachelet, "Comparison between microwave infrared thermography and CO2 Laser infrared thermography in defect detection in applications with CFRP," Materials Sciences and Applications, vol. 4, pp. 600-605, 2013.

[24] A. Foudazi, I. Mehdipour, K. M. Donnell, and K. H. Khayat, "Detection of steel fibers in cement-based materials by active microwave thermography," In 14th International Symposium on Nondestructive Characterization of Materials (NDCM2015), pp. 22-26, 2015.

[25] A. Foudazi, I. Mehdipour, K. M. Donnell, and K. H. Khayat, "Evaluation of steel fiber distribution in cement-based mortars using active microwave thermography," Materials and Structures, 2016, DOI: 10.1617/s11527-016-0843-3.

[26] A. Foudazi, M. T. Ghasr, and K. M. Donnell, "Characterization of corroded reinforced steel bars by active microwave thermography," IEEE Transactions on Instrumentation and Measurement, vol. 64, no. 9, pp. 2583-2585, 2015.

[27] A. Foudazi, M. T. Ghasr, and K. M. Donnell, "Application of active microwave thermography to inspection of carbon fiber reinforced composites," In 2014IEEE AUTOTESTCON, pp. 318-322, 2014.

[28] A. Foudazi, K. M. Donnell, and M. T. Ghasr, "Application of active microwave thermography to delamination detection," In Proceedings 2014 IEEE International Instrumentation and Measurement Technology Conference (I2MTC), pp. 1567-1571, 2014.

[29] CST - Computer Simulation Technology, http://www.cst.com.

[30] DRS Thermal Camera, http://www.drsinfrared.com.

II. ACTIVE MICROWAVE THERMOGRAPHY FOR NONDESTRUCTIVE EVALUATION OF FRP-REHABILITATED CEMENT-BASED STRUCTURES

ABSTRACT

Fiber reinforced polymer (FRP) composite materials have become important and widely accepted for rehabilitation of deteriorating concrete structures. Among numerous nondestructive testing and evaluation (NDT&E) techniques for FRP-rehabilitated cement-based structures, Active Microwave Thermography (AMT) is an integrated technique that utilizes a microwave-based heat excitation and subsequent thermal monitoring. AMT has shown promise as an NDT&E technique for the infrastructure and aerospace industries. In this paper, representative simulated and measured results for an AMT inspection of a cement-based material rehabilitated with carbon fiber reinforced polymer (CFRP) composites are presented. Specifically, the thermal contrast (*TC*) and signal-to-noise ratio (*SNR*) are provided and discussed as a function of fiber orientation, frequency, and power level. It has been shown that in the case of uni-directional fibers, when the polarization of the incident electromagnetic energy is perpendicular to the fiber direction, a shorter illumination time is required for defect detection as compared to when the incident energy is polarized parallel to the fiber direction. In addition, the saturation time is independent of polarization, so perpendicular polarization is preferred for inspection of uni-directional FRP-rehabilitated cement-based structures.

Index Terms—active microwave thermography (AMT); carbon fiber reinforced polymer (CFRP); defect detection; nondestructive testing and evaluation (NDT&E); rehabilitated cement-based materials.

1. INTRODUCTION

Fiber reinforced polymer (FRP) composite materials have become important and widely accepted for rehabilitation of deteriorating concrete structures due to their chemical stability, high mechanical strength, and low density. These composites (often in the form of laminate sheets) are applied to beams/slabs or wrapped around columns in order to enhance the structure's mechanical performance. The FRP laminates can be uni-directional, bi-directional, or layered with various angle orientations when applied to a structural element. Defects may also occur in such structures due to poor workmanship, chemical/physical degradation of the adhesive bonding layer, impact damage, or other environmental causes such as chloride ingress [1]. One type of defect that is considered and analyzed in this paper, referred to as unbond defect, occurs when the FRP is not properly bonded to the structure. As such, nondestructive testing and evaluation (NDT&E) of FRP materials utilized in the transportation and aerospace industries has become quite important.

There are different NDT&E techniques used for structural assessment including electromagnetic (e.g., microwave, eddy current, induction), mechanical (e.g., ultrasonic), thermal, etc. with varying levels of success. The microwave technique has been successfully applied for (volumetric) inspection of dielectric materials [1]-[10] but is limited to surface inspections of conductive (metal or carbon-based) structures [11]. Ultrasonic methods are well-established but often require contact with the structure under test and an expert operator [12]-[14]. Thermography has also been widely applied in the infrastructure and transportation industries. Thermographic inspections either utilize a passive (meaning solar energy) or active (meaning heat is externally applied) heat excitation with a subsequent surface temperature measurement via an infrared (IR) or thermal camera. The passive method is qualitative and limited in application [15]. For an active thermographic inspection, an external heat source such as a heat lamp [16]-[21] or other excitation (including eddy current [22]-[24], ultrasonic [25], and microwave [26]-[27]) is utilized. In eddy current (or induction) thermography, a high magnitude current is employed to induce an eddy current in a conductive material under inspection in order to produce a surface heat distribution from Joule heating and the heat diffusion process. Eddy current thermography is limited to the inspection of electrically conductive

materials. In ultrasonic thermography, ultrasonic energy is transformed into heat through friction where defects are present, meaning defects act as internal heat sources while undamaged areas show almost no temperature increase. However, ultrasonic thermography is a contact-based method, as the transducer needs to be in contact with the material under the test in order to couple the mechanical energy into the material.

In the last decade, researchers have shown an increased interest in microwave heating techniques as an alternative heat excitation for thermographic structural assessment [26]-[35]. Active Microwave Thermography (AMT) has been utilized for detection and evaluation of steel fibers in cement-based materials [30]-[31], characterization of corrosion on metal-based materials (e.g., steel) [32], inspection of aluminum structures rehabilitated with FRP [33], and preliminarily studied for defect detection in rehabilitated cement-based materials [34]-[35]. Unlike with ultrasonic thermography, insulating (dielectric) materials can be easily penetrated by microwave signals without suffering from high attenuation to reach subsurface of areas of interest (i.e., defects). In addition, unlike eddy current thermography, a microwave-based heat excitation can be utilized with both conductive and dielectric materials, since the (microwave-based) heat generation can be achieved for dielectric and conductive materials.

This paper presents the simulation and measurement results of an investigation aimed at studying the potential of AMT for detection of unbond defects in a multi-layer FRP-rehabilitated cement-based structure. Specifically, the thermal contrast (*TC*) and signal-to-noise ratio (*SNR*) are provided and discussed as a function of fiber orientation, frequency, and power level.

2. ACTIVE MICROWAVE THERMOGRAPHY

As mentioned above, AMT is capable of generating heat differently, depending on the material under inspection. More specifically, in dielectric materials, dielectric heating occurs which is related to the absorption of the microwave energy by the material. Conversely, in conductive materials, induction heating takes place, which is due

to the surface currents that are generated on the conductive material when under microwave illumination.

Dielectric materials can be described by their complex dielectric properties, and when referenced to free-space, are expressed as:

$$\varepsilon_r = \varepsilon_r' - j\varepsilon_r'' \tag{1}$$

where ε_r' and ε_r'' are the relative permittivity (representing the ability of a material to store energy) and loss factor (representing the ability of a material to absorb energy), respectively. To illustrate the process of dielectric heating, a plane wave excitation is considered. Generally speaking, a plane wave consists of orthogonally polarized electric (*E*) and magnetic (*H*) fields propagating normally to the direction of the plane of incidence (that includes both fields). Here, it is assumed that the electric field (*E-field*) is polarized in the *x*-direction with an amplitude of E_0, the magnetic field (*H-field*) is polarized in the *y*-direction with an amplitude of H_0, and both are propagating in the *z*-direction with a propagation constant of K_Z. This scenario is illustrated in Figure 1 for an infinite half-space material with the air-interface located at $z = 0$.

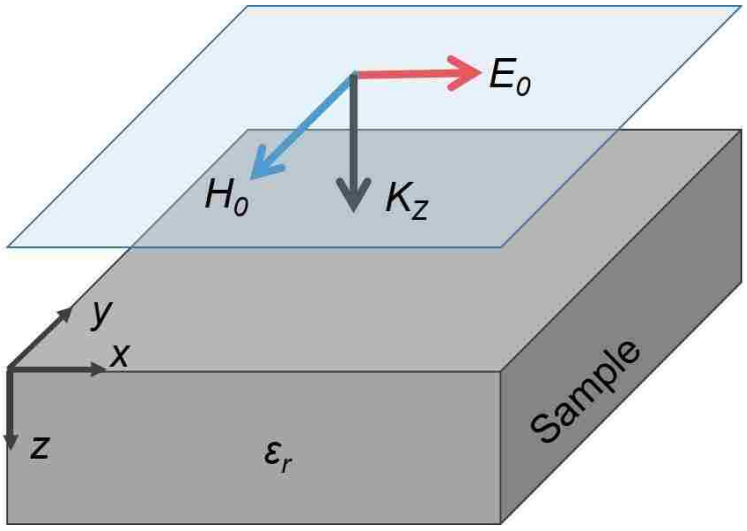

Figure 1 - Illustration of plane wave excitation for microwave-induced heating

Thus, the (frequency domain) fields at a specific location can be expressed as:

$$\vec{E} = \hat{x}E_0 \exp(-\alpha z)\exp(-jK_Z z) \tag{2}$$

$$\vec{H} = \hat{y}\frac{E_0}{\eta}\exp(-\alpha z)\exp(-jK_Z z) \tag{3}$$

where α is the attenuation constant, and η is the wave impedance and is equal to:

$$\eta = \sqrt{\mu/\varepsilon} \tag{4}$$

where μ is the permeability of the material, and $\varepsilon = \varepsilon_0 \varepsilon_r$ in which ε_0 is the permittivity of free space. To determine the complex microwave power associated with a propagating wave, the pointing vector ($\vec{S}$) inside the dielectric material with attenuation constant of α is defined as follows:

$$\vec{S} = \vec{E} \times \vec{H}^* = \frac{(\sqrt{\varepsilon})^*}{\sqrt{\mu}} E_0{}^2 \exp(-2\alpha z) \tag{5}$$

Thus, the dissipated (absorbed) power, Q, can be determined as:

$$Q = -\mathrm{Re}(\nabla.\vec{S}) = \omega\varepsilon_0\varepsilon_r'' E_0{}^2 \exp(-2\alpha z) \tag{6}$$

Here, E_0 (the electric field amplitude) is related to the microwave power source, the distance between the microwave source and sample interface (referred to as lift-off distance), and the transmission coefficient from the air to the material under the test (quantifying the amount of energy that is coupled into the material). It is important to note that E_0 and subsequently the transmitted power attenuate as the energy propagates through the material. Therefore, when a lossy dielectric is irradiated with electromagnetic energy, dielectric heating occurs as a result of the absorbed power. For dielectric

materials, this volumetric heating (i.e., increase in temperature, T) is proportional to the amount of dissipated power Q (W/m^3), thermal conductivity k (W/m.K), specific heat C (J/g.K), material density ρ (Kg/m^3), and time t (sec), and can be expressed as:

$$\rho C \frac{\partial T}{\partial t} = \nabla.(k \nabla T) + Q \tag{7}$$

From Eq. (7), the temperature increase (T) at a given (heating) time, t, as a result of the absorbed power without considering heat diffusion can be simplified as follows:

$$T \approx \frac{Qt}{\rho C} = \frac{\omega \varepsilon_0 \varepsilon_r'' \left| E_0 \right|^2 t}{\rho C} \tag{8}$$

The second heating mechanism occurs when an electromagnetic wave impinges on a conductive material. In this case, the electromagnetic energy cannot penetrate through the material. However, surface currents are induced on the surface of the conductor. Such surface currents serve as a source of radiated (or scattered) electromagnetic energy, which, in turn, may be absorbed by nearby dielectric materials (resulting in additional heat generation) [31]. Furthermore, due to the finite electric conductivity of the conductive material, ohmic (power) losses occur, also resulting in an increase in temperature of the material. Considering the Lorentz force equation and Newton's equation of motion, the ohmic loss per unit volume due to induced surface currents (J) for materials with finite conductivity can be expressed as [36]:

$$\frac{\partial P_{loss}}{\partial V} = J.E \tag{9}$$

3. ELECTROMAGNETIC-THERMAL MODELING

In order to investigate the utility of AMT for structural assessment applications, a coupled electromagnetic-thermal model was developed using CST MultiPhysics

Studio™. This model considered a thick (with 20 cm thickness) cement-based material (CM) with dimensions of 50 × 50 cm rehabilitated with a laminated carbon FRP (CFRP) composite. The CFRP layer (with 1 mm thickness) is assumed to be uni-directional. Between the CFRP and CM layers, a thin layer (1 mm) of adhesive is assumed. An unbond with dimensions of 10× 10 cm with the same thickness of the adhesive layer (1 mm) is also assumed to exist within the structure. The electromagnetic and thermal properties for the CM and CFRP are defined in Table 1. Among these materials, uni-directional CFRP is unique in that it can totally reflect or partially transmit electromagnetic waves, depending on the polarization of the impinging electric field. In other words, when carbon fibers are made into laminate sheets, their interaction with electromagnetic energy is strongly influenced by the relative orientation of the fibers with respect to the polarization of the incident signal. More specifically, electromagnetic energy can penetrate through CFRP sheets when the polarization of the electric field is perpendicular to the fiber orientation ($\perp$). Therefore, $\perp$ CFRP is considered a lossy dielectric with $\varepsilon_r \approx 7 - j2.5$. For the case when the fibers are parallel to the incident electric field polarization ($\|$), CFRP behaves as good conductor with electric conductivity of $\sigma \approx 10^4$S/m.

Table 1 – Electromagnetic-thermal properties of materials

Material	**Electromagnetic Properties**	**Thermal Properties**	
		***k*(W/m.K)**	***C*(J/g.K)**
Air	$\varepsilon_r = 1$	0.026	1.005
Foam	$\varepsilon_r \approx 1$	0.03	1.3
Adhesive	$\varepsilon_r \approx 6\text{-}j0.6$	1.0	3.7
CM	$\varepsilon_r \approx 4.7\text{-}j0.7$	1.7	0.8
CFRP $\|\|$	$\sigma = 10^4$	7	1.2
CFRP$\perp$	$\varepsilon_r \approx 7\text{-}j2.5$	0.8	1.2

The electromagnetic and thermal boundary conditions used in the model are defined in Figure 2a and Figure 2b, respectively. To create a plane wave excitation, perfect electric conductors (PEC) at the *yz*-plane and perfect magnetic conductors (PMC) at the *xz*-plane are considered, meaning uniform or orthogonal *E*- and *H-fields* with a constant phase plane (front). Thermally, adiabatic boundaries were defined at the *xz*- and *yz*-planes, as is illustrated in Figure 2b. The sample has infinite half-space thickness in the *z*-direction.

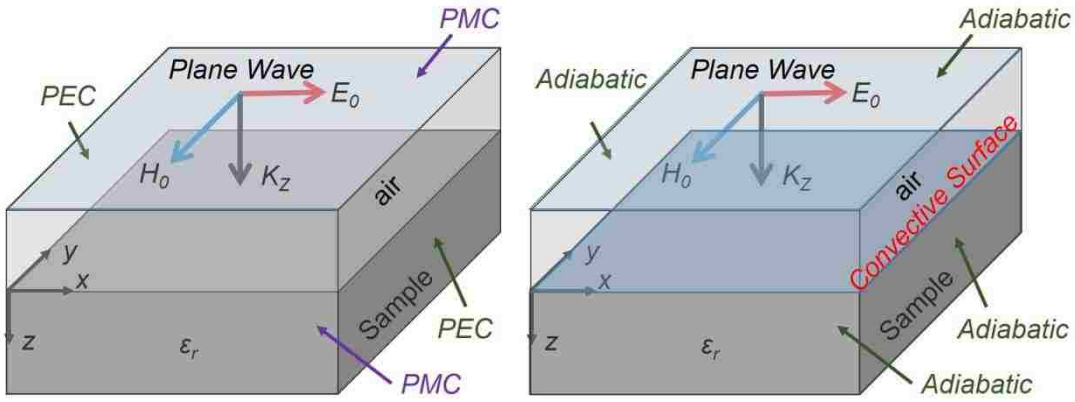

(a) (b)

Figure 2 - Simulation model including boundary conditions for (a) electromagnetic and (b) thermal simulations

Unless indicated otherwise, all simulations assume the electromagnetic (plane wave) excitation to have a power of 50 W and a frequency of 2.45 GHz. From this excitation, the *E*- and *H-fields* and induced surface currents were determined and subsequently utilized to find the temperature distribution on the surface of the sample during and after microwave illumination. Additionally, in order to incorporate heat convection at the sample-air boundary (i.e., CFRP-air), the convective surface at the *xy*-plane (top of the sample) has to be applied:

$$k\frac{\partial T}{\partial n} = -h(T - T_a) \tag{10}$$

where h is the convective heat transfer coefficient (W/m^{2}K), and T_a is the ambient temperature. For this case, the heat transfer coefficient is defined as h = 10 W/m^{2}K.

In Figure 3, each layer of a strengthened-CM utilizing a single CFRP layer and adhesive for $\perp$ and || CFRP orientations is illustrated. Specifically, Figure 3a shows the case when the polarization of the incident electric field is parallel to the fiber orientation (Pr-Pol), and Figure 3b illustrates the case when the electric field polarization is perpendicular to the fiber orientation (Pn-Pol).

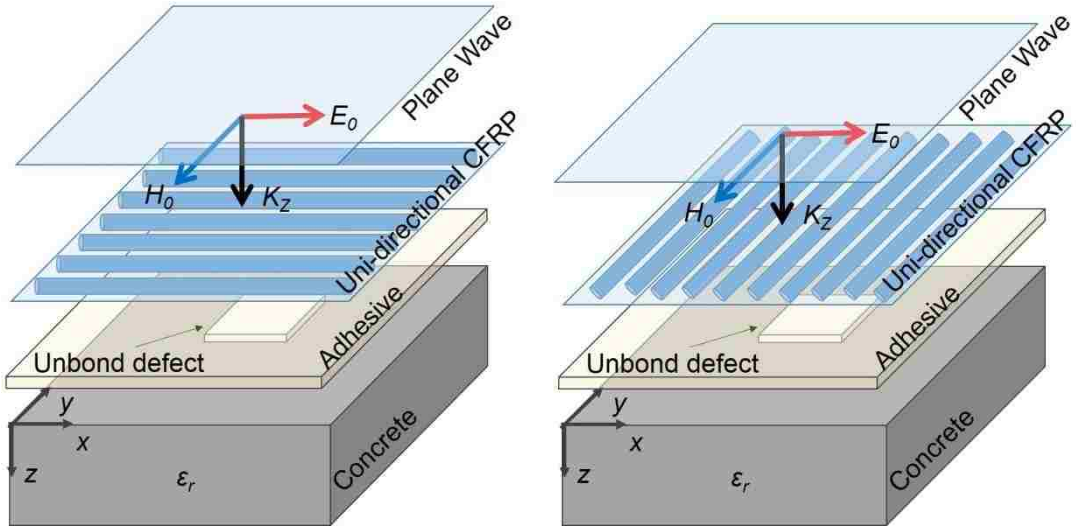

(a) (b)

Figure 3 - Fiber direction parallel (a) and perpendicular (b) to the electric field polarization

In order to quantitatively analyze the thermal response of the material under test during an AMT inspection, thermal contrast (TC) is defined. Prior to microwave illumination, the temperature of the structure is equal to the ambient temperature, T_a. After microwave illumination, the temperature increase, $\Delta T(t)$, at each location can be expressed as the difference between the absolute temperature, $T(t)$, at time t and T_a and is expressed as follows:

$$\Delta T(t) = T(t) - T_a \tag{11}$$

Then, the *TC* can be expressed as the difference between the temperature increase of a defective area (T_D) and a sound (defect-free) area (T_S) as follows:

$$TC = \Delta T_D(t) - \Delta T_S(t) \tag{12}$$

Practically speaking, the *TC* must be greater than the sensitivity of the thermal camera to detect the presence of a defect after a heating time of *t*. In Figure 4, the simulated *TC* is shown for the two different fiber orientations of Figure 3. For the case of parallel polarization (Pr-Pol), the main heating mechanism is induction heating while for the perpendicular case (Pn-Pol), the structure experiences dielectric heating. As shown, the *TC* and subsequently the amount of heat generated in Pr-Pol is much less than that of the case of Pn-Pol, indicating that the effect of dielectric heating is more significant than that of induction heating.

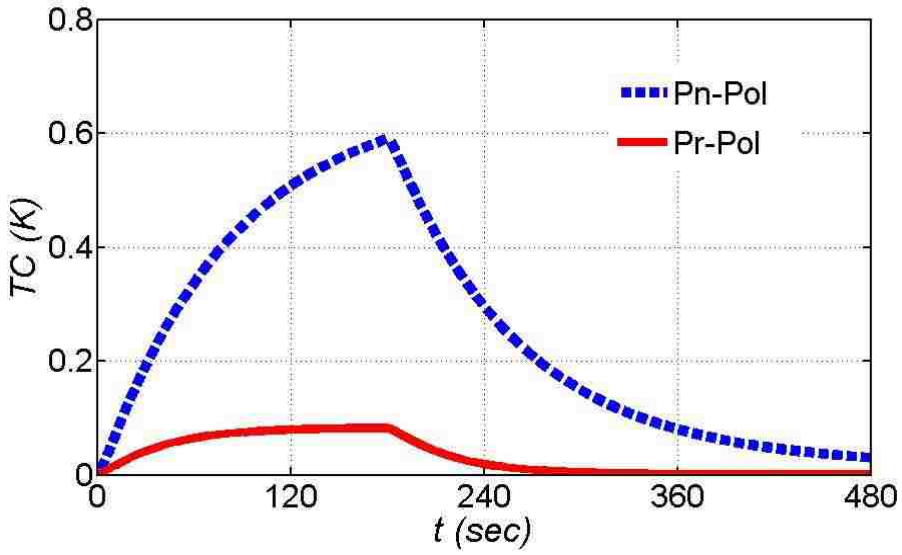

Figure 4 - Simulated *TC* for an unbond for parallel and perpendicular (to the fiber direction) polarizations

Next, simulations were conducted to investigate the effect of additional CFRP layers (as the results above only considered a single layer). In other words, the sample of Figure 3 was considered but with an additional CFRP layer (adhesive and CFRP layer

thickness both are 1 mm). In this case, since there are now two interfaces related to the presence of the rehabiliation material (two layers of CFRP), an unbond defect can exist at the CFRP-CFRP interface (referred to as D1), or at the CFRP-CM interface (referred to as D2). In both cases, the unbond defect is modeled as lack of adhesive between layers (as above). With respect to the orientation of the *E-field* polarization and fiber direction of the CFRP layers, eight situations can occur (depending on *E-field* polarization, fiber orientation, and defect location), as given in Table 2. Table 2 also includes the *TC* after 180 sec of microwave illumination.

Table 2 - *TC* (K) for an unbond in a rehabilitated CM with two layers of CFRP. The CM is assumed to be flush with the 2nd layer indicated below

Case	Fiber Orientation (with respect to *E-field* Polarization)	*TC*(K)	
		D1	D2
I	CFRP ⊥ - CFRP ⊥	1.42	0.98
II	CFRP ⊥ - CFRP ∥	0.13	0.12
III	CFRP ∥ - CFRP ⊥	0.12	0.08
IV	CFRP ∥ - CFRP ∥	0.12	0.06

As seen, for all cases, the defect farther from the surface (listed as D2 in Table 2) will experience a lower *TC* than the defect closer to the surface (listed first in Table 2, D1). In addition, the highest *TC* is observed for case *I* (i.e., dielectric heating mechanism only). Conversely, the lowest *TC* is obtained for case *IV* (i.e., induction heating mechanism only). Thus, it is important to ensure that the *E-field* is perpendicularly polarized with respect to the fiber orientation (for two layers of CFRP with the same orientation) to attain the maximum *TC*. For the case of two layers with different orientations (cases *II* and *III*), case *II* experiences a higher *TC*. Thus, for this situation, it is better to utilize Pn-Pol with respect to the outer CFRP layer to take advantage of dielectric heating.

The simulated thermal profile of two cases of Table 2 is presented in Figure 5a (case *I*) and Figure 5b (case *IV*) after 180 sec of microwave illumination. For both cases, a defect of type D2 is considered (between the CFRP and CM). As seen, the temperature rise (based on Eq. 11) for the case of two Pn-Pol CFRP layers (case *I*, Figure 5a) is much greater (by nearly a factor of 10) than the case of two Pr-Pol CFRP layers (case *IV*, Figure 5b).

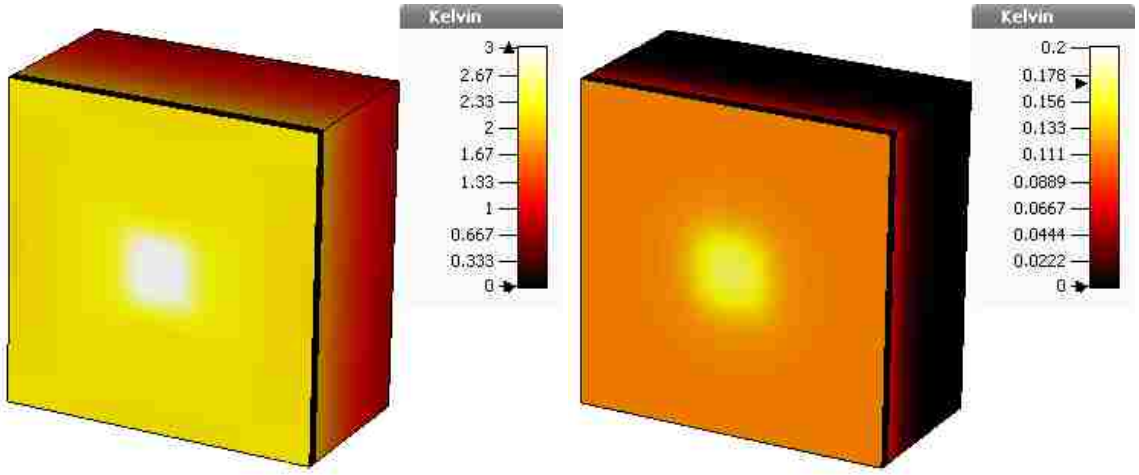

(a) (b)

Figure 5 - Simulated thermal profile for (a) case *I*, and (b) case *IV*.

The effect of frequency was also studied via simulation. Thus far, a frequency of 2.45 GHz was chosen due to prior success with microwave-based CM inspections [9]. However, other frequencies near this value may prove to induce more heat. Therefore, in Figure 6, the *TC* for case *I* (Figure 6a) and case *IV* (Figure 6b) of Table 2 for frequencies from 1- 4 GHz (with a power level of 50 W and heating time of 180 sec) were studied.

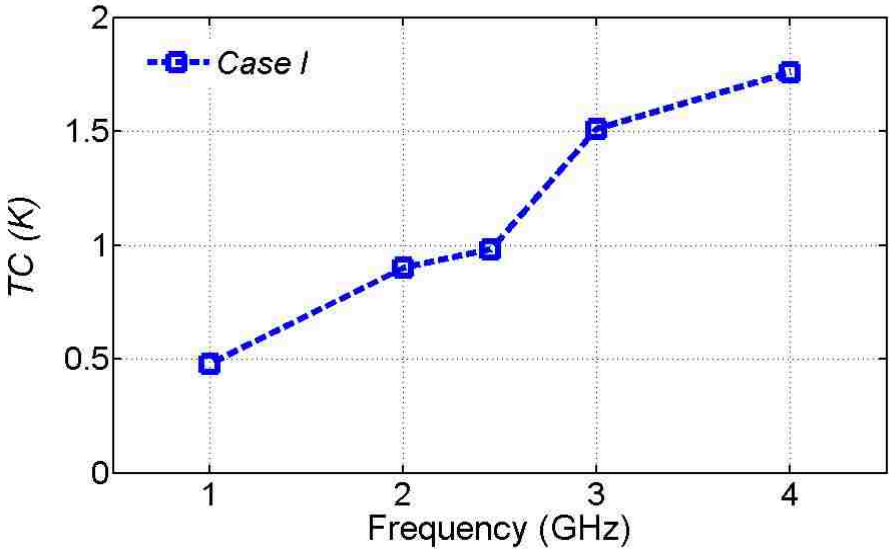

(a)

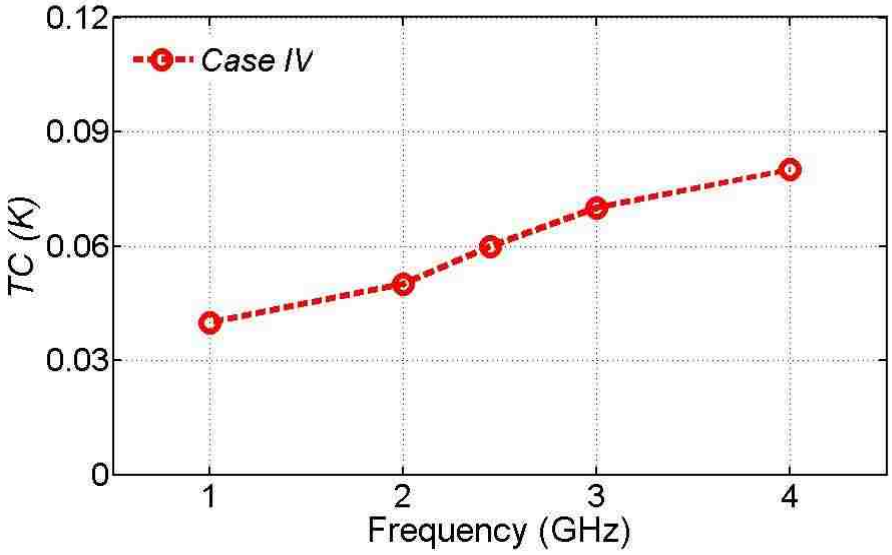

(b)

Figure 6 - *TC* (K) as a function of frequency for case *I* (a), and case *IV* (b)

From the results in Figure 6, it can be observed that the *TC* for case *I* (dielectric heating) is (approximately) linearly proportional to the frequency, as expected from Eq. 8. The effect of higher *TC* at higher frequencies can be explained as an increase in the absorbed electromagnetic energy at these frequencies (i.e., improved *TC*). For case *IV*, the *TC* also exhibits an increase as a function of frequency (due to induction heating), as it is related to the induced surface current and finite conductivity of the CFRP. Therefore, although 2.45 GHz is in an unlicensed frequency band (making it ideal for AMT inspections from a practical point-of-view), utilizing higher frequencies is better for AMT inspections (if possible in practice) for rehabilitated CMs since a higher *TC* can be achieved.

Finally, the effect of source power was investigated. In Table 3, the *TC* for cases *I* and *IV* (of Table 2) at a frequency of 2.45 GHz and heating time of 180 sec as a function of source power (from 50 – 1000 W) is provided. As expected from Eq. 8 and observed from the results of both heating mechanisms, the *TC* is linearly proportional to the power level. However, it is important to note that increasing the incident power is not without drawbacks. That is to say, safety concerns for the operator are increased, and also the cost of the inspection system (financial, thermal management, and power requirements).

Table 3 - *TC* (K) as a function of source power

	TC (K)				
Power (W)	50	100	200	500	1000
Defect D2 - Case *I*	0.98	1.97	3.92	9.85	19.70
Defect D2 - Case *IV*	0.06	0.12	0.23	0.07	1.17

4. AMT MEASUREMENTS – A CASE STUDY

In order to further illustrate the potential for AMT as a structural assessment tool for rehabilitated cement-based structures, measurements were conducted on a representative sample similar to the geometry studied above via simulation. For this project, a mortar sample with an unbond defect was made using a water-to-cement ratio (w/c) of 0.6 and a sand-to-cement ratio (s/c) of 2.0 and was fully cured in ambient conditions for approximately 4 months. Afterward, two layers of uni-directional CFRP laminate (fibers oriented in the same direction) were bonded to the sample's surface. The unbond was created by placing a piece of thin foam (invisible to microwave energy) between the CFRP and mortar layers (i.e., no adhesive). In Figure 7, a schematic and photograph of the AMT measurement setup and sample is shown. In the system, the microwave illumination is generated by a signal generator operating at a frequency of 2.45 GHz. Then, the power level of the signal is amplified using a 50 W power amplifier. The linearly polarized microwave energy was radiated toward the sample using a horn antenna, which is capable of handling high power signals and concentrates the energy toward the surface of the sample. The surface thermal profile of the sample is subsequently captured using a FLIR T430sc thermal camera. Each measurement included 180 sec of microwave illumination (the heating period) followed by an additional 300 sec of measurement (the cooling period).

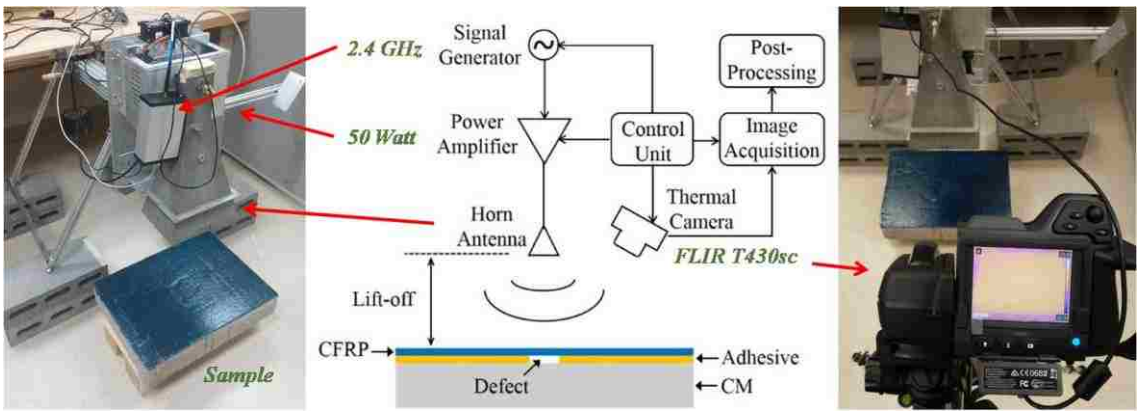

Figure 7 - The AMT system and measurement configuration

During an AMT measurement, the results will be affected by noise (environmental, system, thermal camera, etc.). Therefore, the signal-to-noise ratio (*SNR*) can be used to describe the contrast between a defective area and the surrounding non-defective areas. To define *SNR*, the signal is defined as the *TC*, and the noise is defined as the standard deviation of the temperature in a non-defective area, σ_N. Thus, the *SNR* is expressed as:

$$SNR = 20\log_{10}\frac{TC}{\sigma_N} \tag{13}$$

Strictly speaking, an *SNR* > 0 dB is required for successful defect detections [37].

In Figure 8, the *TC* and *SNR* results for the AMT inspection of the CM sample are presented. In Figure 8a, the temperature increase (defined in Eq. 11) is presented after 5, 10, 20, 60, and 180 sec of microwave illumination with Pn-Pol. As can be seen in Figure 8a, the *TC* increases during the heating time (as is expected). In Figure 8b, the *SNR* (defined in Eq. 13) of the sample is presented after 5, 10, 20, 60, and 180 sec of microwave illumination with Pn-Pol. From this figure, the *SNR* at the defect after 5 sec is 10 dB, and after 60 sec and 180 sec, it is 35 dB and 37 dB, respectively. During an AMT inspection, it is important to provide a sufficient (for defect detection) heating time as well as avoiding excess (either in time or in applied energy) heating. The minimum heating time, (t_{min}) can be determined by analyzing the *SNR* to determine when the *SNR* at the defect is greater than zero. Additionally, in order to avoid unnecessary time/energy spent for heating, it is important to consider the point (in time) in which the *SNR* reaches saturation, t_{sat}. From the results shown in Figure 8b, to detect the defect, t_{min}= ~5 sec. After ~60 sec the *SNR* reaches saturation. Thus, t_{sat} = ~60 sec for this case. The precise (optimal) heating time will lie between this range (5-60 sec) and depends on the capabilities of the thermal camera, material under inspection, etc. This value may differ according to the manufacturing or lamination process of the FRP, or more generally, depending on the material.

In Figure 8c, the surface thermal profile for Pr-Pol is presented. Comparing the results of Pr-Pol with Pn-Pol (Figure 8a and Figure 8c), it can be seen that utilizing Pn-

Pol results in a greater *TC* at the defectat the end of the heating time compared to Pr-Pol. This result was expected from the simulation (Figure 4) and also confirms that dielectric heating is more effective than conductive heating for AMT inspections of CFRP-rehabilitated CM. In addition, it is important to note that the temperature scale for Pn-Pol is 10 times greater than the Pr-Pol (comparing Figure 8c with Figure 8a). Furthermore, since the temperature rise at the defect for Pn-Pol is greater than for Pr-Pol, stronger lateral heat diffusion is observed in Figure 8a as compared to Figure 8c. From the results of *SNR* for Pr-Pol in Figure 8b, t_{min}= ~10 sec (compared to ~5 sec for Pn-Pol). However, t_{sat} = ~60 sec (representing little change in *SNR* from 60 sec to 180 sec) for both polarizations. Thus, inspections utilizing Pn-Pol are preferred since a higher *SNR* and *TC*, as well as faster minimum required illumination time, are achieved.

Finally, σ_N (noise) for both polarizations is presented in Figure 9. For these two cases, the temporal noise in the thermal image is calculated by calculating the standard deviation of temperature over the sample at (randomly selected) non-defective areas. In Figure 9, it is observed (as is expected) that for the case of induction heating (Pr-Pol), the noise on the thermal image varies around 0.03 K, which is very close to the sensitivity level of the thermal camera. Since the only heating mechanism is due to induction heating, the distribution of noise is attributed to the thermal environmental noise and limited sensitivity of the thermal camera. For the case of Pn-Pol, since the heating occurs as a result of dielectric heating and it has a larger temperature increase as compared to Pr-Pol, a stronger lateral heat diffusion exists which leads to an increase (over time) in the amount of noise during the heating period. This value increases from ~0.03K to ~0.05 after 180 sec of heating time and subsequently decreases during the cooling time to ~0.03 K (i.e., environmental and thermal camera noise). Thus, the baseline noise can be considered to be on the order of 0.03 K for this experiment. From this and by characterizing the baseline noise, it can be observed that few seconds are required for inspection of FRP-strengthened structures in order to obtain an *SNR* of greater than zero.

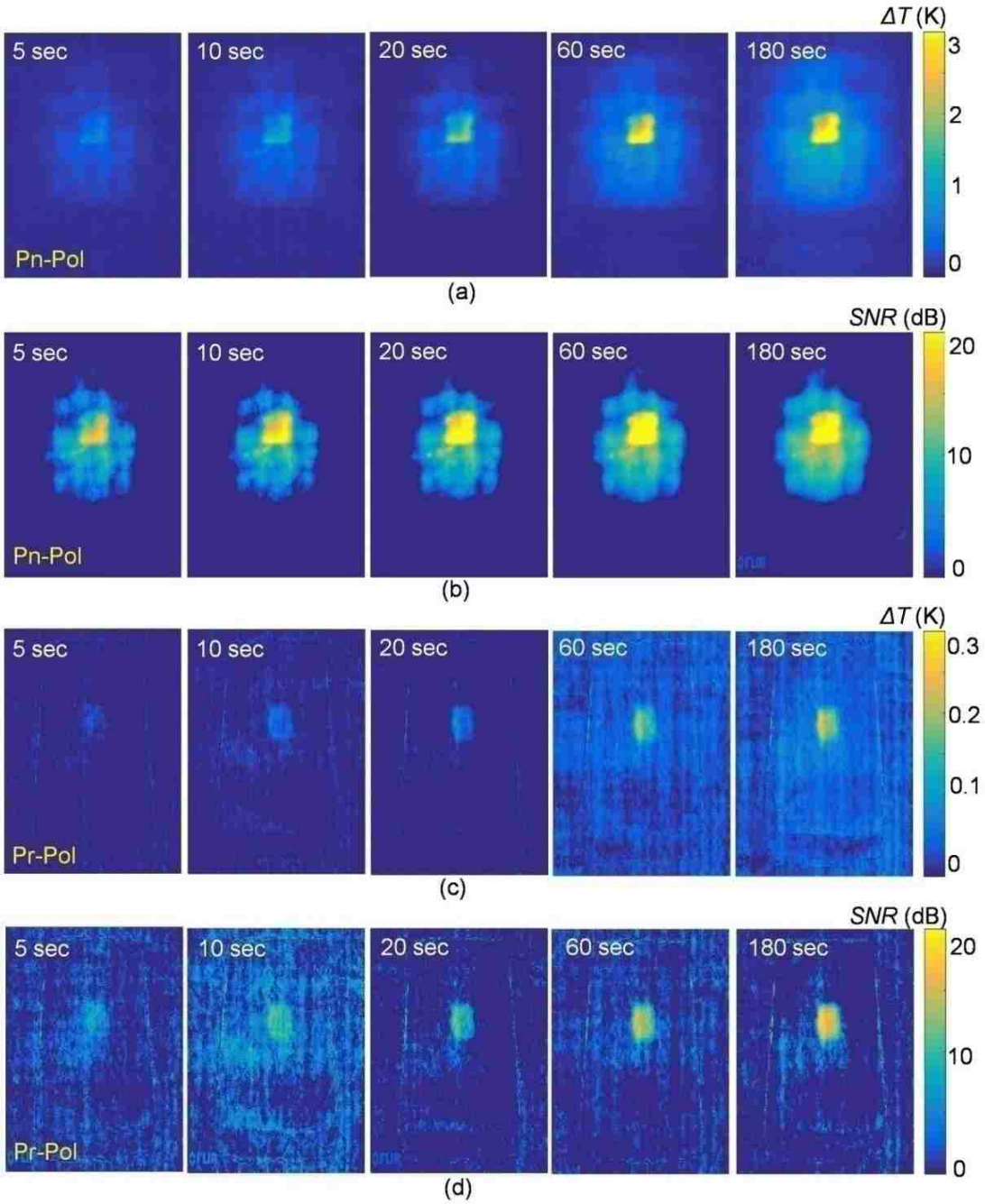

Figure 8 - Results after 5, 10, 20, 60, and 180 sec heating: (a) ΔT profile (defined in Eq, 11) for Pn-Pol, (b) SNR profile for Pn-Pol, (c) ΔT profile for Pr-Pol, and (d) SNR profile for Pr-Pol

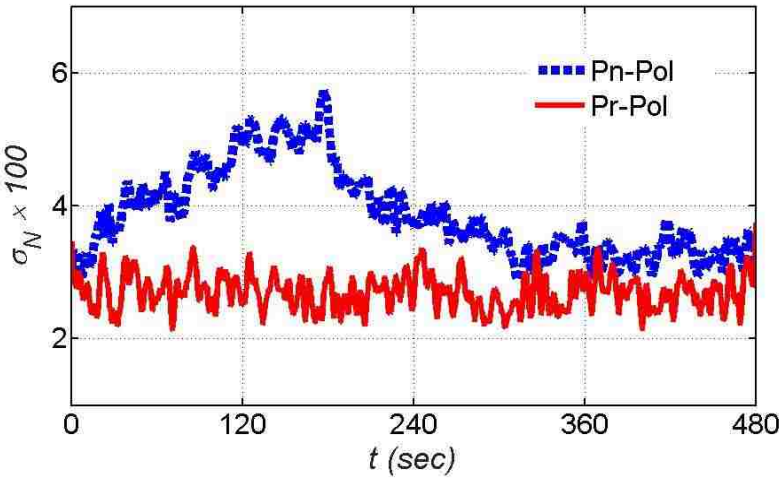

Figure 9 - Temporal noise for both polarizations.

5. CONCLUSION

Active Microwave Thermography (AMT) is a relatively new NDT&E method that has recently been considered for structural assessment in the infrastructure and aerospace industries. To this end, simulation and measurement results using AMT for inspection of cement-based materials rehabilitated with CFRP composites containing an unbond have been presented. Specifically, the effect of fiber orientation (with respect to the polarization of the incident microwave energy), frequency, and power level have been studied. CFRP is conductive when illuminated with microwave energy polarized parallel to the CFRP fiber direction and behaves as a lossy dielectric when illuminated by perpendicularly polarized energy. Since the more significant heating mechanism is based on dielectric heating, a higher thermal contrast (*TC*) and signal-to-noise ratio (*SNR*) between healthy and defective areas can be observed when the incident energy is perpendicular to the fiber direction. From this analysis, it was observed that minimum required heating time to (reliably) detect a defect in cement-based materials rehabilitated with unidirectional CFRP is around ~5 and 10 sec for perpendicular and parallel polarizations, respectively. Also, it was shown that the *SNR* does not improve significantly after ~60 sec of microwave illumination for such a structure, indicating a maximum effective heating time for CFRP strengthened cement-based materials. However, this value may alter according to the type of material and (in the case of composite materials) manufacturing.

REFERENCES

[1] J. Case, R. Zoughi, K. Donnell, D. Hughes, and K. Kurtis; *AIP Conference Proceedings*, 615(1), 498-505,(2002).

[2] A. Foudazi, and K. M. Donnell; IEEE Transactions on Instrumentation and Measurement; 65(7), 1669-1677, (2016).

[3] C. Shearer, A. Foudazi, A. Hashemi, and K. M. Donnell; In IEEE International Instrumentation and Measurement Technology Conference Proceedings (I2MTC), 1-4, (2016).

[4] R. Zoughi; Microwave non-destructive testing and evaluation principles" vol. 4, Springer Science & Business Media, 2000.

[5] N. Qaddoumi, S. Ganchev, R. Zoughi, and G. Carriveau; Materials Evaluation; 53(8), (1995).

[6] A. Foudazi, T. Roth, M. Ghasr, and R.Zoughi; IET Microwaves, Antennas & Propagation; 11(6),811-817, (2016).

[7] R. Zoughi; Research in Nondestructive Evaluation; 7(2-3), 71-74, (1995).

[8] R. Zoughi, J. R. Gallion, and M. T. Ghasr;IEEE Transactions on Instrumentation and Measurement; 65(4), 951-953,(2016).

[9] A. Hashemi, M. Horst, K. E. Kurtis, K. M. Donnell, and R. Zoughi; IEEE Transactions on Instrumentation and Measurement; 64(7), 1907-1915, (2015).

[10] I. Mehdipour, M. Horst, R. Zoughi, and K. H. Khayat; Journal of Materials in Civil Engineering;04017029,(2017).

[11] A. Mirala, and R.Sarrafshirazi; IET Microwaves, Antennas & Propagation; 11(4), 564-569, (2017).

[12] A. Poudel, J.Strycek, and T. P. Chu; Materials Evaluation; 71(8), 987-994, 2013.

[13] W. Zhu, J. L. Rose, J. N. Barshinger, and V. S. Agarwala; Research in Nondestructive Evaluation; 10(4), 205-225, 1998.

[14] A. Poudel, and T.P.Chu; Materials Evaluation; 70(10), (2012).

[15] S. Maillard, J. Cadith, D. Eschimese, H. Walaszek, H. Mooshofer, J. C. Candore, and J. L. Bodnar; In QIRT congress proceedings, Laval. (2010).

[16] X. Maldague; Materials Evaluation; 60(9), 1060-1073, (2002).

[17] C. Ibarra-Castanedo, and X. Maldague, Infrared thermography; Chapter 10, In Handbook of Technical Diagnostics, pp. 175-220. Springer Berlin Heidelberg, 2013.

[18] C. Ibarra-Castanedo, J. Piau, S. Guilbert, N. Avdelidis, M.Genest, A. Bendada, andX. Maldague; Research in Nondestructive Evaluation, 20(1), pp.1-31, (2009).

[19] A. Poudel, K. R. Mitchell, T. P. Chu, S. Neidigk, and C. Jacques; Journal of Composite Materials,50(3), 351-363, (2016).

[20] H. Zhang, R. Yang, Y. He, A.Foudazi, L. Cheng, and G. Tian; Sensors; 17(5), 17.

[21] R. Yang, and Y He; Infrared Physics & Technology,(75), 26-50, (2016).

[22] D.Vasic, V. Bilas, and D. Ambrus; IEEE Transactions on Instrumentation and Measurement; 53(4), 1289-1294, (2004).

[23] J. Wilson, G. Y. Tian, I.Abidin, S. Yang, and D. Almond; Nondestructive Testing and Evaluation; 25(3), 205-218, (2010).

[24] J. Saniie, M. Luukkala, A. Lehto, and R. Rajala; Electronics Letters, 18(15), 651-653, (1982).

[25] J. G. Thompson, C. T. Uyehara;U.S. Patent 7,075,084,(2006).

[26] C. A. DiMarzio, C. M. Rappaport, W. Li, M. E. Kilmer, and G. O. Sauermann; Proc. SPIE, Photonics East (ISAM, VVDC, IEMB), 337-342, (1999).

[27] D. Balageas and P. Levesque; in Proc. QIRT, 71–78, (2002).

[28] S.-A. Keo, D. Defer, F. Breaban, and F. Brachelet; Mater. Sci. Appl., 4(10), 600–605, (2013).

[29] D. Pieper, K. M. Donnell, M. T. Ghasr, and E. C. Kinzel. In AIP Conference Proceedings, 1581(1) 1560-1567, (2014).

[30] A. Foudazi, I. Mehdipour, K. M. Donnell, and K. H. Khayat, In 14th International Symposium on Nondestructive Characterization of Materials (NDCM2015), 22-26, (2015).

[31] A. Foudazi, I. Mehdipour, K. M. Donnell, and K. H. Khayat; Materials and Structures;49(12), 5051-5065, (2016).

[32] A. Foudazi, M. T. Ghasr, and K. M. Donnell; IEEE Transactions on Instrumentation and Measurement; 64(9), 2583-2585, (2015).

[33] A. Foudazi, M. T. Ghasr, and K. M. Donnell; In 2014IEEE AUTOTESTCON; 318-322, (2014).

[34] A. Foudazi, K. M. Donnell, and M. T. Ghasr; In Proceedings 2014 IEEE International Instrumentation and Measurement Technology Conference (I2MTC), 1567-1571, (2014).

[35] A. Foudazi, C. Edwards, M. Ghasr, and K. Donnell; IEEE Transactions on Instrumentation and Measurement;65(11),2612-2620, (2016).

[36] S. Orfanidis; Electromagnetic waves and antennas. New Brunswick, NJ: Rutgers University, (2002).

[37] K. Srinivas, A. Siddiqui, and J. Lahiri; In Proc. National Seminar on Non-Destructive Evaluation, 12, 7-9,(2006).

III. EVALUATION OF STEEL FIBER DISTRIBUTION IN CEMENT-BASED MORTARS USING ACTIVE MICROWAVE THERMOGRAPHY

ABSTRACT

The non-uniform distribution of steel fibers in fiber-reinforced cement-based mortars (FRCMs) can lead to heterogeneous properties of hardened material with direct impact on mechanical properties. Among various nondestructive testing techniques, the active microwave thermography (AMT) has shown good potential for inspection of cement-based materials. AMT utilizes combination of microwave energy to generate controlled and localized heating and uses commercially-available infrared cameras to capture surface thermal images in real-time. Utilizing AMT, four FRCM samples made with different steel fiber volumes ranging from 0 to 3% were investigated to evaluate the feasibility of this method for detecting and quantifying fiber distribution. Full-wave coupled electromagnetic-thermal numerical modeling was also conducted to evaluate the effect of dielectric properties, fiber depth, and fiber clumping on surface thermal profile. The results of simulations indicate that increase in fiber depth results in lower surface temperature, due to lower heating associated with induced surface current. Based on AMT measurement results, samples with higher fiber contents were shown to undergo greater increase in surface temperature, as observed for samples with 1% and 2% fibers. However, this tendency was reversed with further fiber addition from 2% to 3%, due to the potential of fiber clumping. Furthermore, the fiber clumping and lower level of fiber homogeneity for FRCM with 3% fiber resulted in 55% lower flexural toughness compared to the FRCM containing 2% fiber. The results of fiber homogeneity measured from freshly cast prism were found to correlate well with those obtained from AMT technique determined on hardened samples.

Index Terms-Active microwave thermography, Fiber-reinforced cement-based mortar, Fiber clumping, Fiber distribution, Nondestructive testing, Steel fiber.

1. INTRODUCTION

Cement-based materials are typically characterized as brittle materials, with relatively low tensile strength and strain capacity. Fibers can be incorporated to reduce cracking tendency and improve post-cracking response and energy absorption capacity. Numerous research studies have been carried out to evaluate the effect of fiber content, geometry, and type on workability and rheological properties, as well as mechanical characteristics of cement-based materials [1]-[5].

The effectiveness of incorporating fibers to enhance mechanical properties of cement-based materials is significantly affected by the fiber distribution [6]-[15]. Non-uniform fiber distribution can lead to mechanical anisotropy in some regions of a structural element, resulting in an undesirable variability in mechanical performance of fiber-reinforced mortar and concrete mixtures. For example, [6] reported that the number of fibers in a cross-section of a test sample significantly affects the mechanical properties of fiber-reinforced concrete (FRC). [12] pointed out that the measured flexural strength of FRC can be significantly lower compared to the predicted flexural strength when fibers are non-uniformly distributed throughout the sample.

The level of fiber distribution in FRCMs is affected by the fiber characteristics, including type, V_f (volume content), aspect ratio (L_f/d_f , where L_f and d_f refer to fiber length and diameter, respectively) [4], [5] workability and rheological properties of the suspending fluid [8]-[10] and [13]-[16], method of introducing fibers into the mixture [17], and casting methods [18].

Given the interaction between fibers, the incorporation of fibers can result in a reduction in the workability of FRCMs. A decrease in workability can adversely reduce the homogeneity of fiber distribution in FRCM. In the case of relatively low fiber volume, the workability of FRCMs may not be significantly affected, given the lower level of potential interaction and larger distance between individual fibers. As fiber volume increases, the interaction between fibers increases, thus reducing workability. Beyond a certain fiber content, the interaction among fibers can substantially increase, potentially leading to the formation of fiber clumping (or fiber balling). Fiber clumping can form a non-uniform fiber distribution throughout the mixture, which can result in significant reduction in workability and mechanical properties.

From a structural health monitoring point-of-view, the evaluation of fiber distribution in FRCMs is of high importance to ensure adequate performance. Several destructive and nondestructive testing (NDT) techniques have been employed to evaluate fiber distribution in fibrous mortar and concrete mixtures. The most common approach involves cutting sample and evaluating fiber distribution. This technique is destructive and time-consuming, and the results cannot be generalized to the entire structure [6], [11], and [12]. Alternatively, NDT techniques can be employed for assessing the fiber distribution and orientation, including X-ray tomography [19]-[21], image processing analysis [16] and [22], electrical resistivity (Lataste et al. 2008), alternating-current impedance spectroscopy (AC-IS) [24], ultrasonic and quantitative acoustic emission technique [25], as well as a magnetic method [26]-[28].

Among the various NDT techniques, X-ray tomography is quite useful for evaluating fiber distribution. However, there are a number of critical (operator) safety issues that should be taken into consideration, and the technique is mainly used in the laboratory. Ultrasonic measurements require contact with the sample under test, which may be difficult in some restricted structures. Ultrasonic methods are sensitive to measurement errors resulting from the noisy atmosphere of most job sites. Microwave NDT has shown good potential for determining material constituents of cement-based materials [29] and [30], but microwave imaging (i.e., raster scanning of large areas) is often time consuming. Thermography is a well-established NDT method which is used extensively for structural health monitoring with numerous benefits, including noncontact inspection, fast, readily available high-sensitivity cameras, and easy-to-interpret results [31]-[33]. However, thermography often requires the application of high thermal energy over a short period of time, which results in a sudden temperature rise (e.g., greater than ~15 °K) [32]. Such temperature increases may risk damaging the material under test. Hence, in order to overcome this risk and improve the method as an efficient NDT tool, microwave NDT has been integrated with thermography, herein referred to as active microwave thermography (AMT) [34]-[37]. AMT utilizes the combination of microwave energy to generate controlled and localized heating and commercially-available infrared (thermal) cameras to capture surface thermal images of a structure under test in real-time. AMT has shown potential as an NDT solution for various applications in the

transportation and aerospace industries, including detection of delamination and debonding in structures rehabilitated with carbon fiber reinforced composites [34] and [35], as well as corrosion detection in steel-based materials [36].

The objective of this study is to investigate the feasibility of AMT to evaluate the fiber distribution in FRCM samples prepared with various steel fiber contents. In order to assess the sensitivity of different frequencies to the fiber content and distribution, AMT measurements were conducted at 2, 2.4, and 3 GHz. Full-wave coupled electromagnetic-thermal numerical modeling was also conducted to evaluate the effect of dielectric properties, fiber depth, and clumping of fibers on the surface thermal profile. In addition, the effect of fiber addition on packing density, paste film thickness (PFT) covering fibers, flow consistency, as well as flexural toughness was also evaluated. The level of fiber homogeneity along the freshly cast prism was determined, and the results were correlated with those obtained from AMT technique.

2. ACTIVE MICROWAVE THERMOGRAPHY

As mentioned above, AMT is based on the integration of microwave and thermographic NDT techniques. As AMT utilizes a microwave heat excitation, two different heating mechanisms can be generated depending on the material properties of the structure under test. The first heating mechanism is based on dielectric heating which takes place due to the interaction between dielectric materials (i.e., non-conducting materials) and incident electromagnetic energy. Dielectric materials are defined by their complex relative (to free-space) dielectric properties, ε_r, given by:

$$\varepsilon_r = \varepsilon_r' - \mathrm{j}\varepsilon_r'' \tag{1}$$

where ε_r' and ε_r'' refer to the permittivity and loss factor, respectively. Permittivity represents the ability of a material to store microwave energy, and loss factor refers to the ability of the material to absorb microwave energy. The amount of (dielectric) heat generated for a given material is related to the loss factor, operating frequency, and

incident power. Assuming a plane-wave excitation (i.e., a uniform electric field with a constant phase front/no phase variation) with an (initial) magnitude of E_0 irradiated toward the dielectric material, the magnitude of this incident signal, $E(z)$, a distance of z from the surface of the dielectric is expressed as:

$$E(z) = E_0 e^{-\alpha z} \tag{2}$$

where α represents the attenuation constant (Np/m) which is calculated as follows:

$$\alpha = \frac{\omega}{c}\sqrt{\frac{\mu_r \varepsilon_r'}{2}\left[\sqrt{1+(\frac{\varepsilon_r''}{\varepsilon_r'})^2}-1\right]} \tag{3}$$

where $\omega = 2\pi f$ (rad/m), f is the operating frequency (Hz), c is the speed of light (3×10^8 m/s), and μ_r is the relative magnetic permeability ($\mu_r = 1$ for dielectric/non-magnetic materials). As shown in Eq. (3), higher operating frequency or loss factor can lead to increased attenuation of the incident wave in the dielectric material. Knowing the magnitude of the incident electric field ($|E|$) inside the dielectric material (at any point) allows for the dissipation of electromagnetic energy, Q (W/m^3) in the material to be determined as follows:

$$Q = \omega\, \varepsilon_0\, \varepsilon_r''\, |E|^2 \tag{4}$$

where ε_0 is the dielectric constant of free-space (8.854×10^{-12} F/m). The energy dissipated inside the dielectric material is subsequently related to a change (with respect to time and space) in temperature (i.e., heat generation) based on the heat transfer equation, expressed as:

$$\rho C \frac{\partial T}{\partial t} = k \frac{\partial^2 T}{\partial^2 z} + Q \tag{5}$$

where ρ is the density (kg/m^3), C is the specific heat (J/g.K), k is thermal conductivity (W/m.K), T is temperature (K) and t is time (sec).

The second heating mechanism in AMT occurs when conductive materials are present. As outlined in [32] and [34], when a conductor is irradiated with electromagnetic energy, surface currents (J) are induced on the conductor. Such surface currents serve as a secondary source of radiated electromagnetic energy which can generate an additional (secondary) source of heat. When a conductor is embedded within a lossy dielectric material (i.e., $\varepsilon_r'' \neq 0$), these surface currents will cause an increase in the concentration of electromagnetic energy (as compared to areas without a conductor). Hence, through Eq. (5), the presence of embedded conductors inside lossy dielectric materials will cause an increase in heat and subsequent temperature.

In this work, since steel fibers (an electrically conductive material) are distributed inside the mortar (a lossy dielectric material), the potential for both heating mechanisms exists. More specifically, when an FRCM is illuminated with electromagnetic energy, the material will experience (volumetric) dielectric heating as the electromagnetic energy propagates into the material. Furthermore, at the location of steel fibers, the induced surface current leads to an additional increase in temperature. The variation in surface temperature can be utilized to distinguish areas with fibers from those without fibers. Further, the variation in surface temperature is dependent on the fiber characteristics (length and volume), depth of fibers (from the surface), etc. For a given fiber distribution, fibers located further from the surface could experience less induced surface current due to the increased attenuation of the incident electromagnetic energy (see Eq. (3)). Thus, those fibers could contribute less to the temperature variation on the surface.

3. RESEARCH METHODOLOGY

The research program undertaken in this investigation consisted of three phases. In the first phase, a coupled electromagnetic-thermal model was utilized to evaluate the effect of dielectric properties, depth and clumping of fibers on the surface thermal profile. The second phase aimed at quantifying the effect of fiber content on fresh and mechanical properties of the investigated FRCMs. The evaluated properties included

packing density of dry mixture of fibers and sand particles, paste film thickness (PFT) covering fibers, flow consistency, as well as flexural toughness. A methodology was also employed to assess the fiber homogeneity along the prism in the fresh state. The third phase was undertaken to assess the fiber content and distribution of FRCM samples using AMT. The significance of variations in the mean value of the surface temperature of FRCM samples were statistically assessed using the analysis of variance (ANOVA) test.

3.1. MATERIALS, MIXTURE PROPORTIONING, AND SAMPLE PREPARATION

In total, four mortar mixtures were prepared. This included a control mixture made without fiber and three mixtures with fiber volumes of 1%, 2%, and 3%. All mortar mixtures were proportioned with a fixed water-to-cement ratio (w/c) of 0.45 and sand-to-cement ratio (s/c) of 2.5. The mixtures were prepared using Type I ordinary portland cement (OPC) and continuously graded natural sand with a maximum size of 4 mm, specific gravity of 2.70, water absorption of 2.8%, and fineness modulus of 2.6. The mortar mixtures did not incorporate any chemical admixture. This was done to reduce the flowability of mixtures with higher fiber content, and eventually fiber clumping would be detected using the proposed NDT technique. Hooked-end steel fibers with lengths of 30 mm, diameters of 0.55 mm, specific gravity of 7.87, and tensile strength of 1500 MPa were used.

The mixing sequence consisted of homogenizing the sand for 30 seconds before introducing half of the mixing water. Cement was added and mixed for 30 seconds followed by the remaining water. The fibers were then gradually introduced, and the mixture was mixed for 3 minutes and kept at rest for 2 minutes before remixing for 3 minutes. Visual observation during mixing indicated that the mixture with 3% fiber volume developed fiber clumps, and the mixture exhibited signs of bleeding and fiber clumping.

The casting procedure of the FRCM has significant influence on the distribution of fibers along the prism, and consequently on mechanical properties. In this study, all FRCMs were cast parallel to the longitudinal direction of the prism. All samples were

cast in two layers, and consolidated on a vibrating table for 30 seconds. The samples were demolded after one day, and were subjected to standard moist curing (23 ± 1°C and 100% RH) until the age of testing at 28 days.

3.2.TEST METHODS

3.2.1. Fresh And Hardened Properties Of FRCMS. a) Flow consistency: The flow consistency of mortars was evaluated using the flow table test, in accordance with ASTM C1437, where the mortar is subjected to 25 drops in 15 seconds after removal from a cone-shaped mold. The flow is calculated as the percentage of the difference between the spread diameter of mortar after the 25th drop and the original base diameter divided by the original base diameter.

b) Packing density and determination of paste film thickness covering fibers: The effect of fiber addition on packing density of dry mixture of sand particles and fibers was evaluated in accordance with ASTM C29. The results of packing density were subsequently used to quantify the effect of fiber addition on paste film thickness (PFT) covering fibers and sand particles. In order to determine the PFT surrounding fibers and sand particles, the FRCM was considered as a two-phase composite, including solid (fibers and sand particles) and suspending fluid (cement paste). The suspending fluid initially fills the voids between solid particles, and then covers the constitutive materials of the first phase. The thickness of the paste layer covering the fibers and sand particles, corresponding to the PFT, can be estimated using the total surface area and void volume (V_V) of the solid phase. The $V_V$is calculated by measuring the packing density of the solid phase, which depends on the volume, shape, rigidity, and interaction between sand particles and fibers. The PFT around the sand and fibers can be expressed as follows:

$$PFT = \frac{1 - V_A - V_{V(A,f)} - V_f}{A_A + A_f} \tag{6}$$

where V_A and V_f are the volumes of aggregate and fiber, respectively. $V_{V(A,f)}$ refers to the void volume between sand particles and fibers in a dry mixture. A_A andA_f refer to the

total surface areas of aggregate and fibers, respectively. The total surface area for rigid steel fibers can be expressed as follows:

$$A_f = \frac{4V_f}{d_f} \tag{7}$$

c) Assessment of fiber homogeneity in fresh state: A simple test method was implemented to quantitatively evaluate the variation of fiber content along a cast prism in fresh state. This test involves determining the variation in fiber content along a cast prism measuring 75 × 75 × 285 mm. The test procedure is schematically presented in Figure 3.1. It consists of casting the FRCM parallel to the longitudinal direction of the prism followed by inserting thin metal plates into the plastic mixture shortly after casting to separate the prism into four zones. The FRCM in each section are weighed, then washed out on a 75 µm sieve to determine the fiber content retained on the sieve. The variation of fiber content throughout the mixture was quantified by calculating the inhomogeneity index (*IHI*). The *IHI* is considered to be the coefficient of variation (*COV*) of the fiber content of four zones along the cast prism and is expressed as follows:

$$IHI(\%) = \frac{\sqrt{\frac{1}{4}\sum_{i=1}^{4}(M_{Fi} - M_{Fave})^2}}{M_{Fave}} \times 100 \tag{8}$$

where M_{Fi} refers to the fiber content in each zone and M_{Fave} represents the average fiber content corresponding to all four zones along the cast prism.

d) Flexural toughness: Prismatic samples measuring 75 × 75 × 400 mm were cast to determine the 28-day flexural strength and toughness, in accordance with ASTM C1609. The results of flexural toughness represent the mean values of three samples.

3.2.2. AMT Measurements. The AMT measurements were conducted on FRCM samples with dimensions of 200 × 200 × 200 mm. After demolding at 24 hours, samples were stored in a temperature and humidity controlled room at 23 ± 2 °C and 35% ± 5% RH until the age of AMT measurement at 28 days. The AMT measurement test setup is schematically illustrated in Figure 2. A signal generator was utilized to produce a microwave signal at the desired frequency. The power level was amplified using a 50 W power amplifier. The microwave energy was radiated toward the FRCM sample using a horn antenna. The horn antenna is capable of handling high power microwave signals as well as concentrating the microwave energy toward the surface of the sample and providing a relatively uniform microwave excitation (similar to a plane wave). In order to measure the surface thermal profile, a DRS Tamarisk 320 thermal camera was utilized. Each measurement included 30 sec of microwave illumination followed by an additional 90 sec of thermal measurements (i.e., measurements continued during the cooling period).

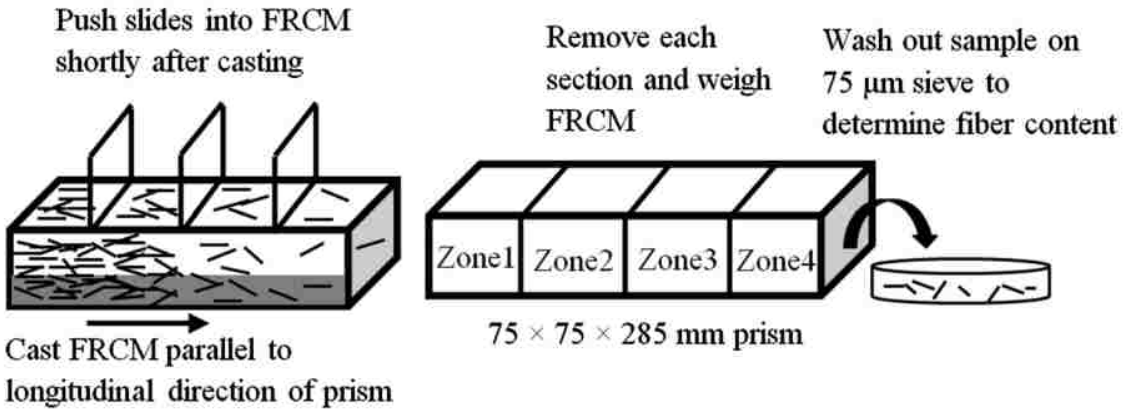

Figure 1 - Experimental procedure for evaluating fiber inhomogeneity along cast prism in fresh state

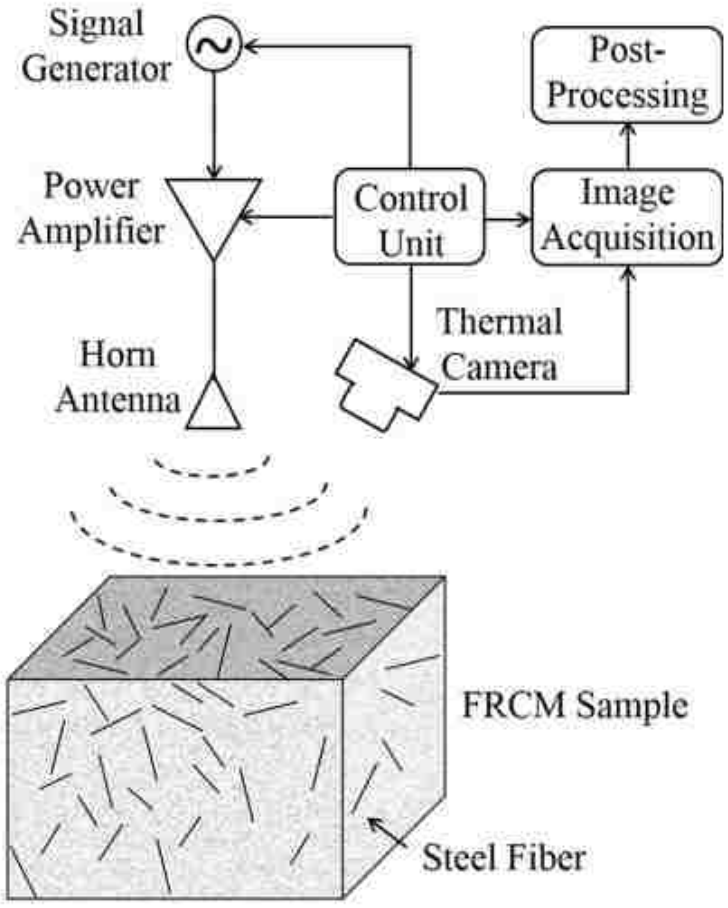

Figure 2 - AMT measurement test setup

The AMT measurements were conducted on the four sides of the samples, excluding the top and bottom surfaces (since these surfaces have some roughness which may affect the AMT results). Considering a frequency of 2.4 GHz (midpoint of the frequencies utilized here) and a mortar with permittivity of 4.8, the wavelength in air and mortar is 125 mm and 57 mm, respectively. Thus at this frequency, the length of steel fiber (30 mm) is near the resonant length (i.e., half of the wavelength of the signal in mortar, 28 mm), and the maximum current distribution on the fiber surface will be induced. For areas containing steel fibers, the induced surface current on the steel fibers contribute to a larger temperature difference (as explained above). As such, it is expected that the temperature will increase with increasing volume content of steel fibers.

An illustration of the thermal image acquisition process is shown in Figure 3. The temperature profile was acquired at a rate of 1/30 sec, resulting in a frames-per-second rate of 1/30. All acquired frames, *T(t)*, were subtracted from the first frame (i.e., ambient condition, *T(0)*) in order to highlight the temperature changes taking place during testing. As shown in Figure 3, initially a temperature difference of zero is measured (as for the first measured frame, no microwave heating has taken place) for all measurement points (example measurement points shown as *u*, *v*, and *w* in Figure 3). Then, after the microwave illumination begins, the temperature difference increases. In the zone surrounding point *u*, the concentration of fibers is higher than those near points *v* and *w*. As a result, the temperature difference in zone *u* will be larger, as illustrated in Figure. 3. Also, the zone near point *v* will experience a greater temperature difference than areas with no fibers (i.e., around point *w*). Additionally, the temperature difference decreases after the microwave excitation is removed (during the cooling period) for all points.

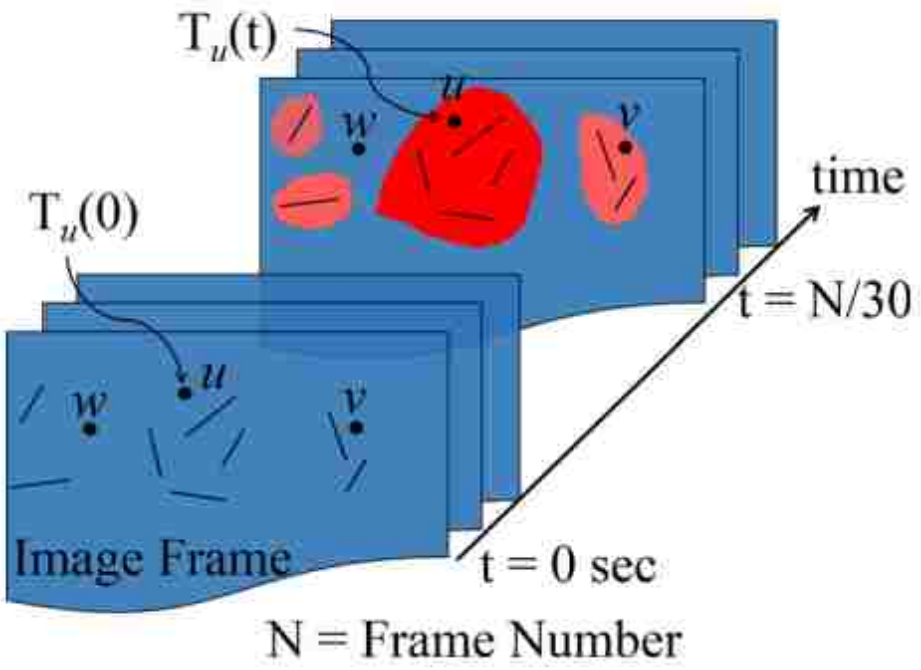

Figure 3 - Illustration of image acquisition

In order to quantitatively evaluate the fiber distribution along the surface of an FRCM sample, the middle portion of each surface can be divided into few equivalent zones, and the results of each zone can be used to evaluate fiber distribution. The mean temperature at time *t* for the corresponding surface (*s*) and zone (*z*), $\mu_{Zone}(s,z,t)$, can be calculated as follows:

$$\mu_{Zone}(s,z,t) = \frac{1}{N_P}\sum_{p=1}^{N_P}\Delta T_p(t) \tag{9}$$

where $\Delta T_p(t)$ is the temperature difference at pixel *p* and time *t*, and N_P refers to total number of pixels for a corresponding zone. Then, the overall mean of the temperature difference of each sample ($\mu_{total}(t)$) can be expressed as follows:

$$\mu_{total}(t) = \frac{1}{N_S N_Z}\sum_{s=1}^{N_S}\sum_{z=1}^{N_Z}\mu_{Zone}(s,z,t) \tag{10}$$

where N_Z and N_S refer to the number of zones and surfaces, respectively, of each tested sample. Since the presence of fiber affects the surface temperature (through induced surface current mechanism), a comparison of mean values ($\mu_{Zone}(s,z,t)$) of each zone across the surface may provide an indication of the fiber distribution of test sample. Thus, it is expected that the concentration of fibers can be quantitatively evaluated by analyzing the mean of the temperature difference at each zone.

4. NUMERICAL SIMULATION OF AMT

For numerical modeling, a full-wave coupled electromagnetic-thermal simulation was conducted to evaluate the effect of dielectric properties and fiber depth and clumping on the surface temperature of FRCM samples using CST MultiPhysicsStudio™. The simulation was carried out in two parts. First, assuming a 50 W plane wave excitation, the

electric and magnetic fields inside the FRCM and subsequently the induced surface current on the steel fibers were determined. The solution is based on the finite difference time domain technique. Subsequently, for the thermal simulation, the computed electric and magnetic fields and induced surface current are utilized to determine the transient heat diffusion. The transient thermal response (i.e., heat generation, diffusion, etc.) of the structure is based on Eq. (4). The transient thermal simulation includes two parts, in which the FRCM is first illuminated by incident electromagnetic power (i.e., heating period) for a given heating time, t_h, and subsequently the heat source is removed (i.e., cooling period) and the thermal profile is recorded for a given cooling time, t_c (i.e., total time of $t = t_h + t_c$). For numerical modeling, the operating frequency was chosen to be 2.4 GHz with 50 W of incident electromagnetic energy (plane wave illumination). As in [38] at low frequencies, such as 2.4 GHz, the mortar sample can be considered a homogeneous material. Therefore, each mortar sample was modeled as a homogeneous solid material measuring 140 × 140 × 70 mm. The steel fiber was modeled with a length of 30 mm and diameter of 0.55 mm. The dielectric and thermal properties of the material constituents of FRCM sample were considered as follows: mortar was assumed to have a dielectric properties of $\varepsilon_r = 4.8 - j0.05$,thermal conductivity of $k = 1.2$ W/m.K, specific heat of $C = 0.9$ J/g.K, and density of $\rho = 2200$ kg/m^3; air has dielectric properties of $\varepsilon_r = 1$, $k = 0.026$ W/m.K, $C = 1.005$ J/g.K, and $\rho = 1.204$ kg/m^3; steel fiber was considered to have electric conductivity of $\sigma = 7.69 \times 10^6$ (S/m), $k = 59.5$ W/m.K, $C = 0.48$ J/g.K, and $\rho = 7870$ kg/m^3.

4.1. EFFECT OF EMBEDDED SINGLE FIBER ON SURFACE TEMPERATURE

The first phase of numerical simulation was undertaken to evaluate the effect of mortar loss factor and the depth (from the surface) of a single steel fiber on the surface temperature profile. The fiber depth and loss factor of mortar contributes to change in temperature due to induced surface current and dielectric heating, respectively. The surface temperature difference of a sample as well as induced surface current on steel

fiber at t_h = 30 sec is shown in Figure 4(a). Assuming fixed mortar dielectric properties, the surface temperature reduces as the fiber depth increases. As expected, the surface current induced by the incident electromagnetic signal decreases since the amount of energy that reaches the fiber decreases with distance from the surface (see Eq. (4)). For this material, after 8 mm, the fiber depth does not affect the temperature. Thus, fibers placed deeper than ~10 mm are not likely to contribute to the surface temperature (nor AMT inspection results).

Related to this, the induced surface current on the steel fibers is also a function of the fiber orientation with respect to the polarization of incident electric field. The effect of incident polarization on the fiber can be quantified using through the polarization loss factor [39]. In general, the greatest induced surface current occurs when the fiber is parallel to the incident electric field, and approaches zero for a perpendicular orientation of the fiber. This dependency on fiber orientation causes a subsequent dependency of surface temperature (and overall AMT sensitivity) to the fiber alignment.

The temperature difference on a sample without and with a single fiber (located 1 mm from the top surface) along with induced surface current on fiber is shown in Figure 4(b) as a function of loss factor. For the mortar without fiber, the surface temperature increases with increasing loss factor (resulting from dielectric heating). However, in the case of mortar with a single steel fiber, as the loss factor increases, the temperature difference initially also increases as a result of both dielectric heating and induced surface current on the fiber (up to a loss factor of ~0.6). After this point, the contribution of the induced surface current (on the fiber) is less dominant, and therefore the temperature difference begins to decrease. This is a result of the increased attenuation of the electric field impinging on the fiber (and subsequently a reduction in induced surface current). Therefore, the temperature difference between samples made with and without fibers is highly dependent on the material properties (dielectric properties) of mortar.

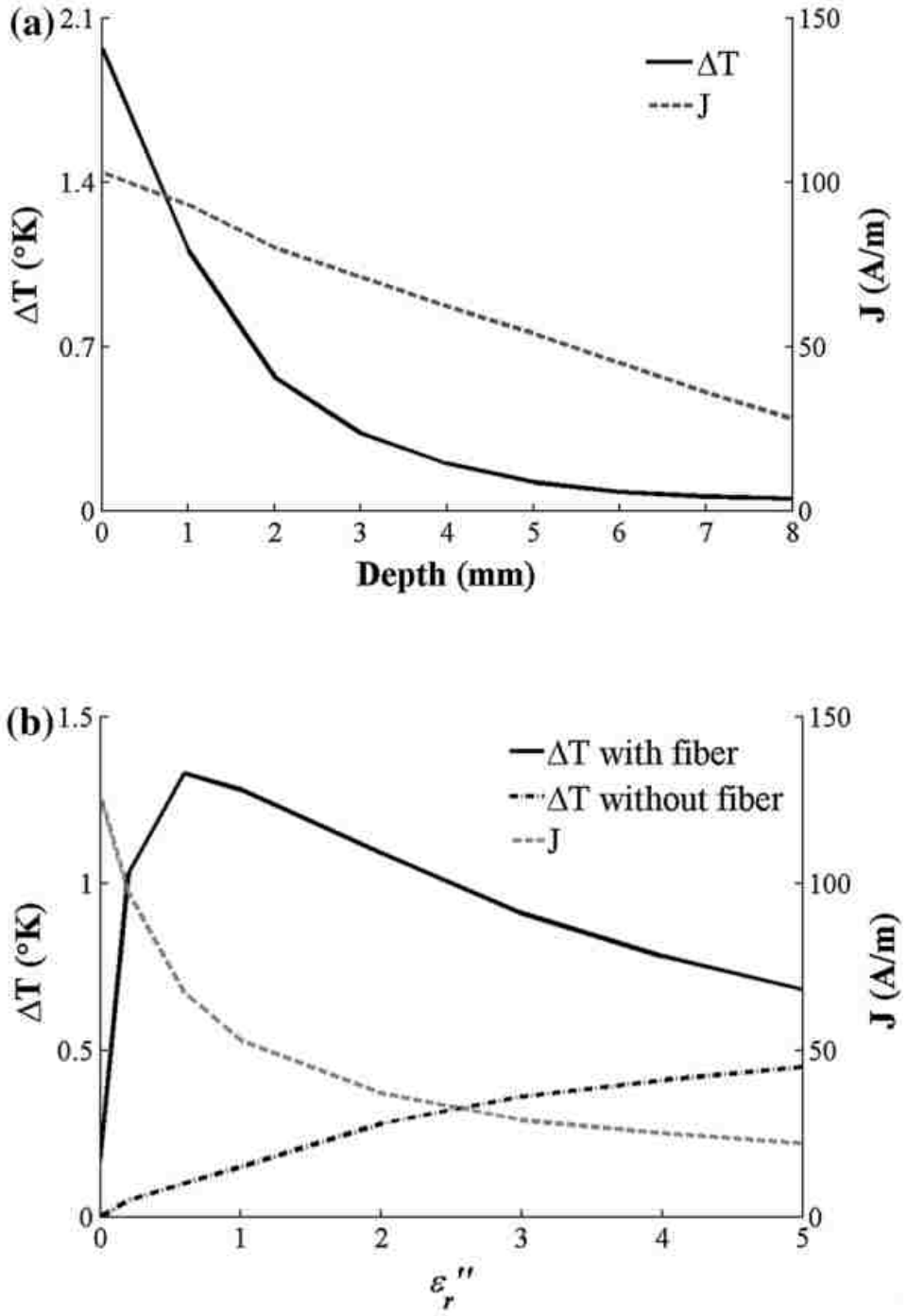

Figure 4 - Simulated surface temperature and induced surface current on fiber for sample with a single fiber a variation in fiber depth and b variation in sample loss factor

4.2. EFFECT OF FIBER DISTRIBUTION ON SURFACE TEMPERATURE

The second simulation phase was carried out to evaluate the effect of fiber distribution on surface temperature for sample containing 0.5% steel fibers. Two different fiber distributions were considered; namely, a random distribution and a clumped distribution, as shown in Figure 5. For both distributions, the fibers were distributed within the first 50 cm (i.e., a 50-cm depth from the surface) of the sample. The location and orientation of the i^{th} fiber was determined by generating a random Cartesian starting position (x_i, y_i, z_i) within the geometrical boundaries of the sample, and the direction of the fiber was randomly assigned using angles θ_i and ϕ_i of the spherical coordinate system. For both distributions, the depth and orientation (θ_i and ϕ_i) are identical. The difference between the distributions is in the lateral placement (i.e., x and y directions as shown in Figure 5), meaning that the randomly distributed fibers cover a greater (lateral) surface area than the clumped distribution. The magnitude of electric field (E-field) and temperature difference for both distributions are shown in Figure 5. From these results, it can be seen that the E-field distribution is affected by the fiber distribution. In the case of clumped distribution, the E-field and temperature values were substantially higher at the center of the sample and rapidly decreased with distance from the center. Therefore, in the clumped model, the high intensity temperature in the center of the sample is attributed to the higher concentration of fibers placed in this zone. However, for the random distribution, the distribution and magnitude of the E-field are more uniform across the surface.

In order to quantitatively evaluate the distribution of surface temperature, the surface of these two models was divided into 25 equal zones with dimensions of 25 × 25 mm. The greatest mean value of 0.4 was obtained in the center of the clumped fiber sample, and this value sharply decreases with distance from the center of sample. Further, the mean value of the temperature for sample with random distribution and clumped fiber are 0.20 and 0.14, respectively. However, the random distribution sample has a standard deviation for temperature difference of 0.06 compared to 0.12 for the clumped distribution sample, thus supporting the conclusion of a more uniform distribution of temperature difference for the random distribution sample.

It should be pointed out that open boundary conditions were employed for simulations which consider an infinite FRCM sample in the lateral direction (i.e., x and y directions as shown in Figure 5). As a result of the open boundary condition applied along the x- and y-axes, heat diffusion is the only mechanism of heat transfer in these directions. Additionally, the top and bottom of the SFRC sample (along the z-axis in Figure 5) is considered to be surrounded by an infinite half-space of air. Thus, both heat diffusion and heat convection take place in this direction. In order to address the boundary conditions at the two interfaces between FRCM and air, the heat transfer coefficient of h_C = 10 W/m^{2}K is considered [40].

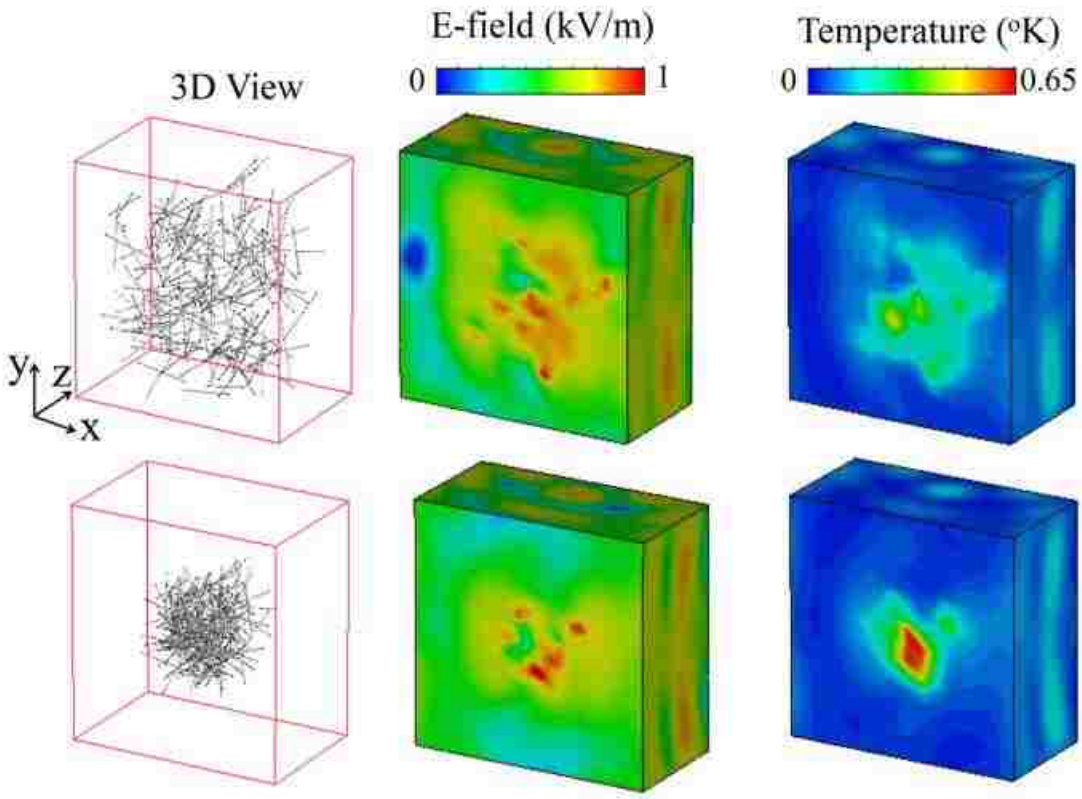

Figure 5 - Numerical modeling results of E-field and temperature variation for random (top row) and clumped (bottom row) fiber distributions

5. TEST RESULTS

5.1. FRESH AND MECHANICAL PROPERTIES OF FRCMS

Figure 6 shows the variation in flow consistency with fiber addition. As expected, the inclusion of fibers resulted in lower flow consistency. The increase in fiber from 1% to 3% resulted in 15% to 82% lower flow compared to the reference mixture. As shown in Figure 6, for the mixture containing 3% fiber, relatively high concentration of fibers can be observed at the center of the flow test, and a layer of water appeared on the outer edge of mixture at the end of the flow test, indicating a low level of stability.

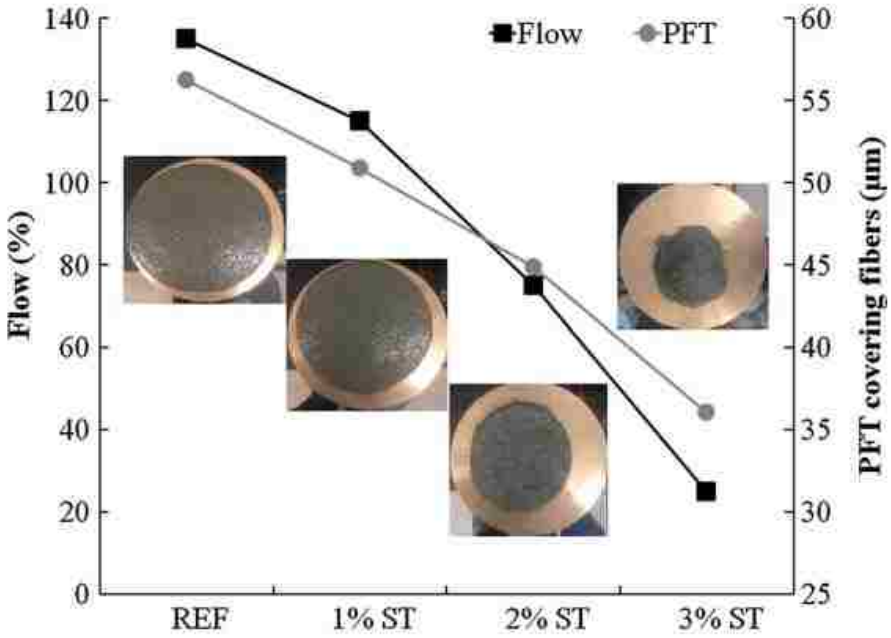

Figure 6 - Effect of fiber addition on flow and PFT covering fibers

The effect of fiber addition on PFT covering fibers is shown in Figure 6. An increase in the fiber content from 0 to 3% resulted in a 37% reduction in PFT around the fibers. The reduction in PFT around fibers contributes to lower flow consistency and higher interaction among fibers, thus leading to higher potential of fiber clumping. The addition of fibers from 0 to 3% decreased the packing density from 0.73 to 0.67. The increase in steel fiber from 0 to 2% led to merely 3% reduction in packing density,

whereas a further increase in fiber content from 2% to 3% resulted in an 8.5% decrease in packing density. This can be attributed to the fact that rigid fibers, such as steel fibers, can change the structure of the solid skeleton (i.e. aggregates) and push the particles apart, thus increasing the void volume among solid particles. Therefore, for a given paste volume, a decrease in packing density can lead to lower workability and lower thickness of the paste layer surrounding the fibers.

Figure 7 depicts the load-deflection responses of the FRCMs. As expected, the use of fibers resulted in higher peak strength and flexural toughness compared to the reference mixture. The mixture made with 2% steel fiber was shown to have the greatest peak strength and area under load-deflection curve compared to other FRCMs. The increase in fiber content from 2% to 3% led to 20% lower peak strength and 55% lower flexural toughness. In other words, the mixture containing the highest fiber content of 3% did not exhibit the greatest flexural toughness. This can be attributed to the fiber clumping, which can lead to lower efficiency of fibers to transfer stress, thus resulting in drop in mechanical performance. In addition, the entrapment of air bubbles between fiber clumps can weaken the interface between fibers and paste, thus reducing bond strength.

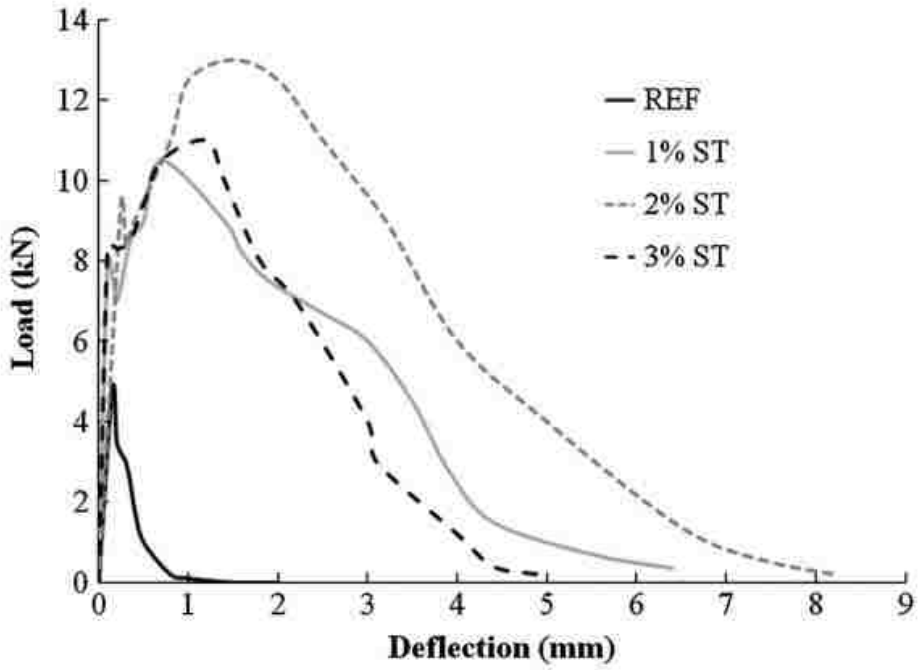

Figure 7 - Load-deflection curves of investigated FRCMs

5.2. AMT RESULTS

Surface temperature differences (ΔT) determined on one side of the investigated samples (1%, 2%, and 3% fiber contents) after 30 sec of microwave illumination at a frequency of 2.4 GHz are shown in Figure 8. For each sample, ten zones with dimensions of 25 × 25 mm were considered to quantitatively analyze the distribution of fibers. For a given sample side (i.e., side 1), samples made with 1% and 2% steel fibers exhibited a higher temperature difference across the surface compared to the sample containing 3% steel fibers. The high intensity spot in the temperature profile of the sample containing 3% fiber content can reflect the relatively high concentration of fibers (fiber clumping) in that zone. In addition, the relatively high quantity of blue zones observed for this sample represents zones without steel fibers.

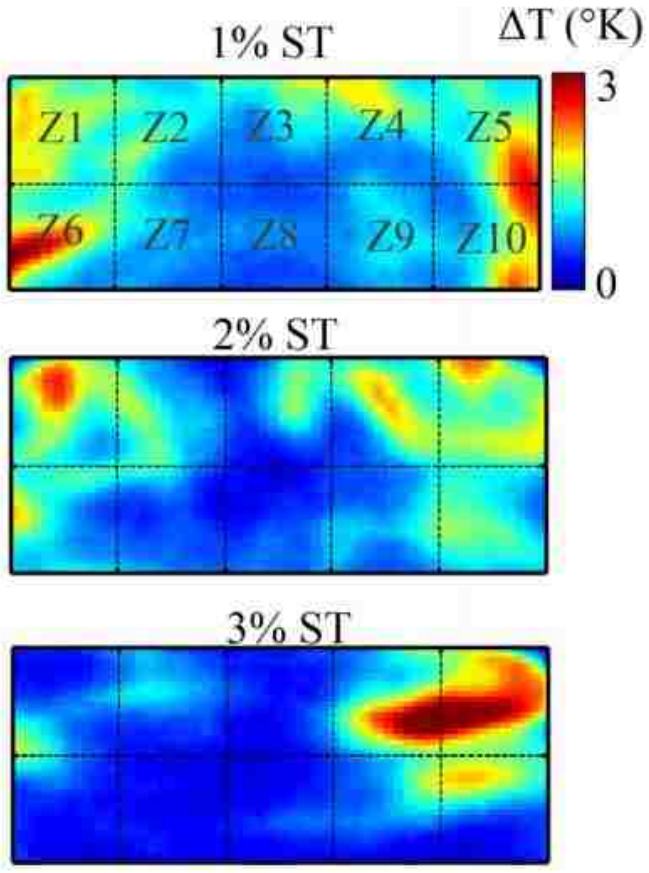

Figure 8 - Surface temperature variation of samples made with different fiber contents

The histogram of the mean of the temperature difference ($\mu_{total}(t)$) for all surfaces of samples made with 2% and 3% fibers is shown in Figure 9. The sample made with 3% fiber content resulted in the higher variation (density) in surface temperature, ranging from 0.1 to 2.5 °K. In addition, the majority of measured surface temperature in this sample lies within a narrow range between 0.2 to 0.4 °K, resulting in a narrow and steep histogram for this sample. Compared to the sample with 3% steel fiber, sample containing 2% fiber exhibited a more uniform distribution of measured surface temperature (indicative of a more uniform distribution of steel fibers), shown in Figure 9.

The mean of temperature difference for 120 sec (30 sec heating time plus 90 sec cooling time) for all three samples at operating frequency of 2.4 GHz is shown in Figure 10. It is expected that samples with higher fiber content will undergo a greater increase in surface temperature, as is observed for samples made with 1% and 2% fiber contents. However, this tendency is reversed with further fiber addition (from 2% to 3%). This behavior was observed for both the heating and cooling stages. Further, the decrease in surface temperature for the sample with 3% fiber content may be an indication of zones without fibers, in which the surface temperature is only affected by dielectric heating.

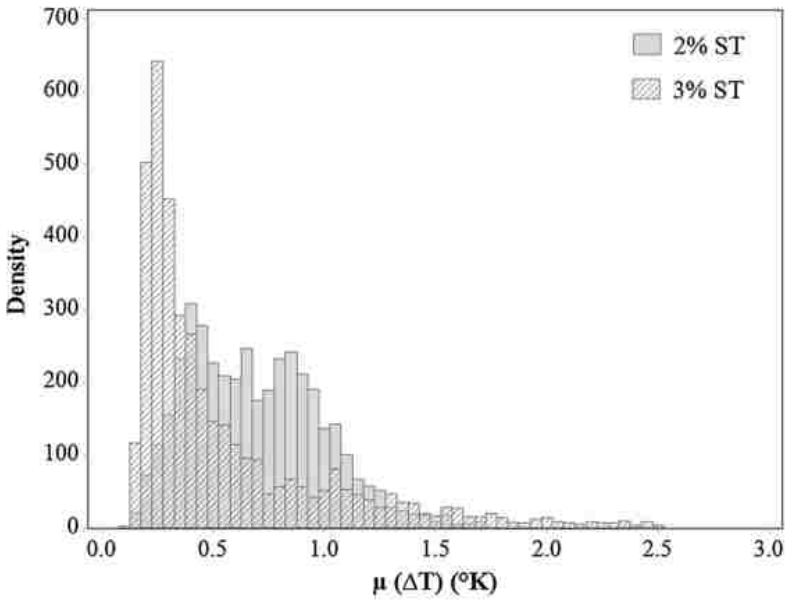

Figure 9 - Histograms of surface temperature for samples made with different fiber contents

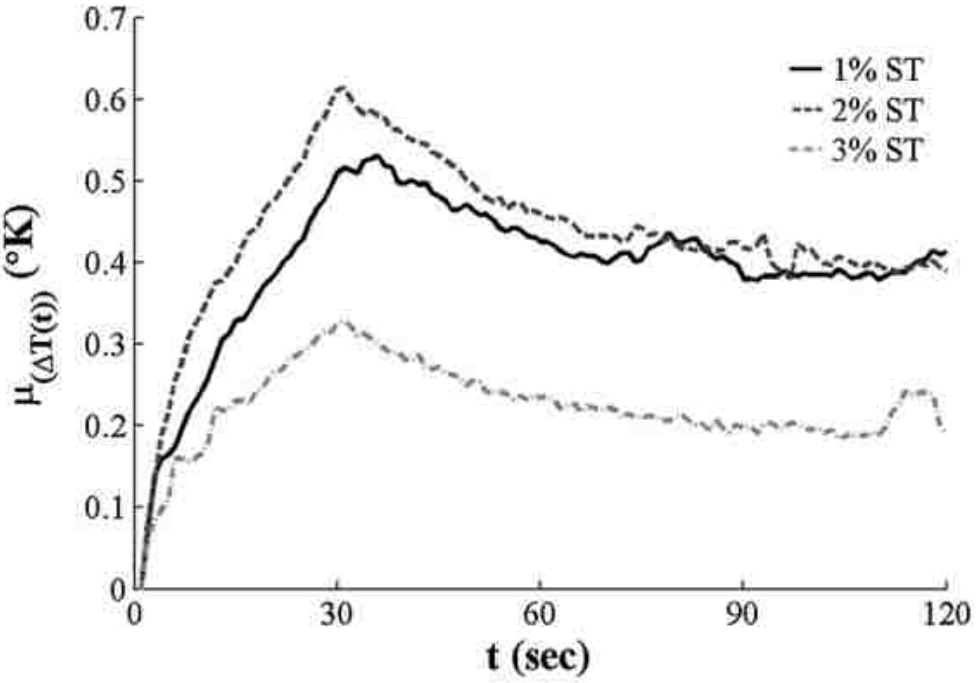

Figure 10 - Transient surface temperature of samples made with different fiber contents at operating frequency of 2.4 GHz

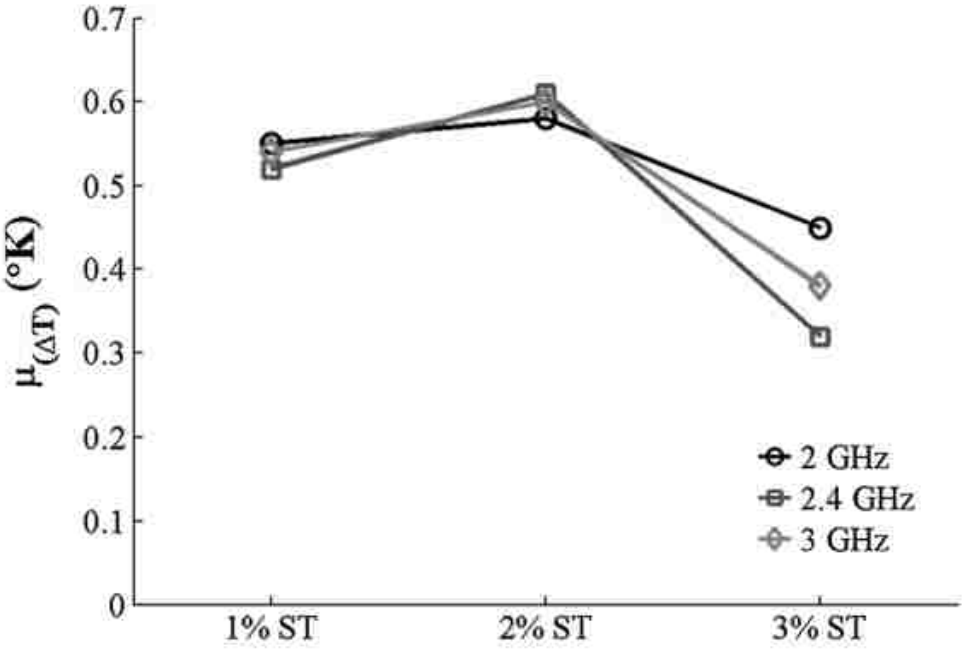

Figure 11 - Variation in mean value of surface temperature at different operating frequencies after 30 s heating

The variation in the mean value of the surface temperature as a function of fiber content at various operating frequencies is shown in Figure 11. Regardless of operating frequency, an increase in fiber content from 1% to 2% resulted in higher mean value of the surface temperature. On the other hand, for the sample made with 3% fiber content, significant decrease in the mean (from the 2% sample) occurred. This decrease is attributed to the non-uniform fiber distribution in the sample with 3% fiber content. These results are in agreement with those obtained from the simulated AMT results (Figure 5), in which for the sample with uniform fiber distribution, the temperature variation across the entire surface is more uniform than the temperature variation of the sample with non-uniform fiber distribution. As shown in Figure 11, it appears that the temperature difference between the sample with 3% fiber content and the samples with 1% and 2% fiber content is more substantial at 2.4 GHz. However, this difference is quite small (~<0.1 °K) and is attributed to measurement error.

The significance of variation (due to fiber content and sample side) in the mean value of surface temperature for different samples was statistically evaluated using the ANOVA test. The null hypothesis indicates that a variable has no significant influence on surface temperature, whereas the alternative hypothesis represents that the contribution of a given parameter to the surface temperature is statistically significant for a given level of significance. The level of significance is a probability threshold below which the null hypothesis is rejected. Commonly used values for the level of significance are 0.05 and 0.10 [41].

In this investigation, the probability (P-value) of 0.05 was considered as the level of significance. The results of the ANOVA test for the investigated parameters (fiber content and sample side) at frequency of 2.4 GHz are presented in Table 1. The results indicate that the fiber volume has a significant influence on the variation of the mean of surface temperature. It is interesting to note that the significance of measurements conducted on different sides of each sample is as a function of fiber content. In the case of samples made with 3% steel fibers, the investigated sample sides (surfaces) had a significant effect on the variation of the mean value of surface temperature (P-value << 0.05). However, for samples made with 1% and 2% steel fibers, the investigated sample side resulted in no significant influence on the mean value of surface temperature (P-

value > 0.05). This reflects that in the case of relatively uniform fiber distribution, the measurements have good repeatability, regardless of the sample side.

Table 1 - ANOVA results at 2.4 GHz

Response	Parameter	DOF	*P* value	Remark
Surface temperature	Fiber	2	0.0001	S
	Sample side			
	1 % ST	3	0.053	NS
	2 % ST	3	0.091	NS
	3 % ST	3	0.0001	S

DOF degree of freedom which is equal to $N - 1$ (N refers to the number of variables.), *NS* not significant, *S* significant

Figure 12 shows the variation in the mean of temperature difference across the surface (i.e., as a function of zones) for the three samples (see Eqs. (9) and (10)). Each sample is divided into 40 zones resulting from $N_z = 10$ and $N_s = 4$. The highest variation in the mean of surface temperature was found for the sample made with 3% fiber content, indicating non-uniform fiber distribution across different zones. Even with higher fiber content, the majority of zones of the sample containing 3% fibers exhibited lower temperature difference compared to the other two samples. This may indicate that for the sample with 3% fiber content, most of the fibers are located away from the surface of sample, thus leading to a lower temperature difference. This can be attributed to the potential of clumping of fibers in this sample. Samples made with 1% and 2% fiber contents exhibited a similar mean of temperature difference. This may be due to the similar fiber distribution of these samples.

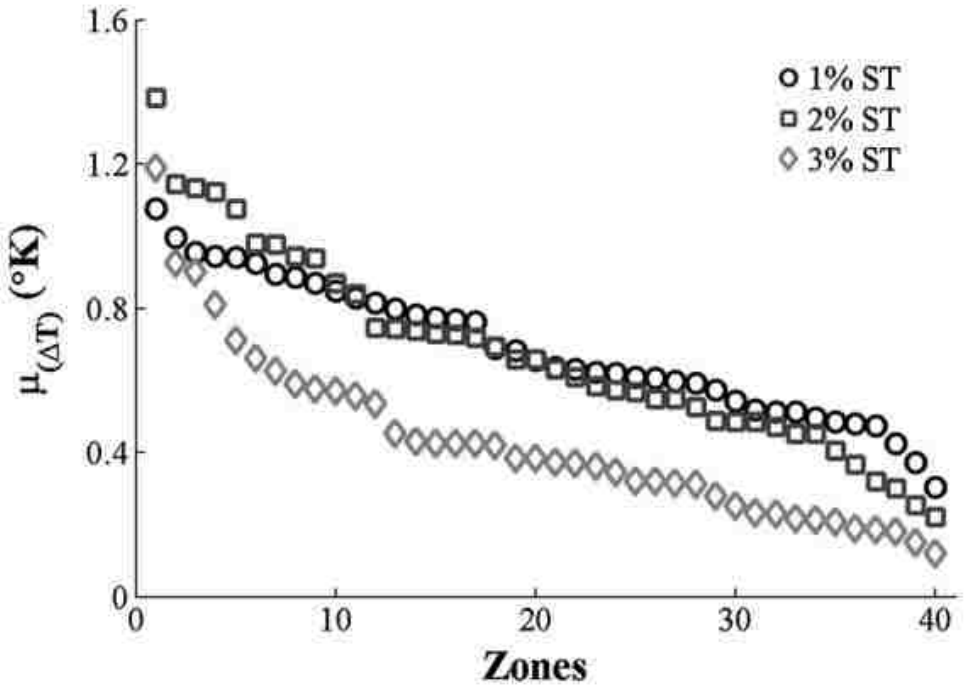

Figure 12 - Variation in mean value of surface temperature for 40 zones across each sample after 30 s heating

Figure 13 shows the correlation between the mean of surface temperature and the fiber density for both numerical modeling and measurement. Due to the extensive computation time and mesh cell density, numerical modeling could not be conducted on a sample similar to those measured. Rather, a fiber density of 0.5% was considered to keep the computational domain manageable (random fiber distribution in Figure 5). In order to validate the numerical modeling, the results of simulation (sample modeled with 0.5% steel fibers) and measurement (sample with 2% steel fibers) were compared as a function of fiber density. In all cases (simulation and measurement), there are no fibers present on the surface of the samples. Therefore, the fiber density (simulation and measurement), expressed as the number of fibers located within a sample zone, was determined at a depth of 10 mm (for the 2% sample, 10 mm of sample material was cut/removed from all four sides of the sample). The 25 zones were considered for the simulated sample, and 40 zones were considered for the (measured) 2% fiber sample. All zones had dimensions of 25 × 25 mm (similar to the zones discussed in Section 4.2 and 5.2). Subsequently, the

fiber density was related to the mean surface temperature of each zone, as is shown in Figure 13. As seen, a linear trend for simulation and measurement was observed between the mean of surface temperature and fiber density. An extension of the fitted trend line of the measured data agrees well with the trend line obtained for numerical modeling (shown in Figure 13), thus ensuring that the results of numerical modeling match well with measurements.

Correlation between mean of surface temperature difference (corresponding to 40 zones) and normalized toughness of hardened samples with fiber homogeneity determined from cast prism in fresh state (*IHI*) is shown in Figure 14. As discussed above, higher *IHI* (see Eq. (8)) reflects higher variation (i.e., lower homogeneity) in fiber content throughout the cast prism. The effectiveness of incorporating fibers to enhance flexural toughness is shown to be significantly affected by the level of fiber homogeneity along the cast prism. A higher *IHI* value of 15% for mixture made with 3% fiber content resulted in 55% lower flexural toughness compared to the mixture containing 2% fiber. A lower fiber homogeneity and fiber clumping observed in this mixture led to lowering the reinforcing efficiency of fibers to enhance mechanical properties. Similar trend was observed for mean of surface temperature difference of FRCMs, as indicated in Figure 14. Samples with lower *IHI* values (i.e. higher level of fiber homogeneity) were found to have a higher mean temperature difference. This is due to the increased (more uniform) level of fiber distribution for samples made with 1% and 2% steel fibers. On the other hand, the reduced level of fiber homogeneity in the sample with 3% steel fiber contributed to a lower mean of temperature difference.

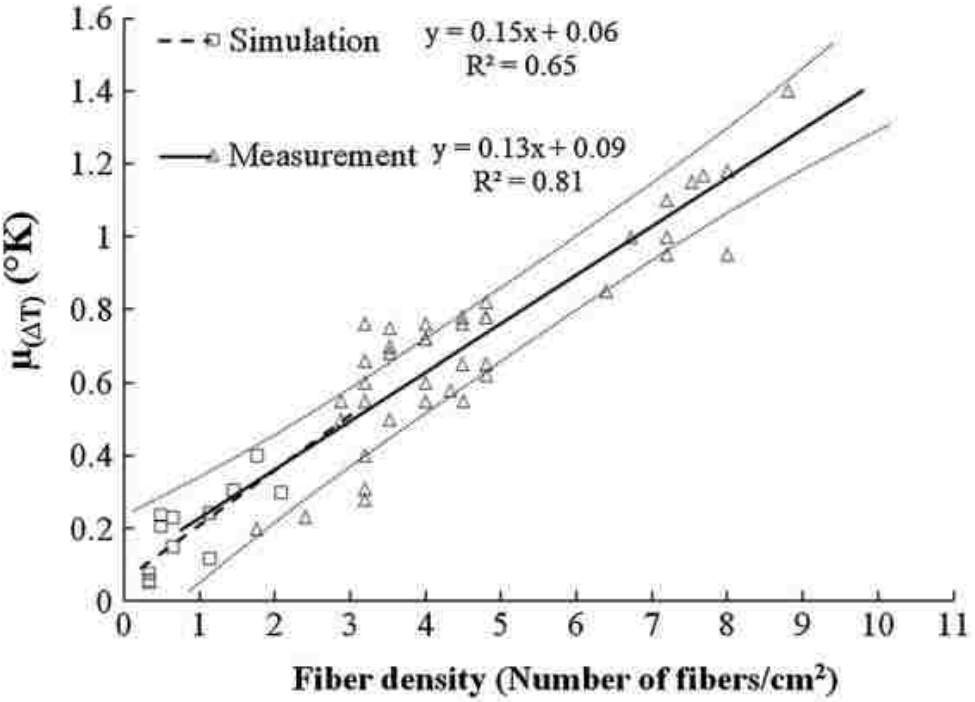

Figure 13 - Correlation between fiber density and mean of surface temperature for both simulations and measurements

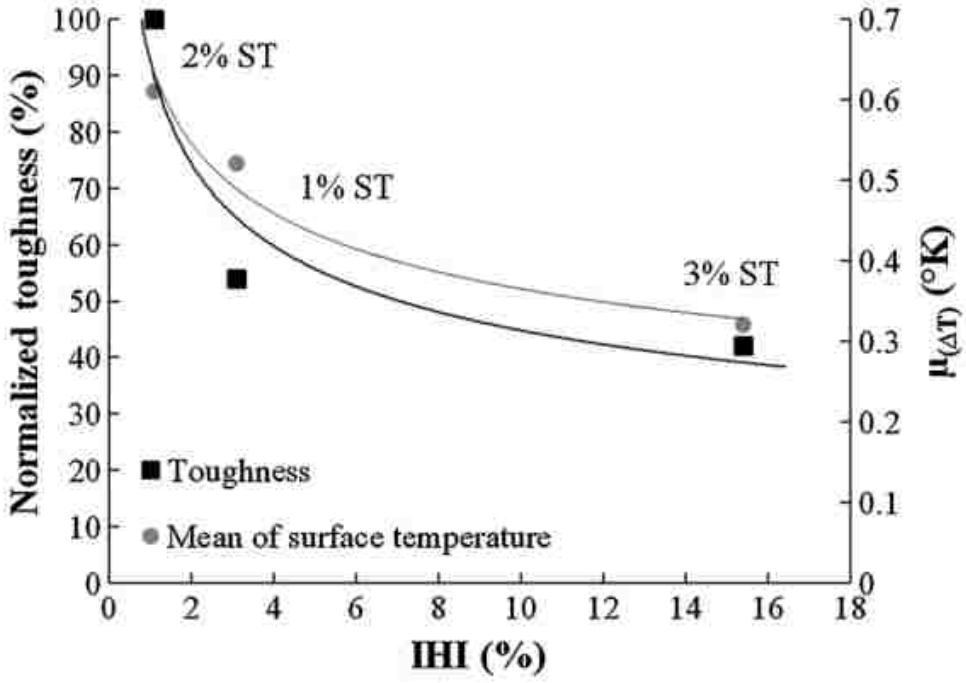

Figure 14 - Correlation between surface temperature and normalized toughness of hardened samples with fiber homogeneity determined from freshly cast prism

6. CONCLUSIONS

Active microwave thermography (AMT) was utilized to characterize the content and distribution of steel fibers in fiber-reinforced cement-based mortars (FRCMs). Full-wave coupled electromagnetic-thermal numerical modeling was also conducted to assess the effect of dielectric properties, fiber depth, and clumping of fibers on the surface thermal profile. The flexural toughness and level of fiber homogeneity along the freshly cast prisms were evaluated. Based on the test results reported herein, the following conclusions can be made:

The AMT simulation results indicated that fiber depth and dielectric properties of mortar have significant influence on temperature difference at the surface of sample, due to variation in heating associated with induced surface current and dielectric heating. The sample with random fiber distribution had lower standard deviation for temperature difference compared to the clumped distribution sample. This is attributed to the more uniform distribution of temperature difference for this sample. Based on the AMT measurement results, FRCMs containing 1% and 2% steel fibers are shown to have higher surface temperature difference compared to the sample made with 3% fiber content. This is due to the non-uniform distribution and possible fiber clumping. The high and low intensity spots in the temperature profile of the sample containing 3% steel fiber can be an indication of relatively high and low concentrations of fibers, respectively, in corresponding zones. Regardless of sample side, the AMT measurements exhibited good repeatability for the four sample sides for FRCMs made with 1% and 2% fiber contents, thus indicating uniform fiber distribution. However, for sample with 3% fiber, the sample side was found to have significant influence on surface temperature. The effectiveness of fibers to enhance flexural toughness is influenced by fiber distribution, as indicated by the freshly cast prism test. The fiber clumping and lower level of fiber homogeneity for FRCM made with 3% steel fiber resulted in 55% lower flexural toughness compared to the FRCM containing 2% fiber. The relationship between mean temperature difference of hardened samples and level of fiber homogeneity determined from freshly cast prism shows that FRCMs with higher level of fiber homogeneity (i.e. lower *IHI*) along the cast prism resulted in higher mean temperature difference determined for four sides of the test samples.

REFERENCES

[1] L. Ferrara, Park YD, Shah SP, "A method for mixdesign of fiber-reinforced self-compacting concrete," Cem Concr Res 37(6):957–971, 2007.

[2] Grunewald S, Walraven JC, "Parameter-study on the influence of steel fibers and coarse aggregate content on the fresh properties of self-compacting concrete," Cem Concr Res 31(12):1793–1798, 2001.

[3] Khayat KH, Kassimi F, Ghoddousi P, "Mixture design and testing of fiber-reinforced self–consolidating concrete," ACI Mater J 111(2):143–152, 2014.

[4] Khayat KH, Roussel Y, "Testing and performance of fiber-reinforced, self-consolidating concrete," Mater Struct 33(6):391–397, 2000.

[5] Rossi P, "Mechanical behaviour of metal-fibre reinforced concretes," Cem Concr Compos 14(1):3–16, 1992.

[6] Akcay B, Tasdemir MA, "Mechanical behaviour and fibre dispersion of hybrid steel fibre reinforced self-compacting concrete," Constr Build Mater 28(1):287–293, 2012.

[7] Di Prisco M, Dozio D, Belletti B, "On the fracture behaviour of thin-walled SFRC roof elements," Mater Struct 46(5):803–829, 2013.

[8] Emdadi A, Mehdipour I, Libre NA, Shekarchi M, "Optimized workability and mechanical properties of FRCM by using fiber factor approach: theoretical and experimental study," Mater Struct 48(4):1149–1161, 2015.

[9] Ferrara L, Meda A, "Relationships between fibre distribution, workability and the mechanical properties of SFRC applied to precast roof elements," Mater Struct 39(4):411–420, 2006.

[10] Ferrara L, Park YD, Shah SP, "Correlation among fresh state behavior, fiber dispersion, and toughness properties of sfrcs," J Mater Civ Eng 20(7):493–501, 2008.

[11] Gettu R, Gardner DR, Saldivar H, Barragan BE, "Study of the distribution and orientation of fibers in SFRC specimens," Mater Struct 38(1):31–37, 2005.

[12] Kang ST, Lee BY, Kim JK, Kim YY, "The effect of fibre distribution characteristics on the flexural strength of steel fibre-reinforced ultra high strength concrete," Constr Build Mater 25(5):2450–2457, 2011.

[13] Martinie L, Rossi P, Roussel N, "Rheology of fiber reinforced cementitious materials: classification and prediction," Cem Concr Res 40(2):226–234, 2010.

[14] Mehdipour I, Vahdani M, Libre NA, Shekarchi M, "Relationship between workability and mechanical properties of fibre-reinforced self-consolidating mortar," Mag Concr Res 65(17):1011–1022, 2013.

[15] Ozyurt N, Mason TO, Shah SP, "Correlation of fiber dispersion, rheology and mechanical performance of FRCs," Cement Concr Compos 29(2):70–79, 2007.

[16] Ferrara L, Ozyurt N, Di Prisco M, "High mechanical performance of fibre reinforced cementitious composites: the role of ''casting-flow induced'' fibre orientation," Mater Struct 44(1):109–128, 2011.

[17] Zhou J, Qian S, Ye G, Copuroglu O, van Breugel K, Li VC, "Improved fiber distribution and mechanical properties of engineered cementitious composites by adjusting the mixing sequence," Cem Concr Compos 34(3):342–348, 2012.

[18] Torrijos MC, Barraga´n BE, Zerbino RL, "Placing conditions, mesostructural characteristics and post-cracking response of fibre reinforced self-compacting concretes," Constr Build Mater 24(6):1078–1085, 2010.

[19] Barnett SJ, Lataste JF, Parry T, Millard SG, Soutsos MN, "Assessment of fibre orientation in ultra high performance fibre reinforced concrete and its effect on flexural strength," Mater Struct 43(7):1009–1023, 2010.

[20] Bordelon AC, Roesler JR, "Spatial distribution of synthetic fibers in concrete with X-ray computed tomography," Cem Concr Compos 53:35–43, 2014.

[21] Ponikiewski T, Katzer J, "X-ray computed tomography of fibre reinforced self-compacting concrete as a tool of assessing its flexural behavior," Mater Struct 1–10. doi:10. 1617/s11527-015-0638-y, 2015

[22] Chermant JL, Chermant L, Coster M, Dequiedt AS, Redon C, "Some fields of applications of automatic image analysis in civil engineering," Cem Concr Compos 23(2):157–169 5064 Materials and Structures (2016) 49:5051–5065, 2001.

[23] Lataste JF, Behloul M, Breysse D, "Characterisation of fibres distribution in a steel fibre reinforced concrete with electrical resistivity measurements," NDT E Int 41(8):638–647, 2008.

[24] Ozyurt N, Mason TO, Shah SP, "Non-destructive monitoring of fiber orientation using AC-IS: an industrial scale application," Cem Concr Res 36(9):1653–1660, 2006.

[25] Reinhardt HW, Grosse CU, Weiler B, "Material characterization of steel fiber reinforced concrete using neutron CT, ultrasound and quantitative acoustic emission techniques," NDT. net. 6(5):1–2, 2001.

[26] Ferrara L, Faifer M, Toscani S, "A magnetic method for non destructive monitoring of fiber dispersion and orientation in steel fiber reinforced cementitious composites— part 1: method calibration," Mater Struct 45(4):575–589, 2012.

[27] Orbe A, Cuadrado J, Losada R, Roj E, "Framework for the design and analysis of steel fiber reinforced self compacting concrete structures," Constr Build Mater 35:676–686, 2012.

[28] Orbe A, Roj E, Losada R, Cuadrado J, “Calibration patterns for predicting residual strengths of steel fibre reinforced concrete (SFRC),” Compos B Eng 58:408–417, 2014.

[29] Jamil M, Hassan MK, Al-Mattarneh HM, Zain MF, “Concrete dielectric properties investigation using microwave nondestructive techniques,” Mater Struct 46(1–2):77–87, 2013.

[30] Zoughi R, “Microwave non-destructive testing and evaluation principles. Springer Science & Business Media, New York, 2000.

[31] Maldague X, Marinetti S, “Pulse phase infrared thermography,” J Appl Phys 79(5):2694–2698, 1996.

[32] Meola C, Carlomagno GM, “Recent advances in the use of infrared thermography,” Meas Sci Technol 15(9):27–58, 2004.

[33] Valluzzi MR, Grinzato E, Pellegrino C, Modena C, “IR thermography for interface analysis of FRP laminates externally bonded to RC beams,” Mater Struct 42(1):25–34, 2009.

[34] Foudazi A, Donnell KM, Ghasr MT, “Application of active microwave thermography to delamination detection,” In: 2014 IEEE International proceedings on instrumentation and measurement technology conference (I2MTC), pp 1567–1571, 2014.

[35] Foudazi A, Ghasr MT, Donnell KM, “Application of active microwave thermography to inspection of carbon fiber reinforced composites,” In Proc. IEEE AUTOTESTCON, pp 318–322, 2014.

[36] Foudazi A, Ghasr MT, Donnell KM, “Characterization of corroded reinforced steel bars by active microwave thermography,” IEEE Trans Instrum Meas 64(9):2583–2585, 2015.

[37] Foudazi A, Mehdipour I, Donnell KM, Khayat KH, “Detection of steel fibers in cementbased materials by active microwave thermography,” In: 14th international symposium on nondestructive characterization of materials (NDCM2015), pp 22–26, 2015.

[38] Bois KJ, Benally AD, Zoughi R, “Microwave near- field reflection property analysis of concrete for material content determination,” IEEE Trans Instrum Meas 49(1):49–55, 2000.

[39] Balanis CA, “Antenna theory: analysis and design,” 2nd edn. Wiley, New York, pp 69–73, 1997.

[40] Lee Y, Choi MS, Yi ST, Kim JK, “Experimental study on the convective heat transfer coefficient of early-age concrete,” Cem Concr Compos 31(1):60–71, 2009.

[41] Montgomery DC, “Design and analysis of experiments: response surface method and designs,” Wiley, Hoboken, 2005.

IV. CHARACTERIZATION OF CORRODED REINFORCED STEEL BARS BY ACTIVE MICROWAVE THERMOGRAPHY

ABSTRACT

Detection and characterization of corrosion on steel is important in the transportation and infrastructure industries. Many nondestructive testing (NDT) methods have been applied to this inspection need including microwave and thermography. In order to overcome existing limitations of traditional NDT methods, integrated NDT techniques have also been developed. To this end, the integration of microwave and thermography, herein referred to as Active Microwave Thermography (AMT), is proposed as a potential NDT tool for detection of corroded steel bars. This method utilizes microwave energy to heat a structure of interest. Subsequently, a thermal camera is used to monitor the thermal surface profile. This paper presents preliminary simulations and measurements of AMT as a potential method for corrosion detection and characterization.

Index Terms—microwave nondestructive testing; thermography; active microwave thermography, corrosion; reinforcing steel bars (rebar); dielectric heating

1. INTRODUCTION

Corrosion in infrastructure in the form of corrosion under paint in steel bridges, corrosion of reinforcing steel bars (rebar) in concrete decks and other types of steel-based structures can cause structural failure [1]. Various nondestructive testing (NDT) methods including microwave [2]-[4], thermography [5], etc. have been proposed for continued maintenance and safety in the transportation industry. Among these methods, active thermography is a well-established and fast inspection tool with benefits including the availability of non-contact and high sensitivity infrared (thermal) cameras. Although active thermography takes advantage of external heat sources (typically powerful heat lamps), it also carries the risk of subsequent heat damage. Thus, to build upon the success and legacy of thermography and improve the method as an NDT tool, other NDT methods have been integrated with thermography including ultrasound [6] and eddy current [7]. As proposed in [8]-[10], the combination of microwaves (as the heat source) and thermography (for subsequent monitoring), herein referred to as Active Microwave Thermography (AMT), is an integrated NDT method which offers unique advantages for health monitoring of infrastructure such as localized heating, rapid inspection time, etc..

In general, there are two mechanisms of heating that are possible with AMT. First, (direct) dielectric heating may take place. Dielectric materials are defined by their relative (to freespace) complex dielectric properties, given as $\varepsilon_r = \varepsilon_r' - j\varepsilon_r''$. The real part (permittivity) represents the ability of the material to store microwave energy, while the imaginary part (loss factor) represents the ability of the material to absorb microwave energy. Generally, dielectric heating is quantified by the specific absorption rate (SAR) of the dielectric material which is defined as the amount of microwave energy absorbed by a given volume of dielectric material when exposed to a radiating device [11]. Another heating mechanism may occur if conductive materials are present in the structure under inspection. Microwaves cannot penetrate through conductive materials, but current will be induced on the surface of such materials when irradiated by microwave energy. Thus, these currents will also act as a (secondary) source of heat. Hence, since rebar is conductive and if corrosion (a lossy dielectric) is present, both mechanisms of heating under microwave illumination will take place. Thus, AMT may have potential for detection and characterization of corrosion on steel-based structures. As such, this paper

presents preliminary simulation and measurement results for the use of AMT in characterization of corroded steel rebar.

2. SIMULATIONS

For simplicity of simulations, a smooth (no ribs) rebar is considered located in air with a radius of r = 4.8 mm containing 1 cm corrosion (ε_r = 10 – j2 [12]) along the length of the rebar. The percentage of corrosion, C, is defined by $C = t/2r$ where t is the thickness of the corrosion. As shown in [10], once corrosion occurs, it not only builds on the surface, but also penetrates the volume of the object. This is illustrated in Figure 1, where the cross-sections of rebar without (Figure 1a) and with (Figure 1b) corrosion are presented.

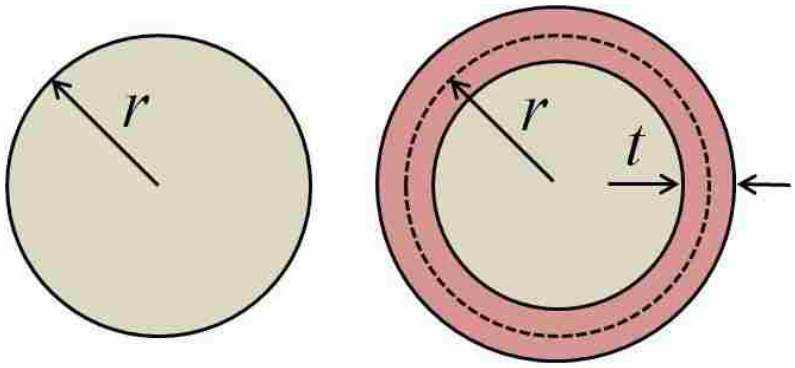

(a) (b)

Figure 1 - Rebar cross-section (a) un-corroded, and (b) corroded

A coupled microwave-thermal co-simulation was conducted using CST Microwave Studio® and MPHYSICS Studio® [13]. The simulation is conducted in two parts; first, the electromagnetic response (i.e., electric and magnetic field inside the dielectric material and induced current on the conducting surface) is determined. Then,

the transient thermal response is calculated (i.e., heat generation and diffusion) based on the electromagnetic response. The transient response contains two parts: first, the amount of time that microwave energy is applied (i.e., the heating period), and second, after the microwave energy is removed (i.e., the cooling period).

In Table 1, the thermal properties of steel, corrosion, air and adhesive (used later for measurements) are provided. As shown, the thermal conductivity of steel is much higher than that of air and corrosion. This is important for this application of AMT, since it is expected that during illumination of microwave energy, the temperature of the corroded area will be higher than that of the uncorroded area due to the lower thermal conductivity. Furthermore, during cooling, the corroded area cools more slowly until thermal equilibrium is reached. Thus, the corrosion will be indicated as a hot spot on the thermal image during both heating and cooling steps.

Table 1 - Thermal Properties of Materials

Material	**Density (Kg/m^3)**	**Thermal Conductivity (W/m.K)**	**Specific Heat (KJ/Kg.K)**	**Diffusivity 10^{-6} m^2/s**
Air	1.204	0.026	1.005	21.5
Steel 1008	7870	59.5	0.48	15.75
Corrosion	5242	0.6	0.65	0.17
Adhesive	1100	~ 0.1 – 2	3.7	~ 0.02 – 0.5

Initially, the effect of corrosion percentage, *C*, on the thermal response of the corroded rebar is studied. The rebar is illuminated with 50 W of microwave energy with parallel (to the orientation of the rebar) polarization. This microwave energy was applied to the rebar for 10 sec (e.g., a short heating time). The thermal profile was monitored

throughout heating and continued during cooling. While the definition of SAR is based on absorption of microwave energy in dielectric materials, this absorption is also related to temperature change. Thus, the indication of corrosion should manifest itself similarly in both SAR and normalized temperature.

In order to investigate the effect of various amounts of corrosion at a specific frequency, the thermal response for cases of C = 20, 30 and 40% at 2.5 GHz are studied. In Figure 2, the maximum temperature at the surface of the corroded area is shown. It is shown that a higher percentage of corrosion leads to a faster temperature rise during the heating period.

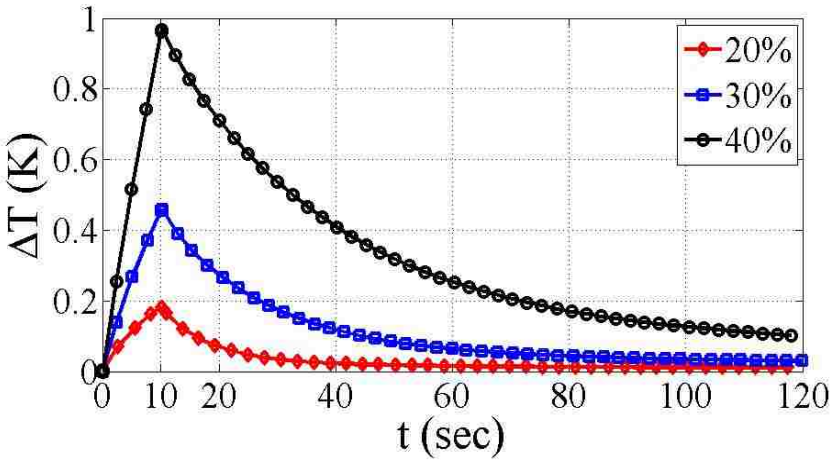

Figure 2 - Transient behavior of the corroded area of rebar at 2.5 GHz

Figure 3 shows the temperature rise as a function of frequency and corrosion percentage. In Figure 3a, the normalized temperature (with respect to ambient) immediately after 10 sec of microwave illumination is shown, along with the SAR for C = 10 to 60% at 2.5 GHz. It can be seen that as the corrosion thickness (i.e., higher t or C) increases, the SAR value also increases as a result of the larger volume of lossy material (since SAR is proportional to ε_r''). As such (and is also shown in Figure 3a), the normalized temperature also increases with C. Further, after C = 10%, the normalized

temperature is greater than 0.05 °K, indicating that the corroded area can be detected with a reasonably-priced and commercially available thermal camera (typical sensitivity of 0.05 °K [14]). However, more sensitive (but more expensive) cameras (e.g., around 0.01 °K) may be used to detect corrosion with *C* less than 10% (i.e., light corrosion on rebar). In Figure 3b, the normalized temperature (with respect to ambient) immediately after 10 sec of microwave illumination is shown, along with the SAR at *C* = 40% for frequency of 1.5 to 3 GHz. As seen, higher frequency leads to a higher SAR value and therefore higher normalized temperature. Lastly and as mentioned previously, it is evident in Figure 3a and Figure 3b that SAR and normalized temperature have the same behavior with respect to the corrosion ratio as well as frequency of operation.

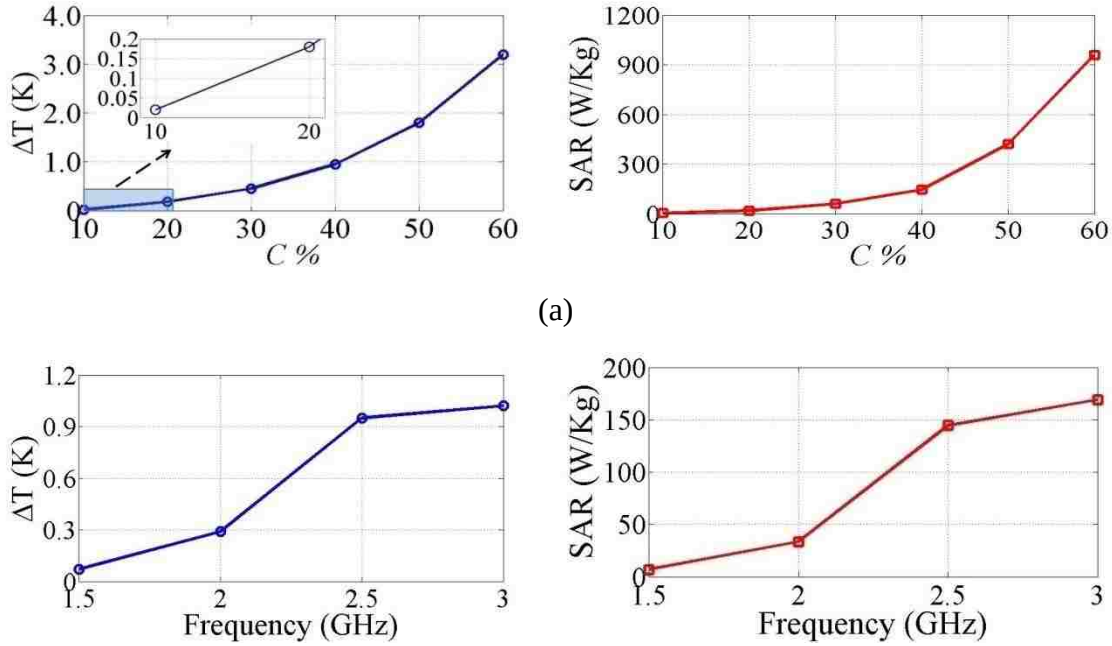

Figure 3 - Effect of (a) corrosion thickness, and (b) frequncy, on normalized temperature of corrosion at t = 10 sec (left), and maximum SAR (right)

3. MEASUREMENT RESULTS

Preliminary measurements were also performed to support this potential application of AMT. To do this, an AMT system, capable of transmitting 50 W of electromagnetic energy at 2 - 3 GHz, has been designed. Measurements were conducted using this system on a rebar, as illustrated in Figure 4. As shown, the rebar contained four small sections of heavy corrosion (i.e., heavily corroded pieces of thin steel) glued on top of a lightly-corroded rebar, referred to as C1 to C4. Since adhesive (glue) has similar thermal properties (thermal conductivity and diffusivity, see Table I) to corrosion, a similar thermal response to the corrosion may result, meaning the influence of the adhesive is expected to be minimal. A TEM horn antenna was used to transmit the microwave signal. The irradiating energy was polarized parallel with respect to the rebar with 1 cm liftoff (the distance between the antenna and the rebar). A thermal camera (DRS Tamarisk 320 [14]) with sensitivity of 0.05 °K was used to monitor the thermal profile of the rebar. Similar to the simulations, rebar was illuminated by 50 W of electromagnetic energy for 10 sec. Also, each experiment was repeated six times.

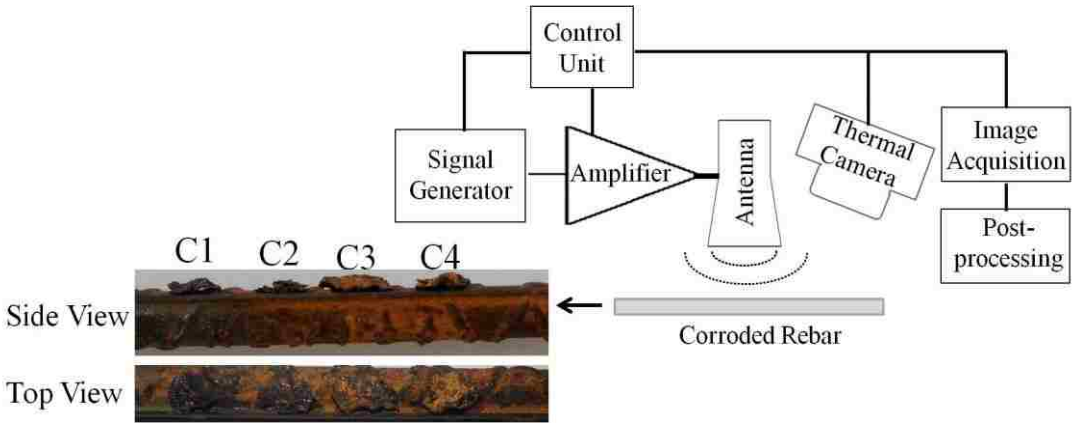

Figure 4 - AMT measurement set-up for corroded rebar (side and top view)

In Figure 5, the surface thermal profile after 10 sec of heating is illustrated for 2, 2.5 and 3 GHz. By averaging the results for each experiment, variation in results due to fluctuation in ambient temperature may be reduced. As seen, the corroded areas are visible as hot spots. Due to high thermal conductivity of steel, heat will dissipate quickly on un-corroded areas. Therefore, while the rest of the rebar has a slightly higher temperature than the background, this may be a result of the light corrosion on its' surface. Moreover, comparing different frequencies shows that a higher frequency leads to a higher temperature, as expected and mentioned above. Furthermore, the temperature difference between the corroded areas indicates different amounts of microwave energy absorption and hence different amounts of corrosion.

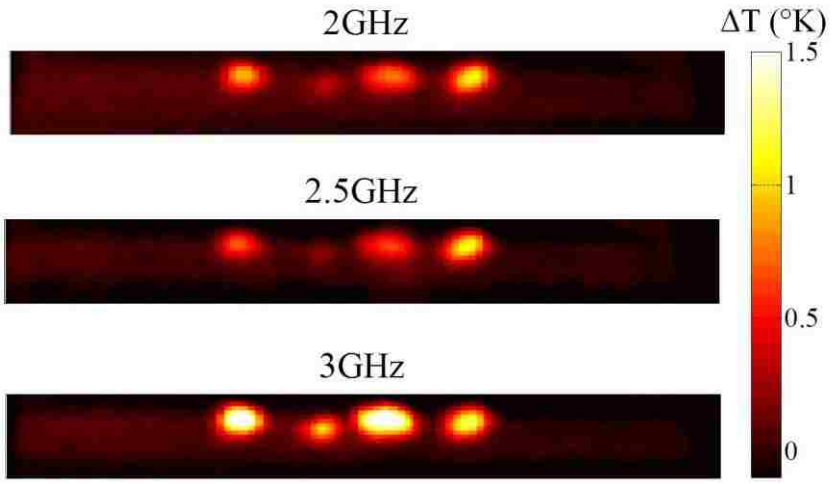

Figure 5 - Temperature profile of corroded rebar after 10 sec heating (C1, left, and C4, right)

To investigate the transient thermal behavior of corroded areas, the temperature of corroded areas C2 and C4 (during heating and cooling) are considered and shown in Figure 6. As seen in Figure 6a, C4 has a higher temperature than C2 (due to its higher value of *C*). It can also be seen that during the heating period, the normalized temperature has a smaller standard deviation than during the cooling period. This may be due to

applying controlled heat energy at a rate which is much higher than the loss of energy to the environment. Also, Figure 6b shows that higher frequencies lead to higher temperature differences during the heating period.

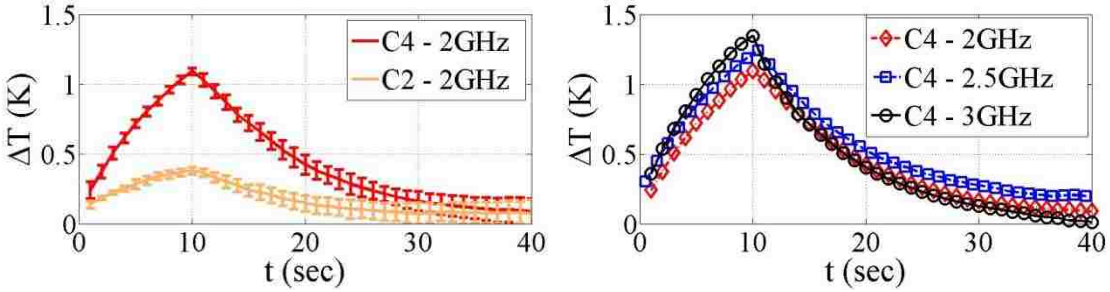

(b) (b)

Figure 6 - Measured results of (a) C2 and C4 at 2 GHz, and (b) C4 at frequenciey of 2, 2.5 and 3 GHz

4. CONCLUSION

Active Microwave Thermography is an integrated NDT method which takes advantage of unique aspects of microwave and thermographic NDT. This paper presented a preliminary simulation and measurement study on the capability of AMT to detect and characterize the presence of corrosion on corroded rebar with different percentages of corrosion and frequencies of operation. It is shown that a higher percentage of corrosion leads to increased absorption of microwave energy as well as a greater temperature difference. Moreover, increasing frequency leads to a greater temperature difference as well. Good agreement was shown between simulation and measurement results, indicating that AMT has potential to serve as a detection and characterization tool for corroded rebar.

REFERENCES

[1] J. G. Cabrera, "Deterioration of concrete due to reinforcement steel corrosion", Cement and concrete composites, vol. 18, no. 1, pp. 47-59, 1996.

[2] R. Zoughi, "Microwave non-destructive testing and evaluation principles," vol. 4. Springer, 2000.

[3] M. Fallahpour, J. Case, M. Ghasr, and R. Zoughi, "Piecewise and Wiener filter-based SAR techniques for monostatic microwave imaging of layered structures." IEEE Trans. on Instrumentation and Measurement, vol. 62, no. 1 pp. 282-294, 2014.

[4] M. Fallahpour, and R. Zoughi. "Sensitivity analysis of Wiener filter-based synthetic aperture radar (SAR) microwave imaging technique." IEEE I2MTC Proceedings, pp. 1212-1215, 2014.

[5] X. Maldague, and S. Marinetti. "Pulse phase infrared thermography", Journal of Applied Physics, vol. 79, no. 5, pp. 2694-2698, 1996.

[6] I. Solodov and G. Busse, "Resonance ultrasonic thermography: Highly efficient contact and air-coupled remote modes," Applied Physics Letters, vol. 102 (6), 2013.

[7] L. Cheng, and G. Y. Tian, "Transient thermal behavior of eddy-current pulsed thermography for nondestructive evaluation of composites," IEEE Trans. on Instrumentation and Measurement, vol. 62, no. 5 pp. 1215-1222, 2013.

[8] A. Foudazi, K. M. Donnell, and M. T. Ghasr, "Application of active microwave thermography to delamination detection", IEEE I2MTC Proceedings, pp. 1567-1571, 2014.

[9] A. Foudazi, M. T. Ghasr, and K. M. Donnell, "Application of active microwave thermography to inspection of carbon fiber reinforced composites", IEEE Autotest 2014, Sep. 2014.

[10] D. Pieper, K. M. Donnell, M. T. Ghasr, and E. C. Kinzel, "Integration of microwave and thermographic NDT methods for corrosion detection", 40th Annual Review Of Progress In Quantitative Nondestructive Evaluation, vol. 1581, no. 1, pp. 1560-1567, 2014.

[11] F. Gustrau, and A. Bahr, "W-band investigation of material parameters, SAR distribution, and thermal response in human tissue." IEEE Trans.on Microwave Theory and Tech., vol. 50, no. 10, pp. 2393-2400, 2002.

[12] N. Qaddoumi, L. Handjojo, T. Bigelow, J. Easter, A. Bray, and R. Zoughi, "Microwave corrosion detection using open ended rectangular waveguide sensors", Materials Evaluation, vol. 58, no. 2, pp. 178-184, 2000.

[13] CST - Computer Simulation Technology, http://www.cst.com

[14] DRS Thermal Camera, http://www.drsinfrared.com

V. ACTIVE MICROWAVE THERMOGRAPHY FOR NONDESTRUCTIVE EVALUATION OF SURFACE CRACKS IN METAL STRUCTURES

ABSTRACT

Detection of covered surface cracks in metal structures is an important issue in numerous industries. Various nondestructive testing and evaluation (NDT&E) techniques have been applied for this goal with varying levels of success. Recently, a technique based on the integration of microwave and thermographic NDT, herein referred to as Active Microwave Thermography (AMT), has been considered for various applications. In AMT, electromagnetic energy is utilized for the thermal excitation, and the subsequent surface thermal profile of the structure/material under test is measured with a thermal camera. Utilizing electromagnetic energy allows the inspection to be tailored to the application through choice of frequency, polarization, and power level. It is shown that for metal with a dielectric-filled crack irradiated with an electric field polarized perpendicular to the crack length, a propagating mode (TE_{10}) is generated inside the crack, which can cause dielectric heating to occur in the (filled) crack. In particular, the crack can be detected via an AMT inspection as long as the angle between the crack length and incident electric field is between 0° (perpendicular polarization) and ~65°. In addition, from the measured thermal contrast (*TC*) and signal-to-noise ratio (*SNR*), the optimum heating time is ~5-30 sec for successful inspection.

Index terms—active microwave thermography; nondestructive testing and evaluation; crack detection; covered crack; crack under coating, corrosion

1. INTRODUCTION

Surface cracks in metal structures result from large stresses, cyclical loading, and environmentally accelerated phenomena (i.e., corrosion) and can take place in an aircraft fuselage, turbine blades, railroad and steel-bridge infrastructure, and oil and gas pipelines, amongst others. Cracks can be visible or hidden under coatings (intentional such as paint or unintentional such as corrosion). Surface cracks on metal under coatings or filled with dielectric materials such as paint, rust, or dirt are not always reliably detected using conventional nondestructive testing and evaluation (NDT&E) methods. There are various NDT&E techniques used for crack detection including microwave [1]-[4], eddy current [5]-[6], ultrasonic [7]-[8], and thermography [9]-[12], each with varying levels of success. From a practical point of view, it is desirable to have contactless crack detection (i.e., with a lift-off distance between the surface under test and the detection probe) without the need for surface coating preparation or removal. The microwave method is one such technique that has demonstrated success for detection of covered cracks in metal surfaces. This method can be done non-contact and is inexpensive, but may require long inspection times if raster scanning of large areas is needed [13]. In addition, the measurement is sensitive to the lift-off distance and requires that a constant lift-off be maintained over the area of inspection [13]. Similarly, eddy current measurements are also adversely affected by lift-off [6]. More specifically, in the eddy current technique, lift-off is considered as a noise source and is undesirable in defect detection. If lift-off occurs in the same direction as the crack, it can subsequently conceal the crack response. Sonic-based methods are well established but often require contact with the structure under test and require an expert operator to interpret the results [7]-[8]. Thermal methods have been widely utilized in the infrastructure and transportation industries for numerous NDT&E-related needs (including crack detection) with varying levels of success [9]-[12]. For activethermography, an external heat source is applied to generate heat and subsequently the surface thermal profile is measured via an infrared (IR) or thermal camera. Generally for active thermography in NDT&E, the external heat source can be a flash lamp [9]-[10] or laser [10]-[11], or be generated via eddy currents [12] or ultrasonic [14] or microwave [26]-[28] energy. Among the active methods, eddy current thermography utilizes high-current electromagnetic signal to induce an eddy

current in a conductive material under inspection to produce a surface heat distribution, but remains sensitive to probe lift-off. In ultrasonic thermography, a contact-based transducer is utilized to generate mechanical energy. This energy is transformed into heat through friction where defects are present. Utilizing microwave energy for the thermal excitation has been considered for thermographic inspections in various industries including mining [19], aerospace [20], and transportation [21]. To this end, Active Microwave Thermography (AMT) has recently shown strong potential for NDT&E of various types of defects in rehabilitated cement-based structures [26], steel fibers in cement-based materials [27], and corrosion on metal-based materials (e.g., steel) [28]. As such, in this paper, detection and evaluation of covered cracks with various dimensions and orientations using AMT is studied through simulation and measurement.

2. ACTIVE MICROWAVE THERMOGRAPHY

In AMT, depending on the material under the test, two heating mechanisms may occur, referred to as dielectric heating and induction heating. Dielectric heating results from absorption of microwave energy in lossy dielectric materials. Generally, dielectric materials are described by their complex dielectric properties (often expressed with respect to those of free-space, ε_0) as:

$$\varepsilon_r = \varepsilon_r' - j\varepsilon_r'' \tag{1}$$

where ε_r' (or permittivity) represents the ability of a dielectric material to store microwave energy, and ε_r'' (or loss factor) represents the ability of a material to absorb energy. Thus, when a lossy material is irradiated with microwave energy, dielectric heating occurs as a result of the absorbed energy. This absorbed energy, Q, is proportional to the dielectric properties of the material, incident electric field ($\vec{E}_{inc}$), frequency (f), and can be expressed as:

$$Q = 2\pi f \varepsilon_0 \varepsilon_r'' \left|\vec{E}_{Inc}\right|^2 \tag{2}$$

Induction heating occurs due to current induced on the surface of conductive materials. More specifically, when a microwave signal impinges on a conductive material, surface current ($\vec{J}_{ind}$) is induced in the conductor due to the finite electric conductivity (σ) of the material. Due to the finite σ, ohmic loss (per unit volume) occurs. The power loss (P_{loss}) per unit volume can be expressed based on the Lorentz force equation and Newton's equation of motion, as follows [29]:

$$\frac{\partial P_{loss}}{\partial V} = \vec{J}_{Ind} \cdot \vec{E}_{Inc} \tag{3}$$

In addition, this induced surface current can serve as a source of radiated (or scattered) microwave energy which in turn may be absorbed by nearby dielectric materials (e.g., dielectric heating of corrosion).

Due to the generated (volumetric) heat within the material under the test, the heat will diffuse until an equilibrium temperature is reached. This behavior is described by the diffusion equation that is related to the thermal conductivity, k (W/m.K), specific heat, C (J/g.K), and density, ρ (Kg/m^3), of the material under the test, as well as time, t (sec), and absorbed energy, Q(W/m^3), as:

$$\rho C \frac{\partial T}{\partial t} = \nabla.(k \nabla T) + Q \tag{4}$$

In Eq. 4, during the heating period, the absorbed energy (Q) is applied (i.e., finite), while during the cooling period, Q (which is the source of heat) is set to zero (i.e., source-free condition). From Eq. (4), the temperature, T, after t seconds of heating, resulting from absorbed microwave power without considering heat diffusion (i.e., a 1st order approximation) can be expressed as follows:

$$T = \frac{Qt}{\rho C} = \frac{2\pi f \varepsilon_0 \varepsilon_r'' |E|^2 t}{\rho C} \tag{5}$$

In order to quantitatively study the temperature variation on the surface of the material under test, the thermal contrast, *TC*, is defined. More specifically, prior to microwave illumination, the structure is at equilibrium with a temperature of T_a. After microwave illumination, the temperature rise, $\Delta T(t)$, can be expressed as the difference between the absolute temperature, $T(t)$, at time t, and the ambient temperature of the structure (T_a), as:

$$\Delta T(t) = T(t) - T_a \tag{6}$$

At the location of a crack, the *TC* can be expressed as the difference between the temperature increase at the crack location, $\Delta T_D(t)$, and that of a crack-free (sound) area, $\Delta \mathrm{T}_S(t)$ as:

$$TC = \Delta T_D(t) - \Delta T_S(t) \tag{7}$$

In general, the *TC* must be at least equal to or preferably greater than the sensitivity of the thermal camera for successful crack detection after t sec of microwave illumination (i.e., heating time).

During an AMT measurement, the results are affected by noise. This temporal noise can come from the environment, emissivity variation of sample surface, thermal camera, etc. Therefore, the signal to noise ratio (*SNR*) is also considered (in addition to the *TC*) to quantitatively describe the contrast between a crack and sound area(s). Here, *SNR* is defined as the ratio of the signal, *TC*, to the temporal noise, defined as the standard deviation of the temperature in a sound area, σ_N, as:

$$SNR = 20\log_{10}\frac{TC}{\sigma_N} \tag{8}$$

For successful crack detections, an *SNR* greater than0 dB is mathematically (ideally) required [30]. However, the actual value required for successful detection in practice will depend on the application, system, environment, etc.

Both *TC* and *SNR* can be used to determine the minimum required heating time (t_{min}) and maximum effective heating (or saturation) time (t_{sat}). t_{min} is defined as the heating time required such that the *TC* is greater than the sensitivity of the thermal camera and the *SNR* is greater than 0 dB. In addition, t_{sat} is defined as point at which the *SNR* no longer increases with additional heating (i.e., microwave illumination). In other words, t_{sat} occurs when the *SNR* reaches an asymptotic value.

3. AMT SIMULATIONS

In order to investigate the efficacy of AMT for crack detection, a coupled electromagnetic and thermal model was developed by utilizing CST Microwave Studio™ and CST MultiPhysics Studio™. This model considered a steel (1008) plate with a through crack covered by and filled with a dielectric coating (corrosion) with thickness of h_C = 0.1 mm, as is illustrated in Figure 1. The plate thickness is defined as h_S = 3 mm, and the surface area of the plate is 200 × 200 mm^2. The through crack has a length of l = 40 mm and width of w = 0.3 mm. In this figure, the electric field (*E-field*) and magnetic field (*H-field*) of an incident plane wave excitation are shown. As seen, the crack may have an orientation angle with respect to the incident *E-field*, shown as ϕ, herein referred to as the crack orientation angle. For ϕ = 0°, the direction of the crack length (l) is perpendicular to the *E-field*. For ϕ = 90°, the *E-field* and crack are parallel. The electromagnetic and thermal properties of the materials relevant to this work (i.e., steel and corrosion) are provided in Table 1. The properties of air are also given since it is included in the model to consider the effect of thermal convection between the sample and air.

To conduct the simulation, first, the electromagnetic response of the sample under plane wave illumination with a frequency of 2.4 GHz (an unlicensed frequency in the industrial, scientific and medical band) was determined. In this way, the *E-field* and *H-field* for a specific level of incident microwave power (here, 50 W) inside the dielectric material (i.e., corrosion) and induced surface current on the conductive material (i.e., steel) were determined. Then, these quantities were used to calculate the absorbed energy (Q) and subsequently the temperature change based on Eq. 4.

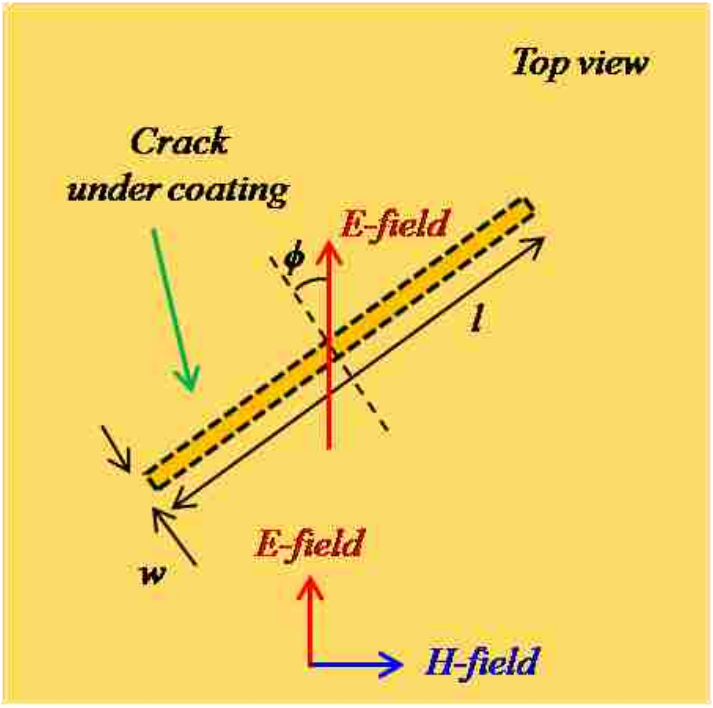

Figure 1 - Top view of a simulated steel structure with a filled and covered crack

Table 1 - Microwave and Thermal Properties

Material	**Microwave Properties**	**Thermal Properties**	
		***k* (W/m.K)**	***C* (J/g.K)**
Air	$\varepsilon_r = 1$	0.026	1.005
Corrosion [28]	$\varepsilon_r \approx 10 - j2$	0.6	0.65
Steel 1008	$\sigma \approx 8\times10^6$	59.5	0.48

For this type of inspection, both dielectric and induction heating will contribute to the temperature increase. More specifically, since a plane wave excitation is assumed, there will be uniform dielectric heating on the surface of the steel sample due to the presence of the thin layer of corrosion. As a result, this heating will not contribute to a change in the *TC* at the location of crack, as the *TC* at a crack location is related to the difference in temperature change at the crack location and elsewhere on the sample

without the presence of a crack as given in Eq. 7. Additionally, since steel is conductive, induction heating will take place uniformly throughout the steel sample, thereby also not contributing to the *TC* at the location of the crack. However, when a crack is present and under perpendicular illumination (ϕ = 0° in Figure 1), depending on the frequency of the illuminating signal, crack dimensions, and dielectric properties of the filling material, a propagating electric field mode (such as the dominant transverse electric field mode for a rectangular waveguide, or TE_{10} mode) may be generated within the crack. In other words, the crack will act like a narrow and very short waveguide (or aperture slot). The length of the crack corresponds to the broad dimension of the waveguide and the depth of the crack corresponds to the length of the waveguide. Thus, due to the concentrated *E-field* within the crack (which is filled with a lossy dielectric), a temperature increase will result due to dielectric heating of the crack filling material (i.e. corrosion).

To illustrate this phenomenon, consider a crack with l = 40 mm filled with corrosion (ε_r' = 10). The TE_{10}mode cut-off frequency is ~1.2 GHz for this scenario, meaning that dielectric heating will occur for frequencies greater than 1.2 GHz. To illustrate this effect, the *E-field* distribution in the crack for frequencies of 0.4 GHz (below cut-off), and 1.2 GHz (slightly above cut-off) are illustrated in Figure 2.

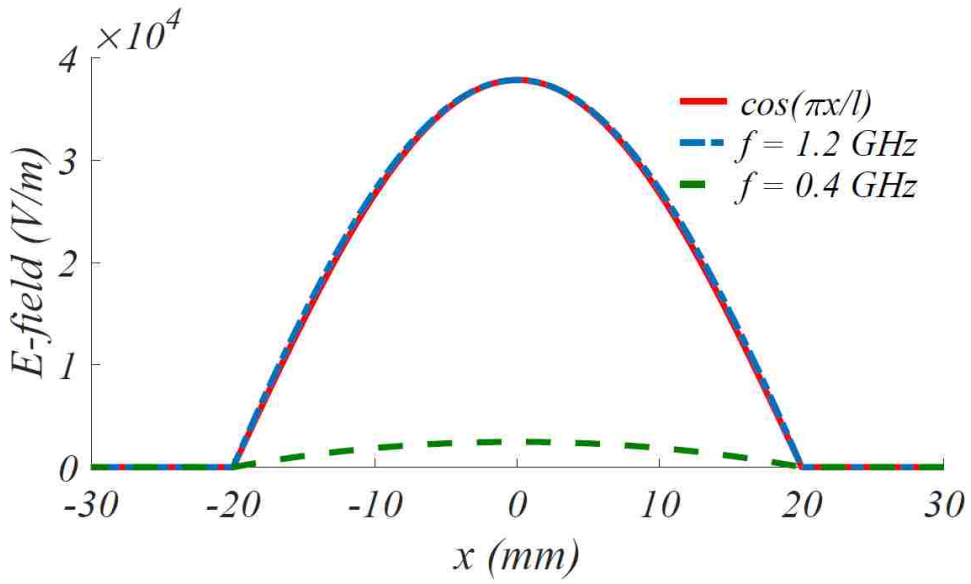

Figure 2 - Simulated normalized E-field as a function of position along the crack length with l = 40 mm for below (0.4 GHz) and above cut-off (1.2 GHz).

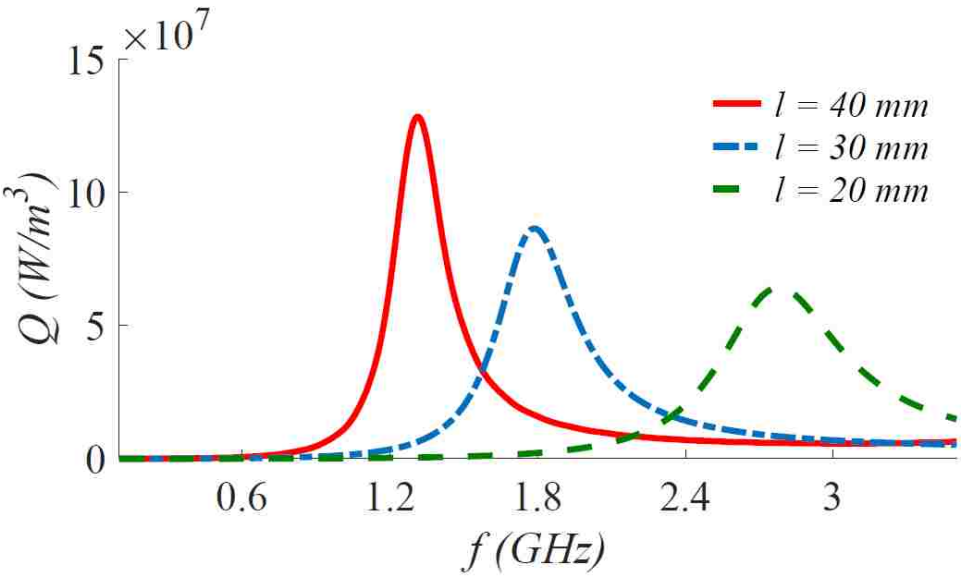

(a)

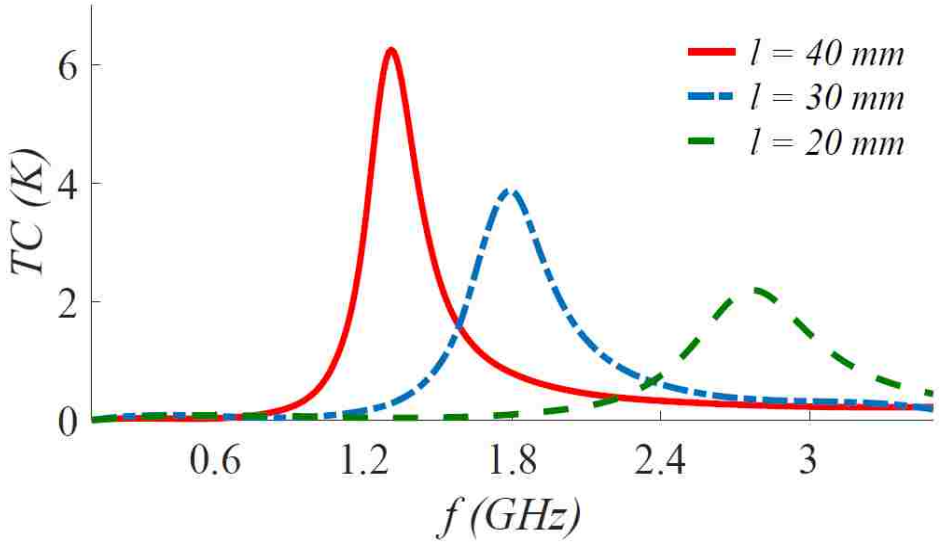

(b)

Figure 3 - Simulated TC as a function of frequency

As seen, the *E-field* in the crack at 1.2 GHz is similar to the cos($\pi x/l$) where x is along the length of crack with the zero value at the center of crack. This distribution is proportional to the TE_{10}. For 0.4 GHz, the magnitude of the *E-field* is much lower than the case of 1.2 GHz, showing the waveguide (including cut-off) behavior of the crack.

To further illustrate this waveguide effect, in Figure 3, the *Q* and *TC* for three cracks with lengths of 20 mm, 30 mm and 40 mm under microwave illumination as a function of frequency are presented (all filled with corrosion). For cracks with lengths of

40, 30 and 20 mm, the corresponding cut-off frequencies are ~1.2 GHz, ~1.6 GHz, and ~2.4 GHz.

As seen in Figure 3, the maximum *Q* and *TC* for each crack occurs around its proportional cut-off frequency. Further, since essentially no *E-field* exists in the crack below the cut-off frequency, the *Q* (and subsequent *TC*) is zero (since $Q \approx f|E|^2$ as given in Eq. 5). As the frequency increases beyond cut-off, the Q and TC decrease, due to the decrease in *E-field* from wave attenuation. In addition, the maximum *Q* (and *TC*) decreases with decreasing crack length. This is due to a reduction in lossy dielectric material within the crack thereby causing a reduction in dielectric heating. A similarity between *Q* and *TC* is also evident and is expected, considering the relationship between the two (given in Eq. 5).The dependence of *TC* on crack length may also have practical ramifications. In other words, if an AMT inspection were to be done using a range of illuminating frequencies, the frequency at which the maximum *TC* occurs may give an indication of crack length (assuming the dielectric properties of the crack filling are known).

The relationship between crack orientation angle (ϕ)and the subsequent *TC* is also important as it relates to crack detectability. For a given crack orientation angle of ϕ, the *E-field* distribution generated in the effective waveguide (i.e., the crack) can be expressed as the projection of the incident *E-field* along the width of the waveguide (length of the crack) as $E\cos(\phi)$. Thus, it is expected that the maximum dielectric heating (and *TC*) will be proportional to $\cos(\phi)$. Therefore, the relationship between *TC* and the illuminating *E-field* can be expressed as follows:

$$TC \propto \cos^2(\phi) \tag{9}$$

To this end, simulation results for temperature increase (ΔT, related to *TC*) on the surface of the sample after 60 sec of microwave illumination is shown in Figure 4 for three different angles of ϕ. For the case of $\phi = 0°$, it can be seen that the distribution of the temperature is similar to the TE_{10}mode that is generated (see Figure 2), in which the maximum and minimum temperature of the crack occurs at the center and edges of the crack, respectively. Furthermore, when the crack is parallel with respect to the

polarization of the *E-field* (ϕ = 90°), the TE_{10} mode is not generated and subsequently no dissipated microwave energy results. For ϕ = 45°, the temperature at the center of the crack is approximately half of the temperature for ϕ = 90°, again showing the $\cos^2(\phi)$ behavior. This dependence of ΔT (and subsequently the *TC*) on ϕ may also have practical ramifications. In other words, the orientation of the crack may be determined if a full range of *E-field* polarization is used (0° to 90°, or circular polarization) and the *TC* is monitored for its maximum value (thereby providing an indication of the crack orientation)

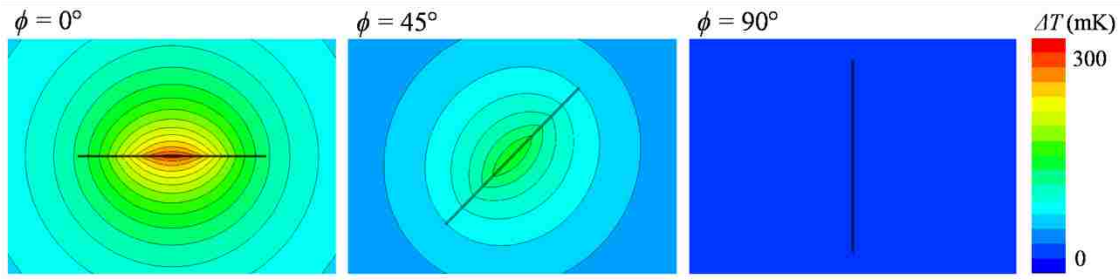

Figure 4 – Simulated temperature rise after 60 sec microwave heating

In Figure 5, the temporal behavior of the *TC* for a crack with various orientation angles (ϕ = 0°, 45° and 90°) is presented during the heating (illumination) and cooling periods (60 sec each). If the crack orientation angle is zero, highest *TC* will occur (as discussed above and illustrated in Figure 4). If ϕ = 90°, the lowest *TC* is expected and is shown here to be near zero (the slight increase is attributed to minor dielectric heating). For the case of ϕ = 45°, the *TC* is in between that of ϕ = 0° and 90°. As shown in Eq. 9 and discussed above, the dissipated heat and subsequently the *TC* is proportional to $\cos^2(\phi)$. Comparing the results of ϕ = 0° and 45°, it can be seen that the peak temperature at ϕ = 45° is half of that at the maximum (ϕ = 0°; *TC* = ~0.28 K compare to ~0.14 K for ϕ = 45°). In this way, the expected relationship with ϕ (i.e., cosine-squared) is evident.

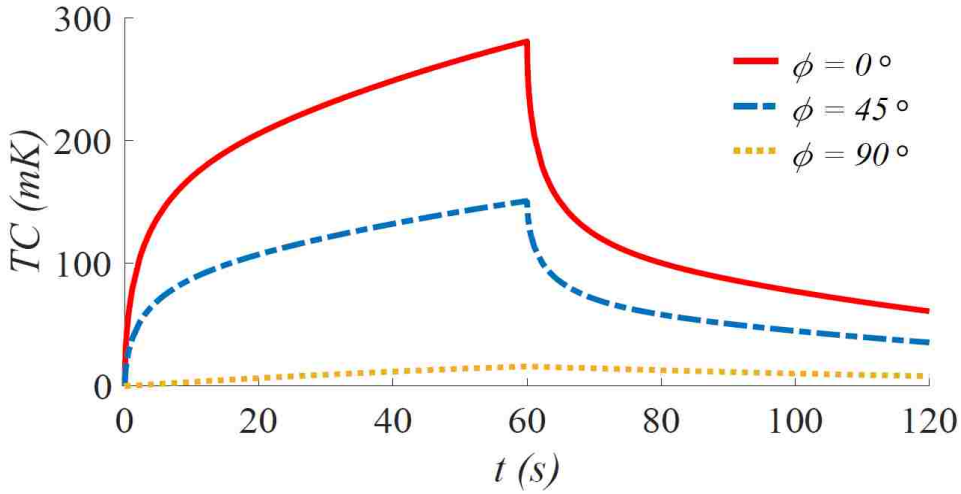

Figure 5 – Simulated *TC* as a function of time for various crack orientation angles

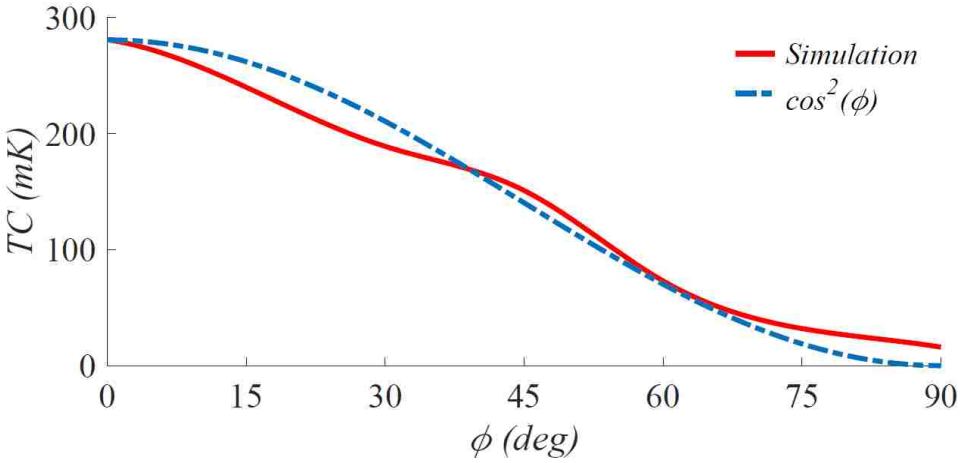

Figure 6 – Simulated *TC* as a function of crack orientation angle

In Figure 6, the *TC* after 60 sec heating as a function of orientation angle for acrackis presented, along with a representative $\cos^2(\phi)$ curve. By comparing the *TC* and $\cos^2(\phi)$, the cosine-squared relationship is again confirmed. The slight variation between the *TC* and $\cos^2(\phi)$ function may be attributed to effects from thermal diffusion and convection that are considered in the simulation but neglected in Eq. 5. Furthermore, as it

relates to practical detection via AMT measurements (discussed in the next section), since the sensitivity of the available thermal camera (FLIR T430sc) is 30 mK, the crack orientation angle that results in a detectable crack must cause a *TC* greater than 30 mK, which for this application translates to $\phi <$ ~65°, according to Figure 6.

A last aspect that can be investigated is the effect of crack width, *w* (or the height of the effective waveguide). In Figure 7, the temporal *TC* for a crack with an orientation angle of ϕ = 0° for various crack widths is presented during the heating and cooling periods. As shown, an increase in *w* causes an increase in the *TC*. This is a result of the increase in dielectric material, meaning there is more material that will undergo dielectric heating. Subsequently, a higher *TC* will result as *w* increases. More specifically, by increasing *w* from 0.3 mm to 0.6 mm, the *TC* increases from 280 mK to 570 mK (approximately a factor of 2). Considering a first order approximation, doubling the width of the crack doubles *TC*; however, effect of heat diffusion across the direction of the width will slightly alter this value. In addition, changing from 0.3 mm to 0.9 mm, *TC* becomes approximately triple.

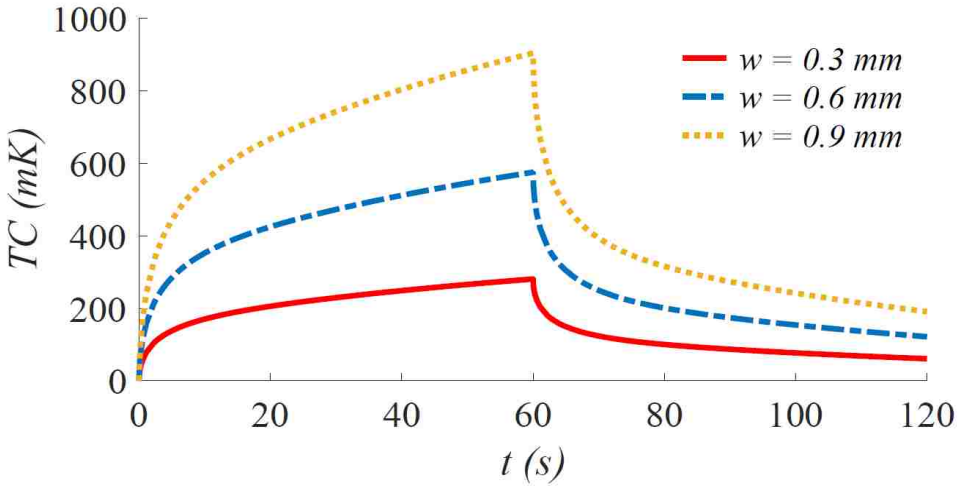

Figure 7 – Simulated TC for various crack width at ϕ = 0°

4. AMT MEASUREMENTS

To further illustrate the potential for AMT as a structural assessment tool for NDT&E of surface cracks on metal structures, measurements were conducted on a representative sample similar to the geometry studied above via simulation. The sample has a crack (man-made) with length of ~40 mm, shown in Figure 8a. The depth and width of the crack is not consistent and varies in the range of ~0.1-0.3 mm over the entire crack length. On the surface of the sample, there is a thin (and non-uniform) layer of corrosion with thickness f ~0.1 mm that covers the crack. Although it was shown that crack with length of 40 mm has the highest *TC* at 1.2 GHz, however, a frequency of 2.4 GHz will be utilized for measurements as this frequency is an unlicensed allocated frequency used for industrial, scientific and medical (ISM) applications. Furthermore, even though the simulated *TC* in Figure 3 at 2.4 GHz (*TC* = ~0.3 K) is much less than the maximum at 1.2 GHz (*TC* = ~4 K), the crack can still be detected at this frequency since the *TC* is still ten times greater than the sensitivity of the camera (0.03 K). This has important practical ramifications since the limitation on length (corresponding to cut-off frequency) does not have to be met for successful detection.

The AMT system used for measurements is capable of transmitting 50 W of power from a horn antenna with aperture dimensions of 23×17 cm^2, as is illustrated in Figure 8b. As shown, the microwave signal is generated at signal generator and amplified through a power amplifier unit. The microwave illumination and thermal measurement is controlled and synchronized with a computer control unit. In addition, thermal images are captured throughout the inspection time for real-time monitoring and stored for post-processing. In addition, a lift-off is necessary in order for thermal images to be obtained of the surface (meaning the horn antenna does not block the "view" of the thermal camera). However, the radiated power (50 W at the antenna aperture) decreases with increasing lift-off. To this end, it was determined via measurement that a lift-off in the range of ~10-40 cm is acceptable since the required *TC* (30 mK minimum) and *SNR* (0 dB minimum) for successful crack detection are met.

Figure 9 shows the measured *TC* and *SNR* for the covered crack with a lift-off of 15 cm for three crack orientation angles. As above, the heating/illumination and cooling times are 60 sec each. In addition, crack orientation angles of ϕ = 0°, 45° and 90° were

considered (by rotating the sample with respect to the orientation of the horn antenna). More specifically, in Figure 9a (similar to Figure 5 for simulation), the measured *TC* is provided. The same trends exhibited in simulation are also evident in the measurement results. More specifically, for ϕ = 0°, the highest *TC* was observed, and for ϕ = 90°, the *TC* is near zero, and for ϕ = 45°, the *TC* in between the two. Another practical aspect that can be determined from these results is the minimum required heating time (i.e., the illumination time necessary such that the *TC* is greater than the sensitivity of the thermal camera). In other words, for ϕ = 0°, t_{min} = ~1 sec and for ϕ = 45°, t_{min} = ~3 sec, indicating that the minimum heating time is a function of crack orientation angle and therefore must be considered for inspections where the crack orientation is not known. In addition, the *TC* does not reach the minimum sensitivity of the thermal camera (30 mK) for ϕ = 90°. In Figure 9b, the *SNR* is presented. As seen, for ϕ = 0°, the *SNR* reaches a maximum (as is expected since the *TC* is also maximum at this angle). For ϕ = 90°, since *TC* is near zero, the *SNR* < 0 dB and therefore the crack cannot be detected even with advanced signal processing techniques. Therefore, the minimum required heating time for the cases of ϕ = 0° and 45° are t_{min} = ~1-3 sec. In addition, although the saturated value for *SNR* is different for both cases (~29 dB for ϕ = 0° vs. ~36 dB for ϕ = 45°), the maximum effective heating time for both cases is t_{sat} = ~30 sec, since the *SNR* for both cases saturates at that time. This is important as it relates to the practicality of the measurement, meaning that the maximum effective heating time is constant for a given inspection, regardless of whether or not the crack orientation is known beforehand.

The effect of heating/illumination time is further illustrated in Figure 10, where two-dimensional surface images of the *TC* and *SNR* are presented. In Figure 10a, the temperature increase (defined in Eq. 6) is presented after 5, 20, and 60 sec of microwave illumination with a crack orientation angle of ϕ = 0° and a 15 cm lift-off. As can be seen, after a short period of microwave illumination (e.g., 5 sec), the *TC* exceeds the sensitivity of the thermal camera and the crack is evident in thermal image. In addition, the effect of heat diffusion is also evident, as the thermal indication of the crack becomes larger with illumination time. In Figure 10b, the *SNR* is presented. It can be seen that the *SNR* at the crack location after 5 sec of illumination is much greater than 0 dB (*SNR* = 25 dB) and the shape of the crack can be determined easily. Thus, it can be concluded that 5 sec of

microwave illumination is sufficient for this inspection (which is much shorter than the required time for raster scanning necessary in order to use other NDT techniques). As mentioned before, ~30 sec is the maximum effective heating time and more heating time leads to excessive heating and saturation.

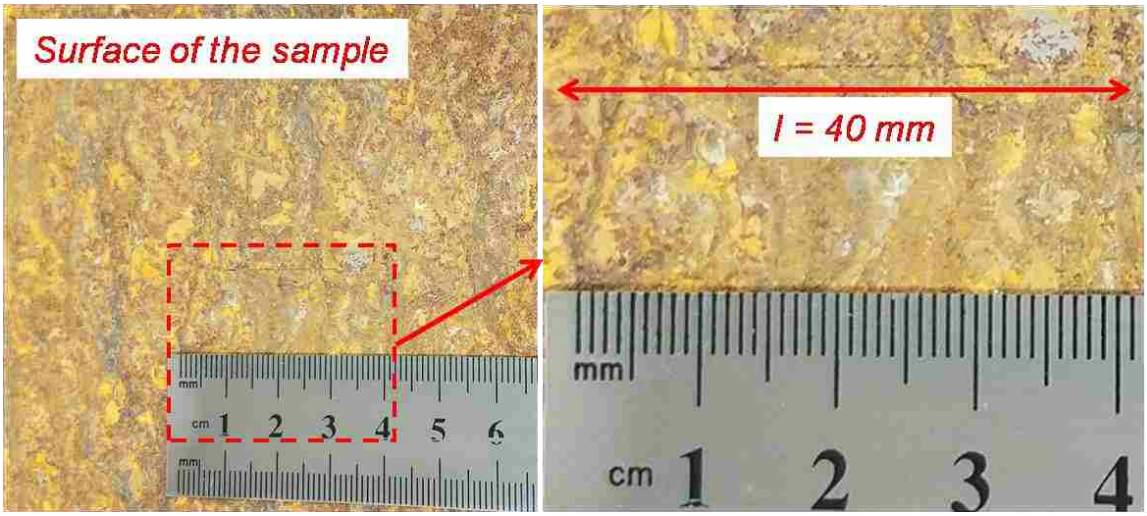

(a)

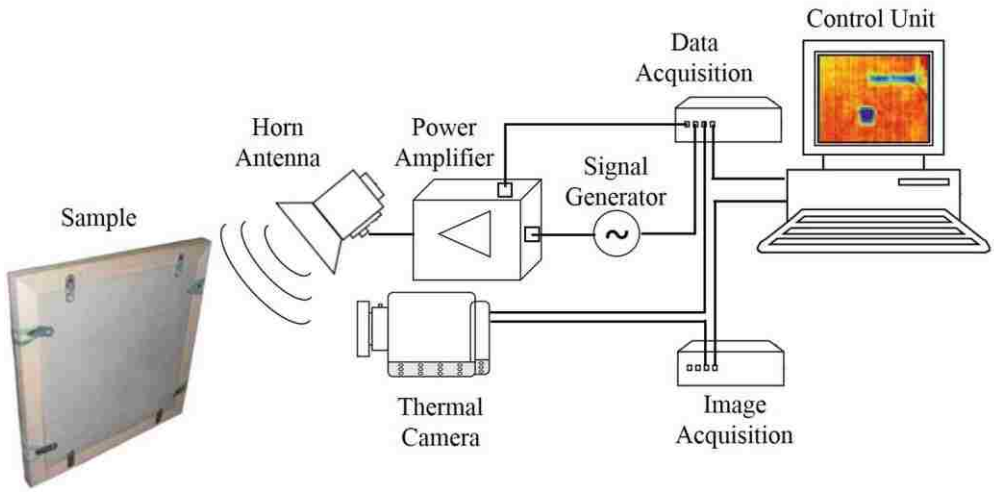

(b)

Figure 8 – (a) Top view of metal sample with surface crack, and (b) illustration of the AMT measurement set up.

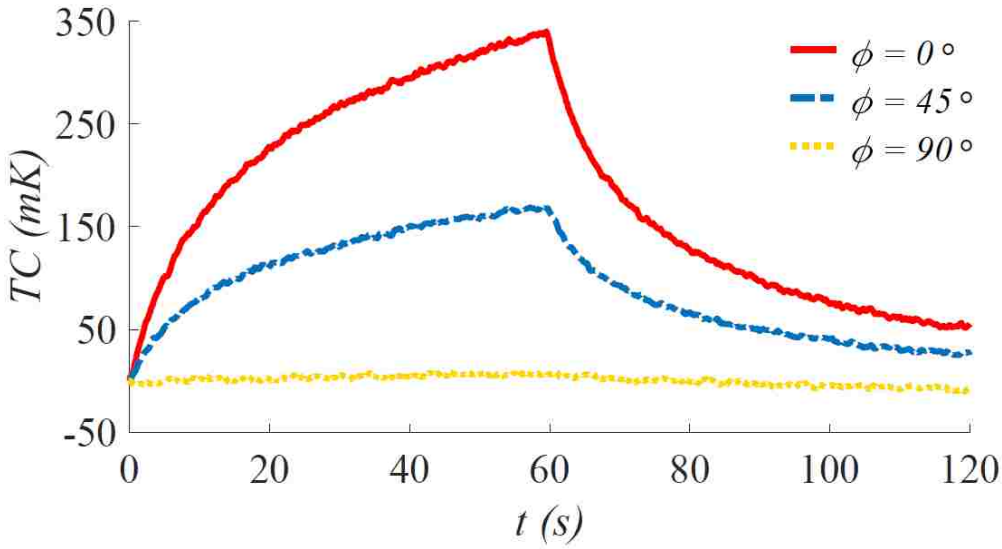

(a)

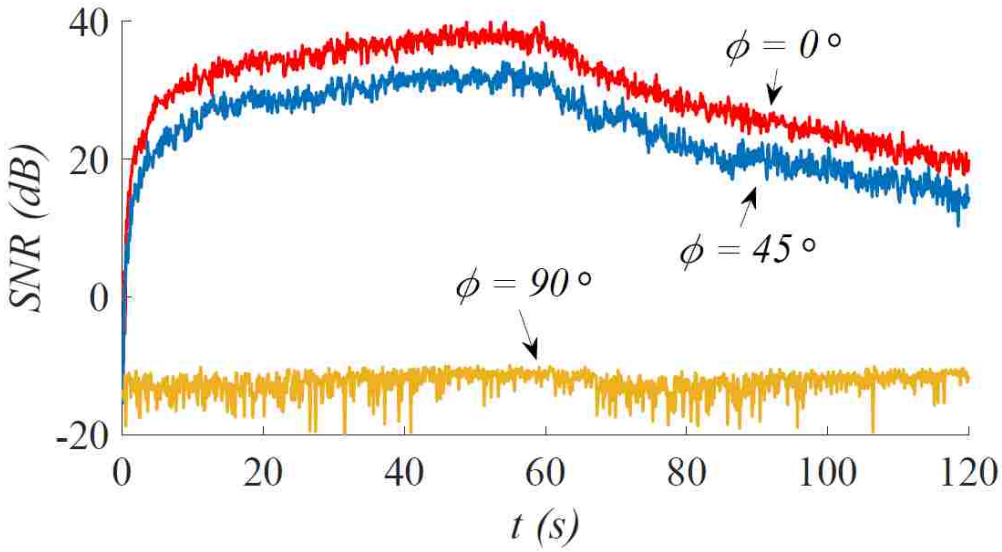

(b)

Figure 9 - Measured (a) *TC* and (b) *SNR* for various crack orientation angles with 15 cm lift-off

Lastly, the effect of lift-off (15 cm and 30 cm) was experimentally investigated on a crack with an orientation angle of ϕ = 0°, with the *TC* and *SNR* shown in Figure 11. By examining the results of Figure 11a (measured *TC*), it can be seen that the *TC* is affected by lift-off. It is known that by increasing the lift-off, the amount of power impinging on the sample decreases (due to free space losses). However, it can be observed that for a 30

cm lift-off (which is much greater than the lift-off in microwave or eddy current methods), the *TC* is still greater than the sensitivity of the thermal camera (30 mK, shown by green dashed-line) after a short period of illumination time (~5 sec). The same can be said for a 15 cm lift-off (i.e., the necessary illumination time, t_{min}, is ~5 sec). This is important practically as it relates to selecting a value for t_{min} for this type of inspection without the need for factoring in the effect of lift-off (so long as the lift-off is within a reasonable ~ 0.5 m or less). The same information can also be seen in Figure 11b where the *SNR* for lift-offs of 15 and 30 cm is shown. Here, the minimum required heating time for both cases is also ~5 sec. In addition, although the saturated *SNR* value is different for both cases (~22 dB vs. ~36 dB), the maximum effective heating time for both cases is t_{sat} = ~30 sec. Therefore, although the level of saturation decreases with increasing lift-off, the optimal range of detection (t_{min}-t_{sat}) experiences negligible change. Thus, it can be concluded that the detectability (in terms of illumination time) can be performed with a larger lift-off (e.g., 30 cm) with reliable results, which is of practical interest to operators for field-testing.

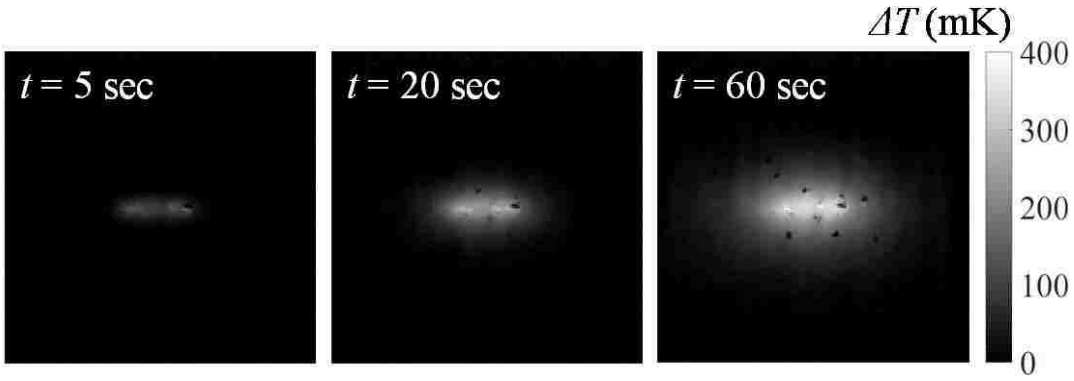

(a)

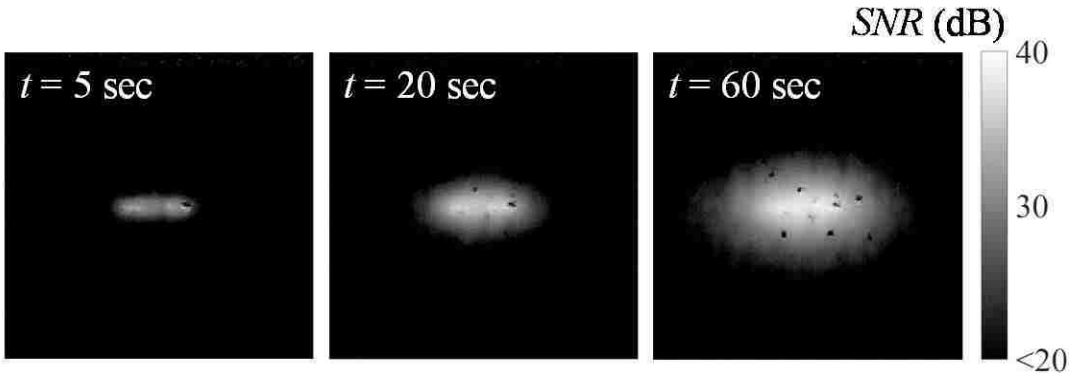

(b)

Figure 10 – Measured (a) *TC* and (b) *SNR*

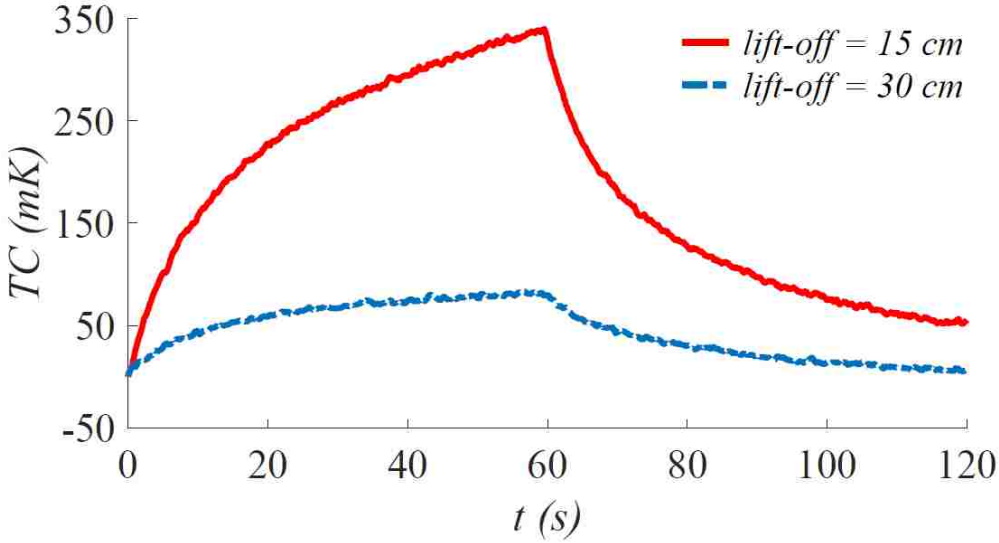

(a)

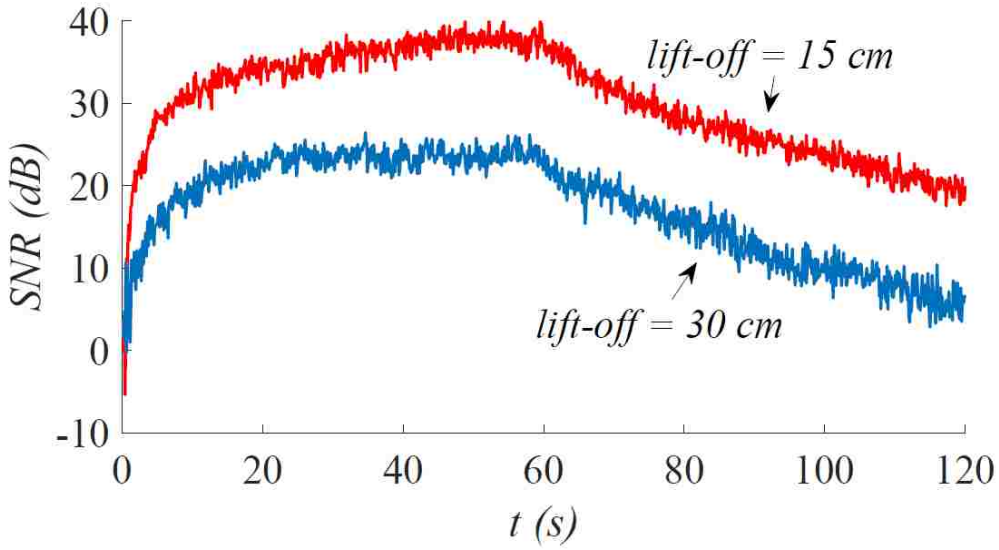

(b)

Figure 11 - Measured (a) *TC* and (b) *SNR* for two different lift-off

5. CONCLUSION

Active Microwave Thermography (AMT) as a novel NDT&E method for infrastructure and aerospace industries is presented which is based on the integration of microwave and thermographic NDT. As such, simulations and measurements of a covered surface crack in a metal structure are presented. It was shown that depending on the crack length and width, maximum *TC* can be obtained when the crack length corresponds to a rectangular waveguide cut-off frequency (meaning the crack operates as a very short waveguide). In addition, the polarization of the *E-field* with respect to the crack orientation is important and is referred to as crack orientation angle (or ϕ). It was observed that for the case of a crack that is parallel to the *E-field* polarization (ϕ = 90°), the *TC* is near zero and the crack cannot be detected. For the case of a crack that is perpendicular to the *E-field* polarization (ϕ = 0°), the *TC* reaches a maximum. Furthermore, a crack with an orientation angle of ϕ < ~65° can be detected for this type of AMT inspection. However, this value is dependent on the sensitivity of the thermal camera, environmental noise, etc., and will therefore change for a given system and application. Also, lift-off was shown to affect the *TC* and *SNR*, but the minimum required heating time and maximum effective heating time (t_{min} and t_{sat}, respectively) is in the range of 5-30 sec for this work.

REFERENCES

[1] C. Yeh, and R. Zoughi "A novel microwave method for detection of long surface cracks in metals." IEEE Transactions on Instrumentation and Measurement, 43, no. 5, pp. 719-725,1994.

[2] C. Huber, H. Abiri, S. Ganchev, and R. Zoughi. "Modeling of surface hairline-crack detection in metals under coatings using an open-ended rectangular waveguide." IEEE Transactions on Microwave Theory and Techniques, 45, no. 11, pp. 2049-2057, 1997.

[3] S. Kharkovsky, M. T. Ghasr, and R. Zoughi. "Near-field millimeter-wave imaging of exposed and covered fatigue cracks." IEEE Transactions on Instrumentation and Measurement, 58, no. 7, pp. 2367-2370, 2009.

[4] A. Mirala, and R.SarrafShirazi. "Detection of surface cracks in metals using time-domain microwave non-destructive testing technique." IET Microwaves, Antennas & Propagation, 11, no. 4, pp. 564-569, 2016.

[5] G. Tian, A.Sophian, D. Taylor, and J.Rudlin. "Multiple sensors on pulsed eddy-current detection for 3-D subsurface crack assessment." IEEE Sensors Journal, 5, no. 1, pp. 90-96, 2005.

[6] W. Yin, R.Binns, S. Dickinson, C. Davis, and A. Peyton. "Analysis of the liftoff effect of phase spectra for eddy current sensors." IEEE Transactions on Instrumentation and Measurement, 56, no. 6, pp. 2775-2781, 2007.

[7] D. Donskoy, A. Sutin, and A. Ekimov. "Nonlinear acoustic interaction on contact interfaces and its use for nondestructive testing." NDT&E International, 34, no. 4, pp. 231-238, 2001.

[8] E. Glushkov, N.Glushkova, A.Ekhlakov, and E.Shapar. "An analytically based computer model for surface measurements in ultrasonic crack detection." Wave Motion, 43, no. 6, pp. 458-473, 2006.

[9] P.Broberg. "Surface crack detection in welds using thermography." NDT&E International, 57, pp. 69-73, 2013.

[10] M. Noethen, K.Wolter, and N.Meyendorf. "Surface crack detection in ferritic and austenitic steel components using inductive heated thermography." In 33rd on IEEEInternational Spring Seminar Electronics Technology (ISSE), pp. 249-254., 2010

[11] Y. An, J. Kim, and H. Sohn. "Laser lock-in thermography for detection of surface-breaking fatigue cracks on uncoated steel structures." NDT&E International, 65, 54-63, 2014.

[12] L. Cheng, and G.Tian. "Surface crack detection for carbon fiber reinforced plastic (CFRP) materials using pulsed eddy current thermography." IEEE Sensors Journal, 11, no. 12, pp. 3261-3268, 2011.

[13] A. Foudazi, T. Roth, M. T. Ghasr, and R. Zoughi. "Aperture-coupled microstrip patch antenna fed by orthogonal SIW line for millimetre-wave imaging applications." IET Microwaves, Antennas & Propagation vol. 11, no. 6, pp. 811-817, 2016.

[14] A. Dillenz, G. Busse, and D. Wu. "Ultrasound lockin thermography: feasibility and limitations Diagnostic Imaging Technologies and Industrial Applications," Proc. SPIE vol. 10, no. 5, pp. 3827, 1999.

[15] P. Levesque, A. Deom, and D. Balageas, "Non destructive evaluation of absorbing materials using microwave stimulated infrared thermography"in Review of Progress in Quantitative Nondestructive Evaluation; Springer, pp. 649–654, 1993.

[16] G. D'Ambrosio, R. Massa,M.Migliore,G.Cavaccini, A. Ciliberto, and C. Sabatino, "Microwave excitation for thermographic NDE: An experimental study and some theoretical evaluations," Mater. Eval., 53, pp. 502–508, 1995.

[17] M. Bowen,R.Osiander, J. Spicer, J. Murphy, "Thermographic Detection of Conducting Contaminants in Composite Materials Using Microwave Excitation,"in Review of Progress in QNDE, vol. 14, pp. 453–460, 1995.

[18] C. DiMarzio, C. Rappaport, W. Li, M. E. Kilmer, and G. Sauermann, "Microwave-enhanced infrared thermography," Proc. SPIE, Photonics East (ISAM, VVDC, IEMB), pp. 337-342, Feb. 1999.

[19] D. Balageas and P. Levesque, "Mines detection using the EMIR method," in Proc. QIRT, pp. 71–78, 2002.

[20] L. Cheng, G. Tian,B.Szymanik, "Feasibility studies on microwave heating for nondestructive evaluation of glass fibre reinforced plastic composites," In Proceedings of the IEEE International Instrumentation and Measurement Technology Conference, pp. 10–12, pp. 1–6, 2011.

[21] S.-A. Keo, D. Defer, F. Breaban, and F. Brachelet, "Comparison between microwave infrared thermography and CO2 laser infrared thermography in defect detection in applications with CFRP," Mater. Sci. Appl., vol. 4, no. 10, pp. 600–605, 2013.

[22] A. Foudazi, M. T. Ghasr, and K. M. Donnell, "Application of active microwave thermography to inspection of carbon fiber reinforced composites," In IEEE AUTOTESTCON, pp. 318-322, 2014.

[23] A. Foudazi, K. M. Donnell, and M. T. Ghasr, "Application of active microwave thermography to delamination detection," In Proceedings IEEE International Instrumentation and Measurement Technology Conference (I2MTC), pp. 1567-1571, 2014

[24] D. Palumbo,F. Ancona, and U. Galiett,. "Quantitative damage evaluation of composite materials with microwave thermographic technique: feasibility and new data analysis."Meccanica, vol. 50, no. 2 pp. 443-459, 2015.

[25] H. Zhang,R. Yang, Y. He, A.Foudazi, L. Cheng, and G. Tian, “A Review of Microwave Thermography Nondestructive Testing and Evaluation,” Sensors, vol. 17, no. 5, 2017.

[26] A. Foudazi, C. Edwards, M.T. Ghasr, and K. M. Donnell. "Active Microwave Thermography for Defect Detection of CFRP-Strengthened Cement-Based Materials." IEEE Transactions on Instrumentation and Measurement, 65, no. 11, pp. 2612-2620, 2016.

[27] A. Foudazi, I. Mehdipour, K. M. Donnell, and K. H. Khayat, "Evaluation of steel fiber distribution in cement-based mortars using active microwave thermography,"Materials and Structures, 49, no. 12, pp. 5051-5065, 2016.

[28] A. Foudazi, M. T. Ghasr, and K. M. Donnell, “Characterization of corroded reinforced steel bars by active microwave thermography,” IEEE Trans. Instrum. Meas., vol. 64, no. 9, pp. 2583–2585, Sep. 2015.

[29] S. Orfanidis;“Electromagneticwaves and antennas,” New Brunswick, NJ: Rutgers University, 2002.

[30] K. Srinivas, A. O. Siddiqui, and J. Lahiri, “Thermographic inspection of composite materials,” in Proc. Nat. Seminar Non-Destruct. Eval., vol. 12, pp. 7–9, 2006.

SECTION

2. CONCLUSIONS AND FUTURE WORK

The overarching objective of this research was to develop Active Microwave Thermography (AMT) as a new nondestructive testing and evaluation (NDT&E) and structural health monitoring tool with application in the aerospace and transportation/infrastructure industries. AMT is an integrated technique that incorporates aspects of microwave NDT and thermography. AMT is based on utilizing a microwave excitation (to generate heat), and subsequently monitoring the surface thermal profile with a thermal camera. AMT offers some unique advantages including the potential for non-contact, selective and focused heating, achievable by taking advantage of the properties of microwave signals and their interaction with materials. More specifically, proper selection of frequency, power level, lift-off (distance between source and sample), and polarization can provide optimal detection and evaluation of defects for a variety of NDT-related issues.

During an AMT inspection, two heating mechanisms are possible, referred to as dielectric heating and induction heating. Dielectric heating occurs as a result of the interaction of microwave energy with lossy dielectric materials which results in dissipated microwave energy and a subsequent increase in temperature. Induction heating is a result of induced surface current on conductive materials with finite conductivity under microwave illumination and subsequent ohmic loss in conductive materials. Additionally, these surface currents can serve as a secondary source of electromagnetic energy, thereby contributing (indirectly) to dielectric heating as well. As such, by taking advantage of one or both of these heating mechanisms, AMT has been considered as a viable NDT option for inspection of defects in single- or multi-layered fiber-reinforced polymer-strengthened cement-based materials, evaluation of steel fiber percentage and distributions in steel fiber reinforced structures, characterization of corrosion ratio on corroded reinforcing steel bars (rebar), and evaluation of covered surface cracks orientation and size in metal structures, as are detailed below in the following 5 papers.

In Paper I, the application of AMT for detection of various types of defects in CFRP-strengthened structures was presented. As such, simulations and measurements were performed for various cases. For uni-directional CFRP parallel with respect to the *E-field* polarization, structure behaves as conductive material (results in induction heating). For perpendicular polarization behaves as a lossy dielectric (results in dielectric heating). From temporal *TC*, defect in perpendicular polarization illumination experience *TC* with a factor of ~ten-times, compare to parallel polarization illumination. Form temporal *SNR*, it was observed that *SNR* value does not improve significantly after ~60 sec of microwave illumination, indicating a potentially maximum effective heat time. Also, the minimum required heating time for which an *SNR* of greater than 0 dB is achieved is studied. It is concluded that at least ~5 sec is required for successful detection of defects in such structures. As such, the optimum inspection time is at the range of ~(5-60 sec). In addition, for parallel polarization illumination, median filter can be applied to improve the SNR around 3 dB, which can help to determine the defect location and shape. This is important for cases where a parallel polarized excitation cannot be avoided, such as bidirectional CFRP.

In Paper II, the application of AMT for detection of defects at different interfaces within a multilayered CFRP laminate (placed on a structure/substrate) was investigated. For a two-layer CFRP laminate, it was shown that 8 possible cases for the location of the defect can occur. These cases are a result of the orientation of CFRP layers with respect to the *E-field* polarization of the incident wave and also the defect location (between CFRP layers or at the structure-CFRP interface). It is shown that the *TC* differs for each case, meaning an indication of defect location is possible from an AMT inspection. Also, the optimum inspection time based on the minimum required heating time and maximum effective heating time is at the range of ~(5-60 sec).

In Paper III, the application of AMT for steel fiber evaluation in fiber-reinforced cement-based materials was presented. In this type of structure, it was shown that both heating mechanisms can occur. It was also observed that fiber depth and dielectric properties of mortar have a significant influence on the *TC*. However, the average temperature over the surface for uniform fiber distribution should be repeatable. In addition, it is also observed that due to the increase in induction heating with increasing

fiber percentage, the *TC* increases. However, it was shown that the samples containing 1% and 2% steel fibers (by volume) have a higher *TC* as compared to a sample made with 3% fiber content showing non-uniform fiber distribution and potential fiber clumping. In addition, good correlation between the *TC* and mechanical test results was achieved for various samples.

In Paper IV, the application of AMT for characterization of corrosion in steel bridges or reinforcing rebar in concrete was investigated. It was shown that the rebar has to be parallel to the *E-field* polarization in order to cause the maximum induced current and subsequent scattering from the rebar. For experimental part, a rebar with several corroded areas was considered in order to investigate the percentage of corrosion present. It was shown that a higher percentage of corrosion leads to increased absorption of microwave energy as well as a greater *TC*. Moreover, increasing frequency leads to a greater temperature difference as well.

In Paper V, AMT was investigated for detection and evaluation of covered cracks in metal structures. It was shown that both heating mechanisms are present, however dielectric heating due to the loss factor of the material inside the crack leads to have high *TC*. At the presence of the crack (depending on the frequency, crack dimensions, dielectric properties of filling materials, and also boundary conditions), a propagating mode TE_{10} may be set up at the crack meaning the crack will act like a very short in length waveguide with the broad dimension corresponding the length of the crack. Thus, it is shown that maximum heat generation occurs when the crack is perpendicular to the *E-field* polarization. More specifically, the relationship between the *TC* and dissipated microwave energy (and subsequent heat generation) is proportional to $\cos^2(\phi)$, where ϕ is the angle between the *E-field* polarization and direction perpendicular to crack length. Thus, according to the minimum sensitivity of the current AMT system thermal camera, a crack with an orientation angle of $\phi = 65°$ can be detected. In addition, *SNR* was studied and it was shown that by changing the lift-off, the value of the *SNR* changes, however, the minimum required heating time and maximum effective heating time (t_{min} - t_{sat}) is at the range of ~(5-30 sec) for this work and will not change significantly based on the crack orientation angle and lift-off.

For future work, feature extraction of the defect including the depth and shape in layered CFRP-strengthened structures can be investigated. This can be done by considering the Fourier series for the temporal *TC* or *SNR*. Effect of source frequency can also be investigated for inspection of this type of structure. In addition, same approach of temporal Fourier analysis can be used for feature extraction of flat bottom holes (i.e., defects) in carbon fiber laminates. For steel fiber reinforced structures, AMT can be utilized *in situ* in order to investigate the steel fiber distribution in fresh concrete, thereby requiring the effect of moisture content in the concrete to be studied. For characterization of corrosion in steel rebar, a temporal investigation of cement-based samples reinforced with rebar that is corroded over time is of interest. Finally, further investigation into the electromagnetic parameters that contribute to the modes set up within the crack is necessary, including the effect of filling, full study of crack dimensions, effect of higher order modes on the generated heat, etc.

VITA

Ali Foudazi was born in Tehran, Iran, in 1986. He received his B.Sc. and M.Sc. degrees in Electrical Engineering from Shahed University, Tehran, Iran, in 2009 and 2012, respectively. He was visiting postgraduate student at Radar Remote Sensing Group at University of Cape Town, South Africa, spring 2011. He joined the Applied Microwave Nondestructive Testing Laboratory (*amntl*) at the Missouri University of Science and Technology in Fall 2013 as a Ph.D. student. In December 2017, he received his Ph.D. in electrical engineering from Missouri University of Science and Technology. His research interests include microwave thermography, coupled electromagnetic-thermal problems, microwave and millimeter-wave imaging, antenna design, material characterization, electromagnetic compatibility and signal integrity. Ali is a member of multiple IEEE societies including Instrumentation & Measurement Society (IMS), and Antennas & Propagation Society (APS). He is an active member of Eta Kappa Nu (HKN) IEEE honor society, as well as American Society for Nondestructive Testing (ASNT). He is organizing committee for 26^{th} and 27^{th} ASNT Research Symposium and session co-chair during the 25^{th} and 26^{th} Research Symposium. He has been awarded multiple awards from different professional societies including the 2015 IEEE Instrumentation & Measurement Graduate Fellowship, the 2015 American Society for Nondestructive Testing Graduate Fellowship, the 2016 IEEE EMC Student Hardware Design Contest, the 2017 Missouri University of S&T Dean's Ph.D. Scholar Award, and multiple travel grant awards.